Finite element analysis of flow liquefaction in a tailings dam using two advanced constitutive soil models

A comparative study of CASM and NorSand

V.H. Miranda

Delft University of Technology

TU Delft

Finite element analysis of flow liquefaction in a tailings dam using two advanced constitutive soil models

Geotechnical engineering master's thesis

in partial fulfilment of the requirements for the degree of

Master of Science
in Civil Engineering
Master Track: Geo-Engineering

at the Delft University of Technology,
to be defended publicly on August 29, 2023.

Author:	Victor Hugo Miranda Challapa	5378680
Thesis committee:	Dr. ir. R.B.J. Brinkgreve	TU Delft
	Dr. ir. S. Muraro	TU Delft
	Dr. ir. R.C. Lanzafame	TU Delft
	Dr. ir. A. Laera	Seequent

Cover: The tailings pond at the Syncrude mine north of Fort McMurray, Alberta, Canada by Ashley Cooper.

An electronic version of this thesis is available at http://repository.tudelft.nl/.

TU Delft PLAXIS SEEQUENT

Preface

This document represents the final work to fulfil the requirements to obtain my MSc Civil Engineering degree at the faculty of Civil Engineering and Geosciences at the Delft University of Technology.

This research aims to assess the capabilities and limitations of two constitutive soil models to analyse flow liquefaction in tailings dams. The models used are NorSand and CASM, whose implementation into the finite element software PLAXIS is verified and validated in this work to be applied in the simulation of laboratory tests and in boundary value problems, including the simulation of a flow liquefaction event. The thesis was conducted in collaboration with PLAXIS BV, where I worked for ten months as an intern, gaining invaluable experiences that made this thesis period a great time for professional and personal growth.

The fulfilment of this work was possible thanks to the support, guidance, and patience of several people from PLAXIS BV and TU Delft. First of all, I would like to express my gratitude to my daily supervisors at PLAXIS BV, Anita Laera and Ricardo Azeiteiro, for their willingness and patience in answering all my questions, for their advice in each one of the stages of the thesis and for sharing with me their knowledge and insights, which are invaluable learning for me. I would also like to thank Prof. R. Brinkgrave, Prof. R. Lanzafame, and Prof. S. Muraro for their willingness to be part of my evaluation committee and for their guidance and constructive feedback. Furthermore, I am thankful to Sandro Brasile, Tuan Bui and all the colleges at PLAXIS BV for the opportunity to be part of such a nice work environment.

This document means the end of an important stage of my life with great adventures and learning that would not have been possible without the support of my family. I will be forever grateful to my parents for their unconditional support and encouragement. Finally, I would like to thank each one of my friends who made this experience an amazing journey.

V.H. Miranda
Delft, August 2023

Abstract

Tailings dam failures are one of the most destructive phenomena in terms of the number of victims and the environmental impact generated. Over the years, different causes have been identified, with flow liquefaction being a prominent factor to consider when assessing the stability of tailings deposits. Due to the complex nature of these events, numerical models are considered an important alternative for the analysis and design phases of tailings dams. These models require the application of appropriate advanced soil constitutive models to reproduce the relevant features of the soil behaviour and, thus, obtain results that are a valid representation of the observations in reality. In this work, the capabilities and limitations of the Clay And Sand Model (CASM), originally proposed by Yu (1995, 1998) and NorSand model (Jefferies, 1993) are assessed using the finite element software PLAXIS in the analysis of flow liquefaction. The criteria considered in the assessment consist of the accuracy of the models to predict the response of the soil under different monotonic loading conditions, the efficiency of the models for their application and the consistency of results obtained from boundary value problems compared with reality.

Both CASM and NorSand are models developed within the critical state soil mechanics framework and use the concept of the state parameter (Been and Jefferies, 1985). However, they present differences in their formulations and assumptions. The performance of the model is explored in this study at three different levels: the material point level, simple boundary value problem level and complex boundary value problem. Different laboratory tests are simulated for the material point level, analysing a single stress point. For the boundary value problems, the construction of an embankment and the well-known Tar Island Dyke flow liquefaction event are simulated. Before applying the models, the implementation of CASM into PLAXIS is widely verified, and additional verification exercises for the NorSand implementation are also presented. Parametric analyses are performed to have a better insight into the effect of the parameters in the response of the models. Moreover, CASM and NorSand calibrated for the same tailings materials are used for the simulations.

Given that most of the model parameters can be estimated through very well established procedures using experimental data, in principle, the calibration of both models is relatively straightforward if the required experimental data is available and when the data is limited, correlations can be used to estimate the parameters of CASM assuming normally consolidated conditions, which is the state at which tailings are often found. The results of the thesis, at the material point level, show that CASM presents limitations to quantitatively predicting the response of dense materials. This is associated with the formulation and assumptions of the model. In the analysis of the boundary value problems, lower strengths and higher stiffness in terms of stress-strain response are obtained with CASM compared with NorSand. Despite these differences, the results of this thesis demonstrate that both CASM and NorSand can successfully reproduce flow liquefaction at the different study levels.

Contents

List of Figures

List of Tables

Nomenclature

Symbol	Definition	Unit
A	Fitting parameter	–
B	Fitting parameter	–
C	CASM plastic potential surface size parameter	–
C_a	Void ratio corresponding to a mean pressure equal to 0 kPa	–
C_b	Parameter of the power-law void ratio expression	–
C_c	Exponent of the power-law	–
c'_{ref}	Effective cohesion	kPa
E_{ref}	Effective Young's modulus	MPa
e_c	Void ratio at critical state	–
e_{ini}	Initial void ratio	–
e_{min}	Minimum void ratio	–
G	Shear modulus	MPa
G_{ref}	Reference shear modulus	MPa
H	Plastic hardening modulus	–
H_0	Hardening rule NorSand model parameter	–
H_ψ	Hardening rule NorSand model parameter	–
K	Bulk modulus	MPa
K_0	Lateral stress ratio	–
M	Stress ratio at critical state	–
M_{tc}	Slope of the CSL in the p' - q space for triaxial compression	–
M_i	Stress ratio at image condition	–
M_θ	Slope of the CSL in the p' - q that depends on the Lode's angle	–
m	Plastic potential shape controlling parameter	–
N	Exponent of the CASM viscosity formulation	–
N	NorSand volumetric coupling parameter	–
n	Stress-state coefficient	–
n_G	Exponent of the power-law elasticity	–
p'_c	Integration constant for the CASM plastic potential function	kPa
p'_i	Mean effective stress at image state.	kPa
p'_{ref}	Reference pressure	kPa
p'_x	Critical state mean effective pressure	kPa
p'_0	Preconsolidation pressure	kPa
R	Isotropic overconsolidation ratio	–
OCR	Isotropic overconsolidation ratio (MCC PLAXIS)	–
r	Spacing ratio	–
S	NorSand softening flag	–
S	Normalised undrained shear strength	–
S_p	Normalised peak undrained shear strength	–
$s_{u,peak}$	Peak undrained strength	kPa

Greek symbol	Definition	Unit
α	Parameter that controls the shape of the yield function in the deviatoric plane	–
Γ	Intersection of the CSL with a ref. pressure of 1kPa	–
γ_{sat}	Saturated unit weight	kN/m^3
γ_{unsat}	Unsaturated unit weight	kN/m^3
η	Stress ratio	–
η	CASM viscosity parameter	m^2 s kN^{-1}
θ	Lode's angle	$^\circ$
κ	Slope of the swelling line	–
λ	Slope of CSL	–
ν	Poissons's ratio	–
ϕ_{FLL}	Friction angle that characterises the slope of the flow liquefaction line	$^\circ$
ϕ'	Effective friction angle (Mohr-Coulomb model)	$^\circ$
ϕ_{cs}	Friction angle at critical state for triaxial compression	$^\circ$
ϕ_c	Critical state friction angle	$^\circ$
χ_{tc}	State-dilatancy parameter	–
ψ	Dilatancy angle	$^\circ$
ψ	State parameter	–
ψ_k	Characteristic state parameter	–
ψ_R	Reference state parameter	–
ψ_0	Initial state parameter	–

1 Introduction

1.1. Problem description

Tailings dam failures are one of the most recorded and destructive phenomena, both in terms of the number of victims and the environmental impact generated. For many years the overall number of tailings dams failure has declined. Nevertheless, in the last decades, the number of 'very serious' failures has increased (Bowker & Chambers, 2016). Moreover, a released assessment of global tailings management facilities carried out by the World Mine Tailings Failures (WMTF), indicates that there has been no improvement in the rate of significant failures. On the contrary, the rate of failures by billion tonnes of mining production increased from 0.09 to 0.1 in the last two decades, and their forecasts are not positive since they predict 18 'very serious' failures for the decade 2015 - 2024 and 13 failures between 2025 and 2029 (Lazenby, 2022). These data evidence the challenge and the importance that tailings dams represent for geotechnical engineers and other professionals in the area.

Different causes were identified as responsible for tailings dam failures, with overtopping and flow liquefaction being the most frequent. In fact, based on an information source of more than 250 tailings dam failures, (Piciullo et al., 2022) reported that more than 40% of the tailings dam failures were caused by these events; therefore, these are fundamental when designing or assessing tailings dams. Due to the complexity of these structures, numerical models are often applied in the design and evaluation phases, where advanced soil constitutive models are used to reproduce the most important features of the behaviour of soils. In this study, the models NorSand (Jefferies, 1993) and Clay And Sand Model (CASM) (Yu, 1998) are considered. Their formulation is based on the Critical State Soil Mechanics framework (Schofield & Wroth, 1968), and the determination of their model parameters can be estimated with conventional laboratory tests. These soil constitutive models have been selected since they are able to simulate flow liquefaction, among other soil characteristics. Their formulations present similarities, as well as differences, which may reflect on the simulated soil response in boundary value problems.

1.2. Objective

The main objective of the project is to assess the capabilities and limitations of NorSand and CASM to analyse flow liquefaction in tailings dams using the geotechnical finite element software PLAXIS.

During the assessment of the models, three main criteria will be considered:

- The efficiency of the models for their application in terms of model parameters calibration.
- The accuracy of the constitutive models to reproduce or predict the response of the soil under different stress paths considering monotonic loading conditions (quantitative and qualitative).
- The consistency of the boundary value problem results with the reported observations and/or data available from the liquefaction failure in reality.

1.3. Research questions

To achieve the objective, research questions and sub-questions are formulated in such a way that their answers allow to obtain information used in the evaluation of the models. The research questions and sub-questions which conduct the development of the present project are:

- What are the differences between NorSand and CASM in terms of formulation and soil response prediction under monotonic loading?
  - Do the available numerical implementation of the models in PLAXIS correspond to their analytical formulation?
  - What is the effect of the particular parameters of each model on their response?
  - What are the strategies followed to calibrate the model parameters? Can the model parameters be estimated from standard laboratory tests (i.e. triaxial tests, oedometer tests, etc.)?
- To what extent the important features of the behaviour of loose sand and tailings are captured by NorSand and CASM?
  - What are the most important features of the behaviour of loose sand and tailings?
  - How accurately do the models predict the response of loose sand and tailings under different laboratory test conditions?
  - What is the effect of the different formulations and assumptions considered by the models on their results?
- What is the performance of CASM and NorSand in a flow liquefaction finite element analysis?
  - What are the boundary conditions that have to be considered for the flow liquefaction study case?
  - Do the results of the numerical simulations represent the failure observed and reported in reality?
  - What differences and limitations can be identified in the results of the numerical simulation?

1.4. Research approach

The methodologies and procedures followed during the research are divided into stages as follows:

- **Literature review**
  This is the start of the project, which consists in researching, studying, and organising the available and necessary theoretical framework to respond to the research questions. Flow liquefaction and soil constitutive models (i.e. NorSand and CASM) will be the main topics to be studied.

- **Models verification**
  In this phase, the numerical implementations of the constitutive models in PLAXIS will be verified through the comparison of simulation results against analytical formulation results or the results of other numerical implementations already verified that can be found in the literature.

- **Sensitivity analysis**
  A sensitivity analysis will be carried out to analyse the influence of the parameters and the stress state in the models' response.

- **Models validation**
  The next phase of the research will be the validation of the models, which includes the calibration of the model parameters. Once the models are calibrated for a certain type of soil, laboratory test simulations will be performed, and their results will be compared with experimental data to validate the models. In this phase, it is expected to identify the differences between the response of the models when predicting the response of the same type of soil.

- **Boundary value problem application**
  Finally, a boundary value problem will be simulated with NorSand and CASM, and the results will be analysed, taking into account not only the model's results but also the failure mechanism in reality. In this stage, the boundary conditions and the trigger for liquefaction will be defined, as well as the effect of the components of a finite element analysis (e.g. discretisation).

- **Result analysis**
  The analysis of the results of each one of the previous stages will lead to the final conclusions and recommendations.

Note that during the study, the analysis of the models is carried out at the local and global levels. The local corresponds to the analysis of a single stress point where only the constitutive models are involved, while the global involves a complete boundary value problem which includes not only the constitutive models but also the components of a finite element method model.

2

Literature Review

2.1. Introduction

The mining industry generates huge volumes of waste tailings every year, which are stored in tailings dams. These storage facilities are required to remain stable and, ideally, not cause any detrimental damage to the environment, making them a fundamental component of the mining industry for environmentally sustainable tailings management. Unfortunately, despite the many advances in the mining sector and the geotechnical field, during the last decades, several significant tailings dam failures have occurred in different parts of the world, resulting in extensive and irremediable damage to the environment and the loss of hundreds of human lives. One of the main causes of these failures is flow liquefaction. Davies et al. (2002) describes several case histories of tailings dam failures due to flow liquefaction highlighting the importance of understanding this phenomenon. Even though it is widely studied, there are still uncertainties and controversy regarding some aspects of the phenomenon. In the present chapter, an overview of tailings dams failures and flow liquefaction is presented.

2.2. Tailings

Tailings are the waste materials left after the process of extracting minerals. These consist of a mixture of sand, silt, and water with high content of metals and chemicals employed during the mining processes. These materials are usually stored as slurry in dams or embankments. Figure 2.1 depicts the process of mining extraction and tailings storage.

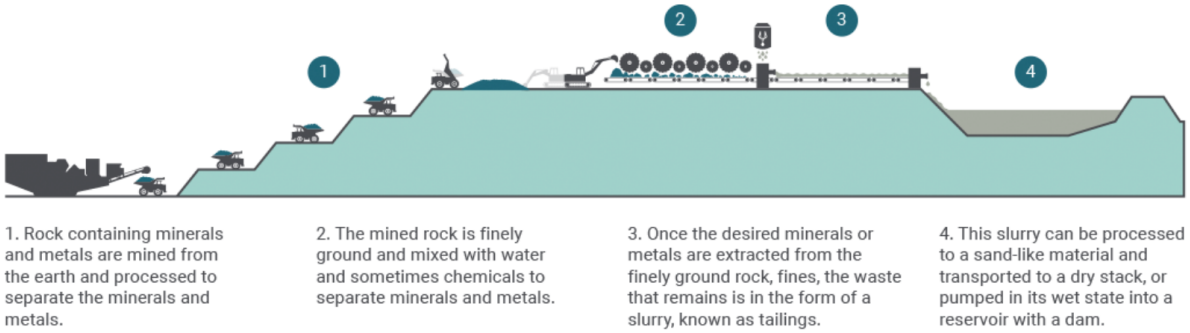

Figure 2.1: Tailings formation and storage (source: globaltailingsreview.org).

The engineering behaviour of tailings is determined by the characteristics of the material itself, the nature of the ore and the processing methods applied. The permeability of tailings is subject to grain size, plasticity, and depositional method, and it spans five or more orders of magnitude from 10^{-2}cm/sec to 10^{-7}cm/sec, which makes it a property difficult to generalize (Vick, 1990). Due to the loose depositional state and high angularity, tailings are generally more compressible than the corresponding types of

natural soils, and their drained shear strength is often higher, compared to similar natural soils. On the contrary, undrained shear strength and cyclic strength depend on the density of the material and are of fundamental importance when evaluating the susceptibility of tailings to failure.

2.3. Tailings dams

Tailings dams are earth-fill structures used to store mining waste, which comes from extracting and processing mineral resources that include solid, semisolid and liquid waste material. Tailings dams can be huge in size, reaching more than 80 m in height with a great amount of volume storage capacity. In the last two decades, the growth of the mining industry has been reflected in the number of tailings dams. There is no accurate record of the number of tailings dams in the world. However, Davies and Martin (2000) estimated 3500 tailings dams in the year 2000, which currently is far from the reality since Kun et al. (2018) indicates that there are 8869 tailings dams in China and Lumbroso et al. (2019) indicates that in South America approximately 1200 mines with tailings dams are in operation while in the USA there are over 1400 tailings dams.

2.3.1. Construction methods

Contrary to water-retention dams, tailings dams are not constructed to their full height before their operation. Tailings dams are usually built gradually and operated during the building phases. The construction of a tailings dam can take decades and is subject to the volume of waste. As the volume of waste increases, different construction methods can be used to raise the dams and, therefore, enlarge the storage capacity.

1. **Upstream construction method**

   This method consists in constructing an initial starter dam, while tailings are discharged from the crest to form a tailings beach. Drains are installed to allow this beach to consolidate, which is then used as the foundation for subsequent dam levels, as it can be seen in Figure 2.2. In this way, the crest of the dam moves upstream with each raise. This method is the most widely used. In fact, prior to the 1980s, all mine tailings dams were constructed using this method (ICOLD, 1989). The major advantages of the upstream method are the cost and simplicity since tailings are reused in the construction, and the amount of material required for raising is smaller than the one needed for the other methods. However, this method is limited to very specific conditions and implies disadvantages related to groundwater table control, water storage capacity, and liquefaction susceptibility (Vick, 1990).

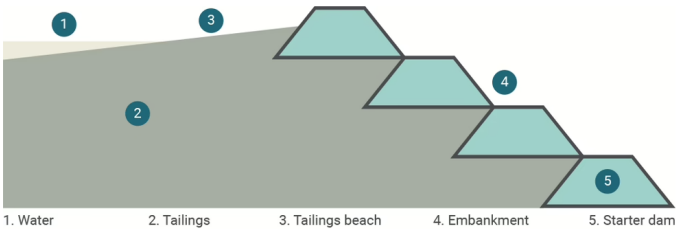

Figure 2.2: Upstream construction method (source: globaltailingsreview.org).

2. **Downstream construction method**

   The downstream construction method was developed as an alternative to the upstream method since tailings dams constructed with this last method present a high risk of failure, especially when subject to dynamic loads (ICOLD, 2001). As the name implies, the downstream method increases the height of the dam by progressing the crest of the dam downstream from the starter dam, as it can be seen in Figure 2.3. In contrast to upstream dams, which are built progressively on tailings, downstream dams are built on prepared and compacted material. Moreover, this method allows the incorporation of additional dam elements, such as impervious cores and internal drains, which enhances the phreatic surface control. These elements are described by Caldwell and Smith (1985), who also point out that downstream embankments may be chosen in preference to upstream or

centreline dams, especially for seismic, wet, or sensitive areas.
The major disadvantage of the downstream raising method is the comparatively large volume of embankment fill required and the high cost that this implies (Vick, 1990). In fact, a downstream dam may cost three to nine times as much as a centreline dam (Caldwell & Smith, 1985).

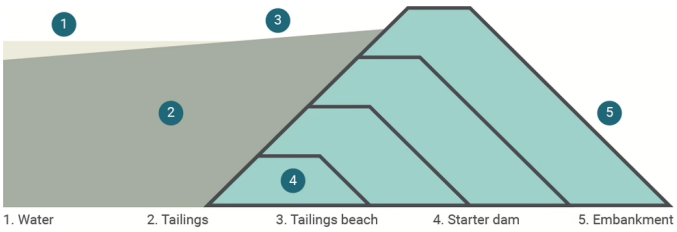

Figure 2.3: Downstream construction method (source: globaltailingsreview.org).

3. Centreline construction method

This method combines the characteristics of both previous methods in order to benefit to a certain extent from their advantages and reduce their disadvantages. Similar to the upstream method, this method employs a starter dam, and tailings are peripherally stored from the dam crest forming a tailings beach. Subsequently, the dam height is increased by placing fill onto the beach and the downstream slope of the previous raise, as shown in Figure 2.4. Since internal drainage zones can be provided within the dam by applying this method, the saturation levels can be controlled reducing the risk of failure. Additionally, the volume of fill required for raising the dam is intermediate between that for upstream and downstream methods, also resulting in intermediate costs (Vick, 1990).

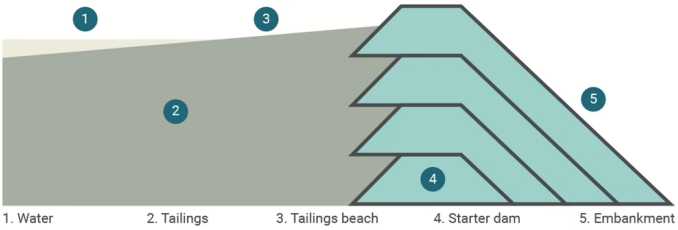

Figure 2.4: Centreline construction method (source: globaltailingsreview.org).

2.3.2. Tailings dam failures

Tailings dam failures are one of the most recorded and destructive events in terms of victims and the environmental impact generated both in the short and long term. Since 1915, a total of 257 tailings dam failures have been recorded, with around 2650 fatalities and 250 million m^3 of contaminated residues released to the environment from which almost 50% (115 million m^3) have been recorded after 2000 with around 640 fatalities (Piciullo et al., 2022). Despite many attempts and investments in improving tailings management and due to the climate change effects, tailings dam failures remain the most significant environmental disaster threat related to mining (Roche et al., 2017).

Causes of failures

The lack of knowledge on tailings behaviour, together with the few monitoring and management measures, can be considered as the predisposing factors of tailings dam failures (Piciullo et al., 2022). An interesting analysis carried out by Piciullo et al. (2022), which is based on the data of 257 tailings dam failures provided by CSP^2 (Centre for Science in Public Participation), indicates that a great number of the failures happened in tailings dams constructed with the upstream method (32%). Moreover, there is a large number of cases where the method of construction is unknown (49%). A chart of dam failures by dam construction method can be seen in Figure 2.5, where it can be observed that the majority of tailings dam failures for which the construction method is known, is by the upstream method.

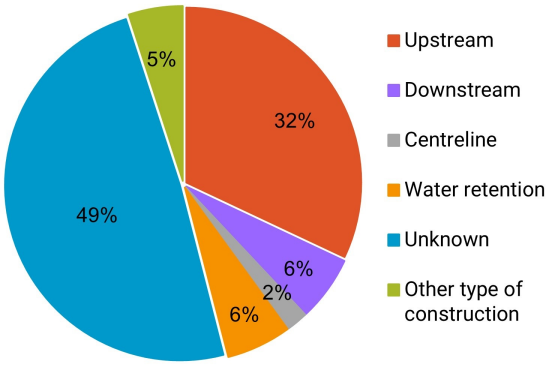

Figure 2.5: Reported tailings dam failures by dam construction (data from Piciullo et al. (2022)).

ICOLD (2001) classifies the cause of tailings dam failures into nine categories, which are: static failure, seepage and internal erosion, structural and foundation conditions, overtopping, structural inadequacies, seismic instability, mine subsidence, external erosion, and unknown. Based on this classification, Figure 2.6 shows a summary of 257 tailings dam failures recorded from 1915 to 2021, where it can be noted that overtopping, static failure and failures whose cause is unknown are the cause of more than 50% of tailings dam failures.

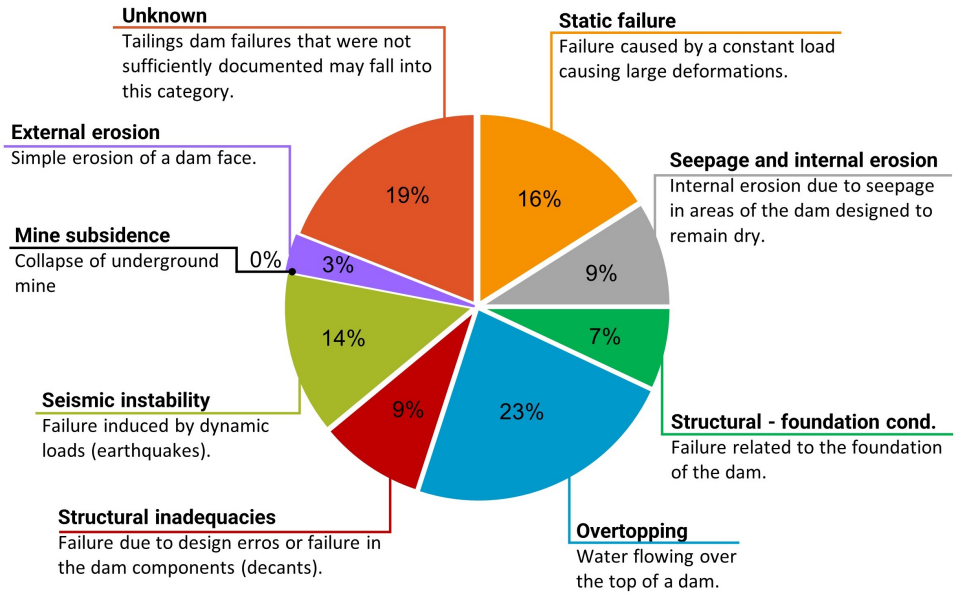

Figure 2.6: Reported causes of tailings dam failures (data from Piciullo et al. (2022)).

2.3.3. Flow liquefaction in tailings dams

Within the ICOLD (2001) classification of tailings dam failure causes, it can be observed that some causes are events that may trigger or are a consequence of flow liquefaction (i.e. seepage, overtopping, and static failure), making this phenomenon (explained in section 2.4) a main concern in tailing dam failures. In the literature, several tailings dam failures whose main cause is reported to be flow liquefaction triggered by a single event or a combination of events such as overtopping and rainfall are reported. Some of them are summarized in the following lines.

In 1994, the Merriespruit gold tailings dam in South Africa collapsed, resulting in 17 fatalities and 600000 m^3 of volume released. An investigation carried out by Fourie et al. (2001) concluded that static liquefaction triggered by an overtopping event was the cause of the flow slide failure. It is re-

corded that an overtopping event happened before the flow slide, which is considered the trigger event since this would have eroded part of the outer slope of the impoundment, causing slip failures that exposed contractive tailings to undrained loading and triggering flow liquefaction. Another recent and catastrophic tailings dam failure took place in Brumadinho (Brazil), where the Feijão Dam I failed due to flow liquefaction (P. K. Robertson et al., 2019) leaving more than 200 fatalities and 12 million m^3 of highly toxic mud released. In this case, it is reported that flow liquefaction within the tailings in the dam was triggered by internal strains due to creep and a strength reduction due to loss of suction caused by cumulative rainfall.

Flow liquefaction is a major issue for tailings dams during the design, operational, and non-operational phases due to the contractive characteristics of tailings and the tailings dam conditions. Aspects such as the construction method, monitoring, and the location of the dam are fundamental during the flow liquefaction assessment since a trigger event, which is often dependent on the previous aspects, is necessary for liquefaction to occur.

2.4. Soil liquefaction

Terzaghi and Peck (1948) defined liquefaction as the sudden loss of strength of very loose sands that caused flow failures triggered by slight disturbance. This phenomenon is considered a major problem when dealing with cohesionless soil material, especially in seismic areas and for the design of large structures such as tailings dams (P. Robertson, 1997). The term liquefaction covers different physical phenomena, such as flow liquefaction and cyclic mobility, which are described below.

2.4.1. Flow liquefaction

Flow or static liquefaction is the process of strain-softening of contractive and cohesionless soils under undrained or partially undrained conditions leading to a flow failure. The sudden loss of strength that occurs in flow liquefaction can be caused if a contractive volume change occurs rapidly, and pore water pressure may not have time to drain, resulting in undrained shearing. This phenomenon can be triggered by static undrained loading (e.g., rapid loading), dynamic loading (e.g., earthquakes), and unloading (e.g., a rise of groundwater table) occurring if the residual strength of a soil is lower than the one required to maintain static equilibrium (Kramer & Elgamal, 2001). Figure 2.7 shows possible stress paths leading to flow liquefaction, where the stress path A-B-C corresponds to a static undrained loading, the stress path A'-E-C corresponds to dynamic loading, and the stress path A-D-C corresponds to a deformation under shear stress that is larger than the liquefied shear strength (i.e. creep).

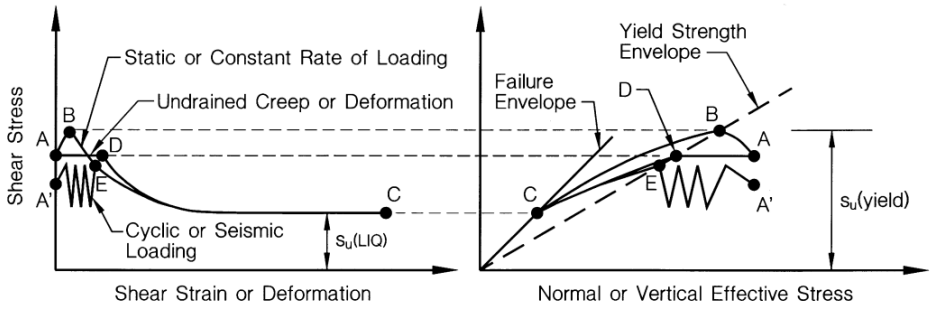

Figure 2.7: Schematic undrained response of a saturated, contractive sandy soil (Olson, 2001).

2.4.2. Cyclic mobility

Cyclic mobility is the phenomenon in which cyclic loading induces excess pore water pressures in a soil whose residual strength is greater than the one required to maintain static equilibrium (Kramer & Elgamal, 2001). Cyclic mobility can occur in almost all sands provided that the cyclic loading is large enough in amplitude and duration. Generally, it is observed in the field in the form of lateral spreading (e.g., Failure of Showa River bridge in Niigata, Japan, 1964) and level ground deformations such as sand boils. Figure 2.8 shows three different cases of cyclic mobility in the stress state space.

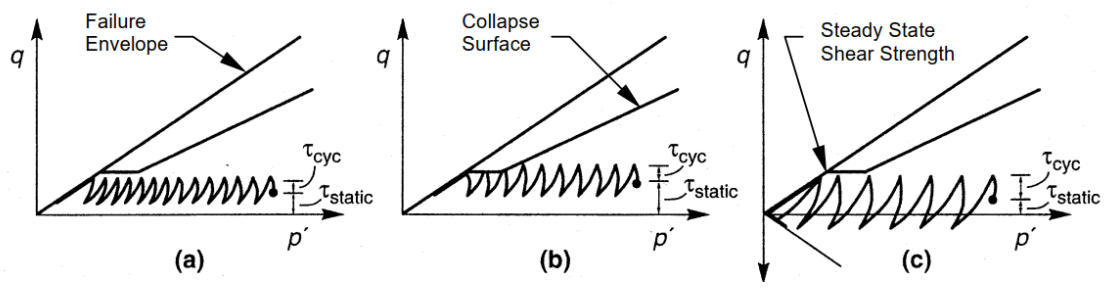

Figure 2.8: Three cases of cyclic mobility: (a) no stress reversal and no exceedance of the steady-state strength; (b) no stress reversal with momentary periods of steady-state strength exceedance; (c) stress reversal with no exceedance of steady-state strength. (Kramer, 1996).

2.4.3. Flow liquefaction assessment

Collapse surface approach

As a result of a back analysis from the Nerlerk berm liquefaction slides due to static loads (1983), Sladen et al. (1985) introduced the concept of a collapse surface in the three-dimensional e, p', q space. This concept is developed into a method of analyzing the loss of limiting equilibrium due to liquefaction.

The concept of collapse surface arose from the observation that the peak strengths of effective stress paths from undrained triaxial tests fall on a single straight line, which changes its position only with the variation in the void ratio. This line represents the collapse surface and is illustrated in Figure 2.9. Sladen et al. (1985) indicates that for liquefaction to occur, the soil state has to reach the collapse surface, and the deviatoric stress must exceed the steady state shear strength under undrained conditions. For loose sand whose state lies on the collapse surface, minimal excess pore pressure is enough to trigger liquefaction. Note in Figure 2.9 that the final steady state is the same for the samples since the void ratio is the same, while for samples at different void ratios, the shape of the stress path will be similar, but the final steady state will differ.

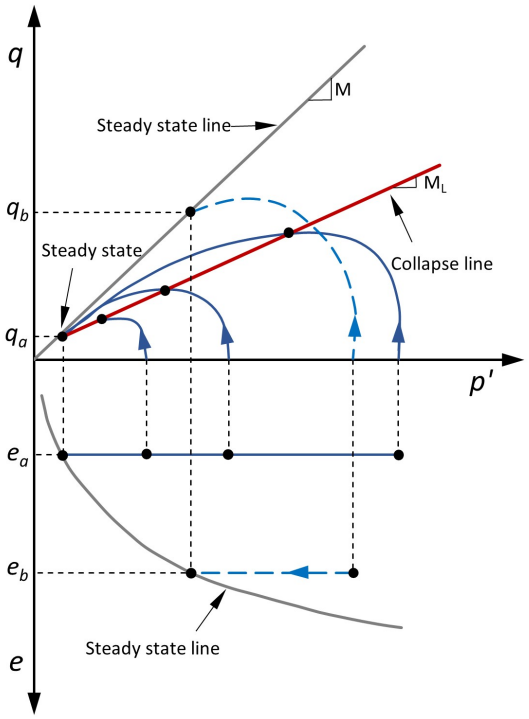

Figure 2.9: Schematic illustration of the collapse line concept (Altered from Sladen et al. (1985)).

In order to compare data from different tests and determine a single collapse surface for samples with varying void ratios, a normalization of the effective stress paths dividing the stresses by the stress at the steady or critical state at the same void ratio is suggested by Sladen et al. (1985) as can be seen in Figure 2.10, which shows the normalized stress paths for the Leighton Buzzard sand and a single collapse line.

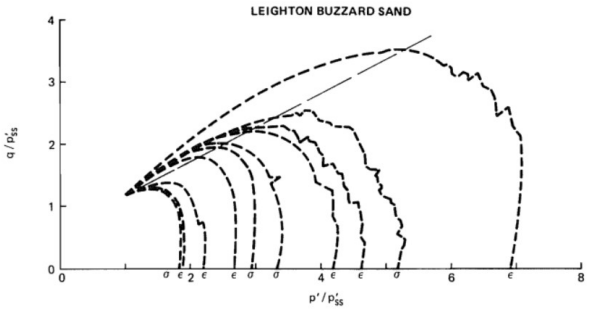

Figure 2.10: Normalized stress paths for Leighton Buzzard sand and collapse line (Sladen et al., 1985).

The application of the collapse surface concept to liquefaction analysis presents advantages over the steady-state approach described in detail by Castro et al. (1982). In the liquefaction analysis, failure occurs at deviatoric stress levels higher than the steady-state shear strength. Moreover, the steady-state approach does not allow the estimation of the magnitude of the required force to trigger liquefaction. These aspects do not invalidate the steady-state approach as a design method; however, they make it inappropriate for the back analysis of liquefaction failures (Sladen et al., 1985). The collapse surface can be defined in terms of parameters analogous to a Mohr-Coulomb failure criterion, which allows its application in limit equilibrium analysis to evaluate liquefaction potential (further information can be found in Sladen et al. (1985)). For this, only the steady-state shear strength and the slope of the collapse line (M_{L}) are the data needed.

Flow liquefaction line approach

Similar to the collapse surface concept, Lade (1993) proposed to identify the flow liquefaction line (FLL) as the locus of peak points in the effective stress paths passing through the stress origin. Figure 2.11 displays an illustration of the comparison between the collapse line and the flow liquefaction line.

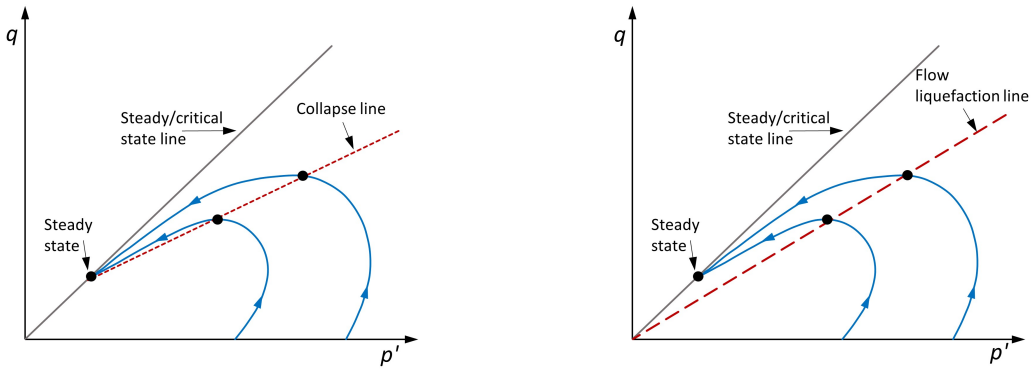

(a) Collapse line. **(b)** Flow liquefaction line.

Figure 2.11: Comparison of collapse line and instability or flow liquefaction line.

Analysing the experimental tests by Sladen et al. (1985) and Ishihara (1993), Yang (2002) showed that the flow liquefaction line is not unique but varies with the state of the soil. Additionally, it was observed that the slope of the flow liquefaction lines increases with decreasing confining pressures and it is limited by the critical state line. Figure 2.12 shows the stress paths of the Leighton Buzzard sand and flow liquefaction lines with different slopes.

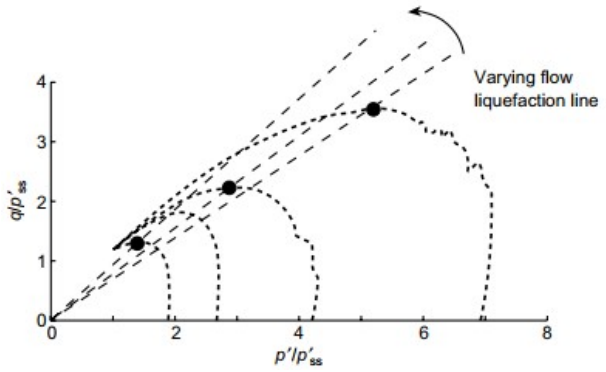

Figure 2.12: Normalized stress paths for Leighton Buzzard sand and varying flow liquefaction line (Yang, 2002).

Based on the state parameter concept, which is further explained in section 3.3, and the peak stress ratio, a relationship was proposed by Yang (2002) and is expressed in the following form:

$$\left(\frac{q}{p'}\right)_{peak} = \frac{M}{B}\exp\left(A\psi\right) \tag{2.1}$$

Where A and B are fitting parameters, M is the stress ratio at critical state, and ψ is the state parameter. A must be lower than zero, while B must be larger than 1. A procedure to calibrate the parameters based on experimental data can be found in Yang (2002). Based on Eq. 2.1 a friction angle, ϕ_{FLL}, characterising the slope of the flow liquefaction line (FLL) can be introduced as:

$$\sin\phi_{\mathrm{FLL}} = \frac{3\left[\frac{M}{B}\exp\left(A\psi\right)\right]}{6+\left[\frac{M}{B}\exp\left(A\psi\right)\right]} \tag{2.2}$$

From the experimental data and Eq. 2.2, it can be noted that the flow liquefaction angle decreases with increasing values of the state parameter ψ. In other words, the looser the sand, the smaller the slope of the flow liquefaction line. This line separates the liquefaction process into stable and unstable states in the p'- q space. Therefore, if a soil stress condition reaches the flow liquefaction line, flow liquefaction is triggered, and the shear strength will rapidly reduce.

Flow liquefaction is a complex phenomenon that definitely still requires further research for a better understanding and evaluation. Been and Jefferies (2004) investigated the behaviour of loose sands questioning the concept of 'collapse surface', and based on drained triaxial tests and the stress-dilatancy concept, it has been demonstrated that loose sands show a stress-dilatancy behaviour similar to that of dense sand and no evidence for a collapse surface in effective stress friction terms was found. As an alternative, Been and Jefferies (2004) indicated that the flow rule characterising the Cam-clay model (Schofield & Wroth, 1968) could be taken as a starting point for modelling sand behaviour since the stress-dilatancy relationship considered by the model seems close to the one observed experimentally.

The next chapter presents two constitutive models that were developed based on the Cam-clay model and are able to simulate flow liquefaction.

3

Constitutive models for flow liquefaction

3.1. Introduction

Numerical modelling has become a universal and valuable tool in geotechnical engineering to understand and predict the behaviour of geotechnical structures and interaction phenomena. The selection of a constitutive model able to reproduce the behaviour of the soil accurately plays a key role in the success of the numerical simulation.

The numerical analysis of flow liquefaction requires advanced constitutive models able to capture and reproduce the rapid reduction of strength and stiffness characteristic of this phenomenon. Specifically for flow liquefaction, Jefferies and Been (2006) states that the basic premise of a proper constitutive model is that this must capture the effect of the density on the modelled response of the material, which has been proved to affect the behaviour of soils drastically. With such objective, a state parameter approach (Been & Jefferies, 1985) has often been used in conjunction with the Critical State Soil Mechanics theory (Schofield & Wroth, 1968) to develop models capable of simulating the conditions and consequences of flow liquefaction and be used in the analysis of geotechnical structures susceptible to this phenomenon. In this chapter, the concepts, formulations, and parameters of two different critical state constitutive models able to reproduce flow liquefaction are presented.

3.2. Critical State concept

The Critical State concept has been used to describe and predict important features of the mechanical behaviour of soils. Schofield and Wroth (1968) describe the concept of critical state in the following way: the concept that soil and other granular materials, if continuously distorted until they flow as a frictional fluid, will come into a well-defined critical state determined by two equations characterised by a unique relationship between the specific volume, v, and the mean effective stress, p', as well as between deviatoric stress, q, and p' as follows:

$$q = M \cdot p' \tag{3.1}$$

$$\Gamma = v + \lambda \cdot \ln p' \tag{3.2}$$

Where the constants M, Γ, and λ represent basic soil properties, whose meaning is shown in Figure 3.1 and the parameters q, p', and v define the state of the material. Equation (3.1) determines the magnitude of deviatoric stress required to keep the soil flowing continuously, and equation (3.2) states that the specific volume will decrease as the logarithm of effective mean stress increases. The specific volume, v can be related to the void ratio, e, as shown in equation (3.3).

$$v = 1 + e \tag{3.3}$$

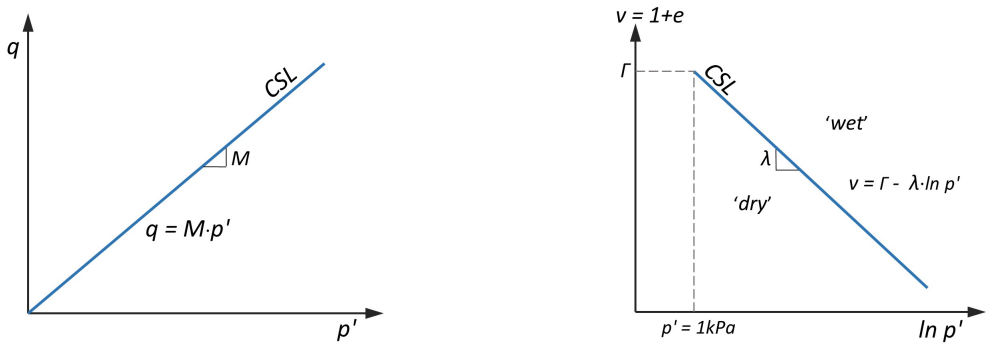

(a) Critical state line in the stress state space.

(b) Critical state line in the $\ln p'$ - v space.

Figure 3.1: Critical state lines.

As further explained by Schofield and Wroth (1968), the equations above indicate that at critical state, yielding occurs at constant volume and constant stresses. This further means that the plastic volumetric strain increment is zero at the critical state since elastic strain increments will be zero due to the constant stress condition at the critical state, assuming that the strains can be split into elastic and plastic components.

If the effective mean stress and the specific volume of a given soil at any point during the loading process are plotted, the current soil's state can be represented by a single point in the ($\ln p'$, v) space and compared with the reference state provided by the critical state line (CSL). In this space, the soil is looser than the critical state when it falls above the CSL, in the so-called 'wet' zone, while it is denser than the critical state when it falls below the CSL, in the so-called 'dry' zone (Figure 3.1b shows both zones). On the 'wet' side, the soil needs to contract to reach the critical state (the term 'wet' comes from the fact that the sample needs to expel water), while on the 'dry' side, the soil needs to dilate to reach the critical state (and, therefore, the soil needs to absorb water). The amount of dilation and contraction depends on how far the current state is from the critical state (Schofield & Wroth, 1968).

For simplicity, the formulations of the critical state models described in this chapter are presented for triaxial conditions, where two of the principal effective stresses are equal, and the directions of principal effective stresses are fixed with respect to the sample. Note that all the formulations presented in this study are in terms of effective stresses. Assuming compressive stresses and strains as positive, the following stress and strain invariants are used:

$$p' = \frac{1}{3}(\sigma'_1 + 2\sigma'_3) \quad ; \quad q = \sigma'_1 - \sigma'_3 \tag{3.4}$$

$$\varepsilon_{vol} = \varepsilon_1 + 2\varepsilon_3 \quad ; \quad \varepsilon_q = \frac{2}{3}(\varepsilon_1 - \varepsilon_3) \tag{3.5}$$

3.3. State parameter

The state parameter (ψ) introduced by Been and Jefferies (1985) is defined as the difference between the current void ratio and the void ratio at critical state for the current mean effective stress, as shown by equation 3.6 and illustrated in Figure 3.2. This parameter measures the state of the soil, which can exist in a wide range of densities and stress states, taking into account as a reference the critical state line (CSL). When a soil has a contractive behaviour (i.e. loose soil), the state parameter is positive, while when the soil behaviour is dilative (i.e. dense soil), the state parameter is negative.

$$\psi = e - e_c \tag{3.6}$$

The importance of the state parameter arises from the fact that, contrary to the void ratio or density, it takes into account the stress levels, which influence the dilatancy (the higher the effective stress that a sample is subjected to, the lesser the tendency to dilate). It is the dilation which influences the strength, not the void ratio or density at which dilation occurs (Jefferies & Been, 2015). Therefore, the state

parameter is fundamental to constitutive models of soil since it provides a simple and effective form of predicting the occurrence of key features of the response of soil (e.g. its peak strength) for a wide range of densities and effective stress states.

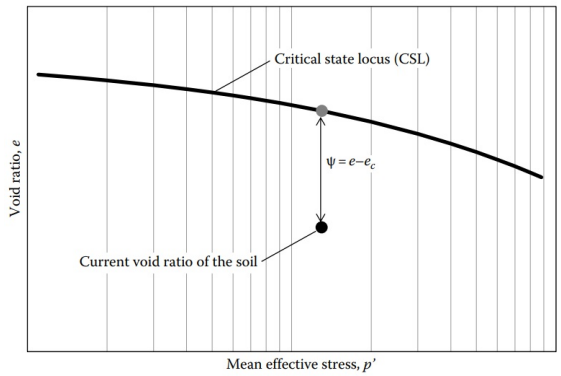

Figure 3.2: State parameter definition (Jefferies & Been, 2015).

3.4. Clay And Sand Model (CASM) (Yu, 1998)

The Clay and Sand Model (CASM) was originally proposed by Yu (1998). This model is based on the critical state theory (Schofield & Wroth, 1968) and formulated in terms of the state parameter concept (Been & Jefferies, 1985). Yu's philosophy behind the development of the constitutive model is that simplicity should be paramount and that the material parameters required by the model should be easily measurable, whenever possible, having conventional values. Moreover, the proposed model is formulated in such a way that the standard Cam-clay models can be recovered simply by choosing specific values for some model parameters.

In order to understand the main principles of the CASM, the formulation of the Original Cam-clay (OCC) and Modified Cam-clay (MCC) - the first series of models proposed within the Critical State Soil Mechanics framework - are presented in terms of the state parameter in the next lines.

3.4.1. Cam-clay models in terms of the state parameter

Original Cam-clay model

As the earliest elastic-plastic critical state model, the OCC was developed by Roscoe and Schofield (1963) and Schofield and Wroth (1968). Later, Yu (1998) showed for the first time that OCC and MCC take a simpler form if formulated in terms of the state parameter. The material behaviour prior to reaching the critical state in the $\ln p'$ - v space is assumed to be controlled by the state parameter, which is defined by equation (3.7) in terms of specific volume and mean effective stress.

$$\psi = v + \lambda \cdot \ln p' - \Gamma \tag{3.7}$$

The state boundary surface which defines a boundary in the effective stress - void ratio space above which no effective stress state can exist of the original Cam-clay model is presented by Schofield and Wroth (1968) as:

$$\frac{q}{Mp'} = \frac{\Gamma + \lambda - \kappa - v - \lambda \cdot \ln p'}{\lambda - \kappa} \tag{3.8}$$

Using equations (3.7) and (3.8) the boundary surface can be expressed as a relationship between the stress ratio and the state parameter. Where $\eta = q/p'$ is known as stress ratio and the boundary surface is formulated as:

$$\frac{\eta}{M} = 1 - \frac{\psi}{\psi_R} \tag{3.9}$$

Where ψ_R is a positive reference state parameter defined by Eq. (3.10) that denotes the vertical distance between the CSL and the reference consolidation line (which is assumed to be parallel to the CSL, as shown in Figure 3.3, and has been typically referred to as normal consolidation line within the context

of Cam-clay model), while r is the spacing ratio defined as the Euler's number in the OCC model. As also shown in Figure 3.3, r is given by the ratio of p'_0, which defines the value of p' at the intersection of the current swelling line with the reference consolidation line (RCL), to p'_x, which defines the value of p' at the intersection of the current swelling line with the CSL.

$$\psi_R = (\lambda - \kappa) \ln r \tag{3.10}$$

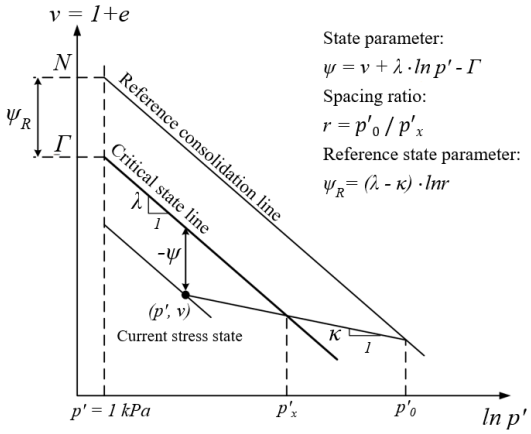

Figure 3.3: State parameter, critical state parameters, and reference state parameter definitions (Yu, 2006).

It should be noted that, in this constitutive model, the state boundary surface is employed as yield surface (which defines the boundary between purely elastic and elasto-plastic response). Moreover, the model is associated, which means that the plastic potential surface coincides with the yield surface.

Modified Cam-clay model

The state boundary surface of the MCC was originally formulated by Roscoe and Burland (1968) as given by equation (3.11). Yu (1998) showed that it is possible to re-write this equation as a function of the state parameter as shown in equation (3.12).

$$\left(\frac{q}{Mp'}\right)^2 = \exp\left(\frac{N + v - \lambda \cdot \ln p'}{\lambda - \kappa}\right) - 1 \tag{3.11}$$

$$\left(\frac{\eta}{M}\right)^2 = 2^{\left(1 - \frac{\psi}{\psi_R}\right)} - 1 \tag{3.12}$$

Unlike the linear stress-state relation suggested by the Original Cam-clay model (Eq. 3.9), the modified stress-state relationship defined by Eq. (3.12) is nonlinear. The spacing ratio, r, is defined to be equal to 2 in the MCC model.

3.4.2. CASM Formulation

Contrary to many other existing critical state models that use different formulations for clay and sand, CASM attempts to establish a unified formulation by using a general stress-state relation (Eq. 3.13). By inspecting this equation, it can be concluded that it is the normalized state parameter, ψ/ψ_R, rather than the state parameter itself that controls the size of the yield surface.

$$\left(\frac{\eta}{M}\right)^n = 1 - \frac{\psi}{\psi_R} \tag{3.13}$$

Where n is a new material parameter which typically ranges between 1.0 - 5.0 and the reference state parameter can be calculated by using Eq. (3.10). In this equation, note that, rather than being a constant as in OCC and MCC, the spacing ratio is now a model parameter. In addition, note that its value is generally much higher for sand than for clay (Coop & Lee, 1993).

It is also noteworthy that the OCC model (Eq. 3.9) can be recovered from Eq. (3.13) by selecting $n = 1$ and $r = 2.7183$. Likewise, the 'wet' side of the MCC model can be matched by choosing $r = 2$ in conjunction with a suitable value for n (around 1.5 - 2.0). From Figure 3.3, it can be shown that:

$$\frac{\psi}{\psi_R} = \frac{-(\lambda - \kappa) \cdot \ln\left(p'_x/p'\right)}{(\lambda - \kappa) \cdot \ln r} = 1 + \frac{\ln\left(p'/p'_0\right)}{\ln r} \tag{3.14}$$

Moreover, by substituting Eq. (3.14) into the general stress-state relation, a generalised yield surface in terms of the preconsolidation pressure, p'_0, and the spacing ratio, r, is obtained, as given by Eq. (3.15).

$$\left(\frac{\eta}{M}\right)^n = -\frac{\ln\left(p'/p'_0\right)}{\ln r} \tag{3.15}$$

Original formulation by Yu (1998)

The original formulation of CASM proposed by Yu (1998) is presented in this section. The modifications introduced by Arroyo and Gens (2021) when implementing CASM as a UDSM in PLAXIS will be detailed later.

• Elastic behaviour

As in the standard Cam-clay models, CASM assumes that the bulk modulus K is proportional to the mean effective pressure p':

$$K = \frac{vp'}{\kappa} \tag{3.16}$$

The second elastic constant is determined by assuming either a constant value for the Poisson's ratio, ν, as shown by Eq. (3.17) or a constant value for the shear modulus, G. The first alternative prevents obtaining unrealistic negative values for the coefficient of Poisson. Therefore, the shear modulus is assumed to vary with mean effective stress.

$$G = \frac{3(1 - 2\nu)}{2(1 + \nu)} K \tag{3.17}$$

• Yield surface

The general stress-state relation defined by equation (3.18) is adopted to describe the behaviour of soil yielding in terms of the effective mean and deviatoric stresses, as well as the state parameter.

$$f(p', q, \psi) = \left(\frac{q}{Mp'}\right)^n + \frac{\psi}{\psi_R} - 1 = 0 \tag{3.18}$$

Where M is the slope of the CSL in the p' - q plane and n is a parameter that controls the shape of the yield surface. Using Eq. (3.18), the yield function can also be formulated in terms of the mean yield stress, p'_0, and the spacing parameter, r, by the substitution of Eq. (3.14) in Eq. (3.18).

$$f(p', q, p'_0, r) = \left(\frac{q}{Mp'}\right)^n + \frac{1}{\ln r} \cdot \ln\left(\frac{p'}{p'_0}\right) = 0 \tag{3.19}$$

As mentioned before, the CASM formulation is formulated in such a way that the standard Cam-clay models can be recovered by selecting a specific value for the parameters n and r as illustrated in Figure 3.4a. It can be noted that while matching perfectly the yield surface of OCC, there are some differences between the yield surface of MCC and that of CASM when $r = 2$ and $n = 1.75$, particularly on the 'dry' side that may lead to different responses for dense sand and overconsolidated clay, more specifically, an strength overestimation with the MCC model. Moreover, the effect of the parameter n, which controls the shape of the yield surface, can be observed in Figure 3.4b. In this figure, it is also interesting to observe that the intersection between the CSL and the yield surface of CASM does not necessarily match at the maximum deviatoric stress, which enables CASM to reproduce a stress-strain behaviour where the deviatoric stress reaches a peak strength before approaching the critical state (Yu et al., 2005), as often observed in the laboratory for sand.

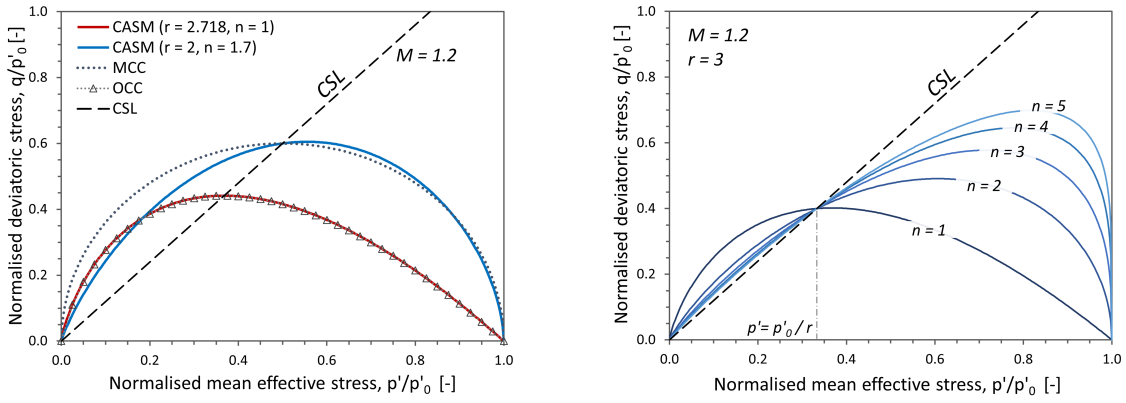

(a) CASM, OCC, and MCC yield surfaces comparison.

(b) CASM yield surfaces with different values of n.

Figure 3.4: Normalised yield surfaces.

It is important to note that in Yu (1998), since the constitutive model is only presented in the p' - q space, the slope of the CSL is assumed to be constant. However, in the alternative proposed in Arroyo and Gens (2021), this slope is expressed as a function of the Lode's angle, as detailed later.

• Plastic potential

The original formulation of the model (Yu, 1998) makes use of the well-known stress-dilatancy relationship of Rowe (1962) (Eq. 3.20). Note that this relationship was developed from minimum energy considerations of particle sliding and has been observed to provide satisfactory results for most practical problems (Yu, 1998).

$$\frac{\dot{\varepsilon}^p_{vol}}{\dot{\varepsilon}^p_q} = \frac{9(M-\eta)}{9+3M-2M\eta} \tag{3.20}$$

Where $\dot{\varepsilon}^p_{vol}$ is the plastic volumetric strain increment, and $\dot{\varepsilon}^p_q$ is the deviatoric strain increment. The plastic potential integrated from Rowe's stress dilatancy is given by (Yu, 1998):

$$g(p',q) = 3M \cdot \ln\left(\frac{p'}{C}\right) + (3+2M) \cdot \ln\left(\frac{2q}{p'}+3\right) - (3-M) \cdot \ln\left(3-\frac{q}{p'}\right) = 0 \tag{3.21}$$

Where the size parameter C can be determined using the current stress state *(p', q)*. It is important to note that, by using Eq. (3.21), the flow rule is non-associated since the plastic potential function does not coincide with the yield surface.

Yu (2006) pointed out that, although accurate for high stress ratios, the Rowe's stress-dilatancy relationship is not realistic for low stress ratios such as one-consolidation. With the aim of overcoming this limitation, Yu (2006) proposed an alternative plastic potential function that gives zero plastic volumetric strain increment at critical states and is integrated from the following stress-dilatancy equation:

$$\frac{\dot{\varepsilon}^p_{vol}}{\dot{\varepsilon}^p_q} = \frac{M^n - \eta^n}{m\eta^{n-1}} \tag{3.22}$$

Where m is a material parameter independent of n and r that controls the shape of the plastic potential function. This parameter can be estimated, ensuring that the stress conditions in one-dimensional consolidation are adequately reproduced by Eq. (3.22) (Alonso et al., 1990; McDowell & Hau, 2003; Ohmaki, 1982). Therefore, in 1D consolidation (where there are zero lateral strains) m leads to a stress path that matches K_0 estimated from Jaky (1944) equation. The stress-dilatancy relation (Eq. 3.22) can be integrated to give the following plastic potential function (Yu, 2006):

$$g(p',q) = m \cdot \ln\left[1+(m-1)\left(\frac{\eta}{M}\right)^n\right] + n(m-1)\ln\frac{p'}{C} \tag{3.23}$$

- **Hardening rule**

As in the Cam-clay models, an isotropic volumetric hardening rule is adopted such that the size of the yield surface is controlled by p'_0 evolving with plastic volumetric strains.

$$\frac{\partial p'_0}{\partial \varepsilon^p_{vol}} = \frac{v p'_0}{\lambda - \kappa} \tag{3.24}$$

Where ε^p_{vol} is the volumetric plastic strain and λ is the slope of the CSL and reference consolidation line in the $\ln p'$ - v space.

Modifications proposed by Arroyo and Gens (2021)

Having implemented CASM as a user-defined soil model (UDSM) into PLAXIS, Arroyo and Gens (2021) introduced some modifications to the formulation of CASM, which are described in this section.

As previously indicated, the original CASM formulation proposed by Yu (1998) was developed for triaxial conditions, assuming a constant value for M. Conversely, Arroyo and Gens (2021) define M as a function of the Lode's angle, θ, which defines the orientation of the stress state in the deviatoric plane. More specifically, M_θ is determined by using the following equation proposed by Sheng et al. (2000):

$$M_\theta = M_{tc} \left(\frac{2\alpha^4}{1 + \alpha^4 + (1 - \alpha^4) \sin 3\theta} \right)^{\frac{1}{4}} \tag{3.25}$$

Where M is the slope of the CSL in triaxial compression and α is a parameter that controls the shape of the function as well as the difference of M between triaxial compression (θ = - 30°) and extension (θ = 30°). Arroyo and Gens (2021) selected M and α to coincide with the Mohr-Coulomb envelope for triaxial compression and extension loading conditions. In such cases, these parameters are defined by equations (3.26) and (3.27).

$$M_{tc} = \frac{6 \cdot \sin \phi_{\text{cs}}}{3 - \sin \phi_{\text{cs}}} \tag{3.26}$$

$$\alpha = \frac{3 - \sin \phi_{\text{cs}}}{3 + \sin \phi_{\text{cs}}} \tag{3.27}$$

Where ϕ_{cs} is the friction angle at critical state for triaxial compression. The adopted function in the deviatoric plane is shown in Figure 3.5

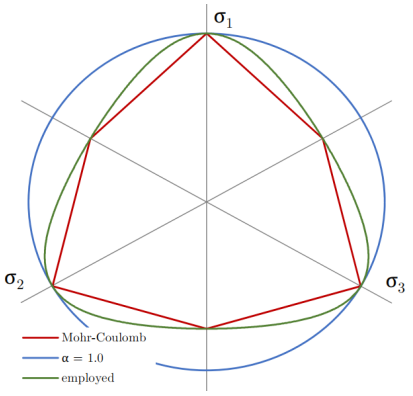

Figure 3.5: Shape of the yield function in the deviatoric plane (Arroyo & Gens, 2021).

The variation of the critical state friction angle, ϕ_c, for different values of the Lode's angle may be computed using equation (3.28) (Potts & Zdravkovic, 1999), which is derived from the Mohr-Coulomb failure criterion and uses Equation 3.25 as interpolation function, $g_{(\theta)}$. Figure 3.6 shows the variation of the critical state friction angle for different Lode's angles and for different fiction angles at the critical state for triaxial compression.

$$\phi_c = \sin^{-1} \left(\frac{2\sqrt{3} \cdot \sin(\phi_{cs}) \cdot g_{(\theta)} \cdot \cos(\theta)}{3 - \sin(\phi_{cs}) - 2 \cdot \sin(\phi_{cs}) \cdot g_{(\theta)} \cdot \sin(\theta)} \right) \tag{3.28}$$

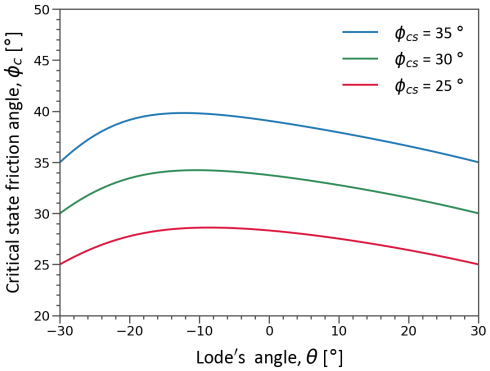

Figure 3.6: Critical state friction angle variation for different Lode's angles.

• Yield surface

Taking into account the Lode's angle dependency of M, the yield surface function is defined as:

$$f(p', q, p'_0) = \left(\frac{q}{M_\theta p'}\right)^n + \frac{1}{\ln r} \cdot \ln\left(\frac{p'}{p'_0}\right) = 0 \tag{3.29}$$

• Plastic potential

As an alternative to the previous function (Eq. 3.21), Arroyo and Gens (2021) used a new flow rule (Eq. 3.30) to derive a new plastic potential function defined as shown in equation (3.30).

$$D = \frac{\dot{\varepsilon}^p_{vol}}{\dot{\varepsilon}^p_q} = \left(\frac{M_\theta}{m} - M_\theta\right)\left(\frac{\eta}{M_\theta}\right) + \left(M_\theta - \frac{M_\theta}{m}\right)\left(\frac{\eta}{M_\theta}\right)^{1-m} \tag{3.30}$$

$$g(p', q) = \left(\frac{q}{p' M_\theta}\right)^m + m - \frac{p'_c(m-1)}{p'} - 1 \tag{3.31}$$

Where m is the parameter that controls the shape of the function and p'_c must be solved for the current stress state by using:

$$p'_c = \frac{p'}{m-1}\left[m + \left(\frac{q}{M_\theta p'}\right)^m - 1\right] \tag{3.32}$$

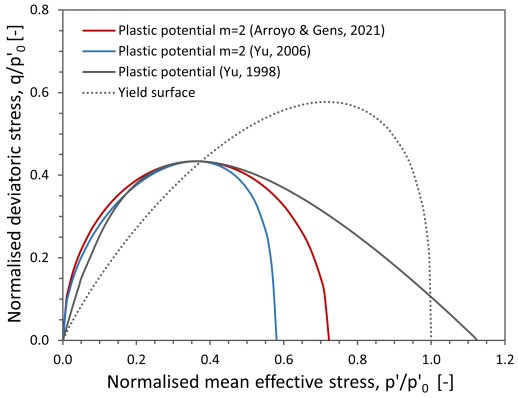

(a) Different plastic potential surfaces proposed in the literature.

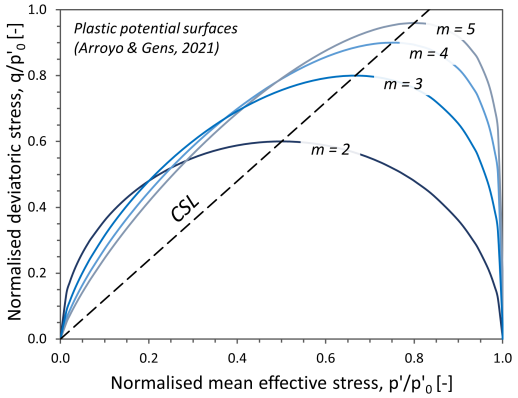

(b) Plastic potential surface proposed by Arroyo and Gens (2021) with different values of m.

Figure 3.7: Normalised plastic potential surfaces.

While having a similar shape as the yield function, Arroyo and Gens (2021) argue that the newly proposed equation has advantages over the previous ones (Yu, 1998, 2006) in terms of numerical implementation. Figure 3.7a compares the shapes of the different plastic potential surfaces proposed in

the literature (i.e. Arroyo and Gens (2021) and Yu (1998, 2006)) for a given effective stress state. It can be observed that the most noticeable differences are the shape of the plastic potential proposed by Yu (1998) with the others. Additionally, the effect of the parameter m on the shape of the plastic potential function proposed by Arroyo and Gens (2021) is shown in Figure 3.7b. A distortion of the plastic potential surface towards the right-hand side can be observed as the parameter m is increased.

• Viscoplastic extension

Although initially formulated as a rate-independent constitutive model, CASM was extended with a viscoplastic formulation by Arroyo and Gens (2021) to allow for the simulation of time-dependent and creep effects. The overstress theory of Perzyna (1966), which defines the total strain rate as shown in Eq. (3.33), was considered.

$$\dot{\varepsilon} = \dot{\varepsilon}^{e} + \dot{\varepsilon}^{vp} \tag{3.33}$$

Where $\dot{\varepsilon}^{e}$ and $\dot{\varepsilon}^{vp}$ are the elastic and viscoplastic strain rate tensors respectively. The viscoplastic strain rates are given by:

$$\dot{\varepsilon}^{vp} = \frac{\langle \Phi(f) \rangle}{\eta} \cdot \frac{\partial g}{\partial \sigma} \tag{3.34}$$

Where η is a viscosity parameter, Φ is the overstress function that depends on the rate-independent yield function f as follows:

$$\langle \Phi(f) \rangle = \begin{cases} \Phi(f) & \text{if } \Phi(f) \geq 0 \\ 0 & \text{if } \Phi(f) < 0 \end{cases} \tag{3.35}$$

A widely employed expression for the overstress function is shown in Eq. (3.36), where f_{o} is a reference normalisation stress and N is an exponent that should be equal or larger than 1 (Simo, 1989). Since the yield surface (Eq. 3.29) is already formulated in a dimensionless form, f_0 can be assumed to be equal to 1. However, the gradient of the plastic potential function ($\partial g / \partial \sigma$) is not dimensionless resulting in units of $\mathrm{m}^2 \cdot \mathrm{s} \cdot \mathrm{kN}^{-1}$ for η in SI.

$$\Phi(f) = \left(\frac{f}{f_o} \right)^{N} \tag{3.36}$$

State parameters

As implemented, CASM allows the definition of two state parameters of the possible five state parameters (i.e. Γ, e_{ini}, p'_0, R, and ψ_0). The state parameters which are not defined as input parameters can be derived from the others using the equations (3.37) (3.38), (3.40), and (3.41). Note that the combination of input state parameters which includes the initial state parameters, ψ_0, and the hardening parameter, p'_0 is not allowed since these parameters do not uniquely define e_{ini} and p'_0.

$$\Gamma = v_{ini} + \lambda \cdot \ln p'_{ini} - \psi_0 \tag{3.37}$$

$$e_{ini} = \Gamma - \lambda \cdot \ln p'_{ini} + \psi_0 - 1 \tag{3.38}$$

$$p'_x = \exp\left(\frac{\Gamma - v_{ini} - \kappa \cdot \ln p'_{ini}}{\lambda - \kappa} \right) \tag{3.39}$$

$$p'_0 = r p'_x \tag{3.40}$$

$$R = \frac{-p'_0 \cdot \exp\left[- \left(\frac{q_{ini}}{M_\theta p'_{ini}} \right)^{n} \ln r \right]}{p'_{ini}} \tag{3.41}$$

In the present study, an additional input parameter has been added to the model implementation into PLAXIS, i.e. the minimum void ratio, e_{min}. This modification improves the robustness of the model and ensures that unrealistic values of void ratios cannot be reached. When known, it is advised to specify a value for e_{min}, which is typically around 0.35 for very dense sands (Massarsch et al., 2015) and 0.4 for stiff clays (Das, 2008). If the value of e_{min} is not specified, it is assumed to be equal to 0.1 by default, which is the option chosen for all the simulations performed with CASM in the present study.

3.4.3. Summary of model equations

A summary of the CASM formulation implemented into PLAXIS is presented in the following table.

Table 3.1: Summary of the CASM formulation and its parameters.

Description	Constitutive equation	Model parameters
Elastic behaviour	$K = \frac{vp'}{\kappa}$ (3.16) $G = \frac{3(1-2\nu)}{2(1+\nu)}K$ (3.17)	κ: slope of the swelling line ν: Poisson's ratio
General stress-state relation	$\left(\frac{\eta}{M}\right)^n = 1 - \frac{\psi}{\psi_R}$ (3.13) $\psi_R = (\lambda - \kappa)\ln r$ (3.10)	n: stress - state coefficient λ: slope of the CSL r: spacing ratio
Yield Surface	$f = \left(\frac{q}{M_\theta p'}\right)^n + \frac{1}{\ln r}\cdot\ln\left(\frac{p'}{p'_0}\right) = 0$ (3.29) $M_\theta = M_{tc}\left(\frac{2\alpha^4}{1+\alpha^4+(1-\alpha^4)\sin 3\theta}\right)^{\frac{1}{4}}$ (3.25)	M_θ: slope of the CSL in the p'- q space that depends on the Lode's angle
Plastic potential (Arroyo & Gens, 2021)	$g = \left(\frac{q}{p' M_\theta}\right)^m + m - \frac{p'_c(m-1)}{p'} - 1$ (3.31) $p'_c = \frac{p'}{m-1}\left[m + \left(\frac{q}{M_\theta p'}\right)^m - 1\right]$ (3.32)	m: plastic potential shape controlling parameter
Hardening rule	$\frac{\partial p'_0}{\partial \varepsilon^p_{vol}} = \frac{vp'_0}{\lambda - \kappa}$ (3.24)	p'_0: hardening parameter
Viscoplasticity	$\dot{\varepsilon}^{vp} = \frac{\langle\Phi(f)\rangle}{\eta}\cdot\frac{\partial g}{\partial \sigma}$ (3.34) $\Phi(f) = \left(\frac{f}{f_o}\right)^N$ (3.36)	η: Viscosity parameter N: exponent of the viscosity formulation

3.4.4. CASM parameters

CASM implementation into PLAXIS consists of 22 input parameters, from which 10 are model parameters, 4 are material state parameters, and 8 are numerical control parameters already defined by default. Table 3.2 presents these parameters with typical values or the values defined by default (for the numerical control parameters) reported in Yu (2006) and Arroyo and Gens (2021).

Table 3.2: Meaning and typical range of values for CASM parameters.

Parameter	Description	Typical value or range
Elasticity		
κ	Slope of the swelling line.	$\kappa = 0.005$ (sand) $\kappa = 0.01$ - 0.06 (clay)
ν	Poissons's ratio.	$\nu = 0.15$ - 0.35 (clay and sand)
Critical state line		
λ	Slope of the CSL in the $\ln p'$ - v space.	$\lambda = 0.01$ - 0.05 (for sand at low-pressure level) $\lambda = 0.1$ - 0.2 (clay)
Γ	Intersection of the CSL with a ref. pressure of 1kPa.	$\Gamma = 1.8$ - 4 (clay and sand)
ϕ_{cs}	Critical state friction angle defined in the p' - q space.	$\phi_{cs} = 21^\circ$ - 26° (clay) $\phi_{cs} = 28^\circ$ - 35° (sand)
Plasticity		
n	Stress-state coefficient, which controls the shape of the yield surface.	$n \geq 1$ (allowable) $n = 1$ - 5 (recommended)
r	Spacing ratio, which defines the distance between the CSL and the RCL in the $\ln p'$ - v space.	$r > 1$ (allowable) $r = 1.5$ - 3 (clay)
m	Plastic potential parameter that controls the shape of the plastic potential function.	$m \geq 2$ to apply Eq. (3.31) $m =$ -1 to apply Eq. (3.21)
State parameters[†]		
e_{ini}	Void ratio at the start of the simulation.	$R \geq 1$ defined with negative sign (for internal calculation purposes)
p'_0 [*]	Hardening parameter.	
R [*]	Isotropic overconsolidation ratio.	
ψ_0	State parameter at the start of the simulation.	
Viscosity		
N	Parameters corresponding to the viscoplasticity extension of the model that should be defined if a rate-dependent response is expected.	$N \geq 2$ $N = 0$ and $\eta = 0$ for rate-independent analysis
η		
Numerical control parameters[⋆]		Values defined by default
Ctrl - p_{atm}	Reference normalisation pressure equal to the atmospheric pressure.	Ctrl - $p_{atm} = 100$ kPa
Ctrl - tol yield	Tolerance to consider the stress state on the yield surface.	Ctrl - tol yield = 1.0E-8
Ctrl - max NR iter	Maximum number of Newton-Raphson iterations before reducing the size of the step.	Ctrl - max NR iter = 30
Ctrl - n subinc	Number of sub-increments employed to calculate a higher-order solution.	Ctrl - n subinc = 2
Ctrl - tol error	Tolerate relative error in the sub-stepping algorithm.	Ctrl - tol error = 1.0E-3
Ctrl - min dt frac	Minimum fraction of the original step that is allowed by the sub-stepping algorithm.	Ctrl - min dt frac = 1.0E-6
Ctrl - n inc int	Parameter that controls the number of times that incorrect integration is allowed.	Ctrl - n inacc int (deactivated)
e_{min}	Minimum void ratio	$e_{min} = 0.1$

[†] Only two of these state parameters should be defined. This should be done by assigning values to the two selected parameters and null values to the remaining ones, which will be computed internally. For further details, refer to Arroyo and Gens (2021).

[*] In the PLAXIS implementation, these parameters are defined in the same parameter box with a negative sign to define R and a positive to define p'_0.

[⋆] Numerical control parameters with internally assigned default values and, therefore, can be set as zero in the material set window in PLAXIS. Further information can be found in Arroyo and Gens (2021).

3.5. NorSand model (Jefferies, 1993)

NorSand (NS) is an elastoplastic model developed from the fundamental axioms of critical state theory described by Jefferies (1993):

- *Axiom 1.* A unique locus exists inp', q, e space such that soil can be deformed without limit at constant stress and constant void ratio; this locus is called the critical state locus (CSL).
- *Axiom 2.* The CSL forms the ultimate condition of all distortional processes in soil so that all monotonic distortional stress state paths tend to this locus.

This model incorporates the state parameter concept and applies an incremental hardening rule that is defined by an image of the critical state on the yield surface, requiring that the image state moves towards the critical state with straining (Jefferies, 1993).

Jefferies et al. (2015) show that NS model is capable of capturing the features of a full range of soil behaviour from static liquefaction of very loose soils to dilation of very dense soils, overcoming the inability of standard CSSM models (such as Cam-clay, Modified Cam-clay and Granta-gravel) to reproduce realistic dilation and yielding of dense sand and overconsolidated clay. Contrary to the standard CSSM models assumption, which considers that all yield surfaces intersect the critical state, NorSand employs the original premise of Drucker et al. (1957) regarding the association between yield surfaces and void ratio, and further recognising that soils exist in a spectrum of states (Jefferies & Been, 2006). NS considers infinite normal compression lines (NCL) in the p' - e plane that depend on the initial void ratio and may cross the CSL. Figure 3.8a illustrates the standard idealised view of a single NCL that is parallel to the CSL, while Figure 3.8b illustrates different and infinite number of NCL that are not necessarily parallel to the CSL. Note that, in both cases, the CSL is a unique line, as pointed out in Axiom 1 and can be defined by the semi-logarithmic form (Eq. 3.42) in the (lnp', e) space.

$$e_c = \Gamma - \lambda \cdot \ln p' \tag{3.42}$$

Where Γ and λ are both intrinsic soil properties that can be estimated through laboratory tests. Note that in NorSand, Γ is defined in terms of void ratio, while in CASM (Eq. 3.2), this parameter is defined in terms of specific volume.

For some soils, the semi-logarithmic trend for the CSL is not a good representation and a power-law alternative is used as in Jefferies et al. (2015). This power-law CSL defined by equation (3.43) is a function of C_a, C_b, and C_c, which are material constants.

$$e_c = C_a - C_b \left(\frac{p'}{p'_{ref}} \right)^{C_c} \tag{3.43}$$

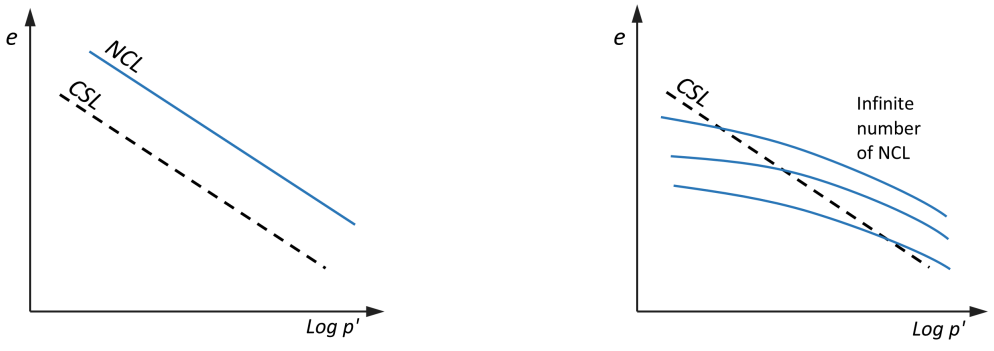

(a) Single NCL parallel to CSL.

(b) Infinite number of NCLs crossing CSL.

Figure 3.8: Comparison of different assumptions for the NCL (Adapted from Jefferies and Been (2006)).

3.5.1. NorSand formulation

NorSand is a plasticity model for soil that, as other similar models, comprises an elastic component, a yield surface, a flow rule, and a hardening law. The formulation of the NorSand model implemented into PLAXIS is described in this subsection.

• Elastic behaviour

Even though there is wide evidence that soils tend to be anisotropic, isotropic elasticity is adopted for this model by employing the following relations:

$$G = G_{ref} \left(\frac{p'}{p'_{ref}} \right)^{n_G} \tag{3.44}$$

$$K = 2G \frac{1+\nu}{3-6\nu} \tag{3.45}$$

Where G is the shear modulus, G_{ref} is the reference value of the shear modulus at the reference pressure (p'_{ref}), K is the elastic bulk modulus, and ν is the Poisson's ratio.

• Yield surface

NorSand adopts a Cam-clay like stress-dilatancy relationship (Eq 3.46), which differs from Cam-clay in using the stress ratio at the image condition ((M_i), also termed as zero-dilatancy friction ratio, rather than a stress ratio at the critical state (M). The stress ratio at image condition (M_i) tends to critical state with shear strain.

$$D^p = M_i - \eta \tag{3.46}$$

As indicated by Brinkgreve et al. (2022), two options are offered for the zero-dilatancy friction ratio based on the suggestion of Li and Dafalias (2000), which indicates that M_i depends on the state parameter (ψ) as shown in the next equations. For dense soil, since this material follows Nova's flow rule, NorSand always uses Eq. (3.47).

$$\psi < 0 \Rightarrow M_i = M \left(1 + \frac{N \chi_i \psi_i}{M_{tc}} \right) \tag{3.47}$$

For loose soils, two options are available in the implementation: equation (3.48), for loose soils that follow the Taylor-Bishop framework of a constant dissipation rate regardless of how loose a material is, while equation (3.49) for loose soils that show less ability to dissipate plastic work as they get progressively looser (extended Dafalias).

Option A: Taylor - Bishop

$$\psi \geq 0 \Rightarrow M_i = M_\theta \tag{3.48}$$

Option B: Extended Dafalias

$$\psi \geq 0 \Rightarrow M_i = M_\theta \left(1 - \frac{N \chi_i \psi_i}{M_{tc}} \right) \tag{3.49}$$

If the state parameter, ψ is equal to zero, NorSand yield surface intersects the CSL and $M_i = M$. The proposed options (i.e. Option A and B) can be chosen by the user based on laboratory test data (Brinkgreve et al., 2022). Option A can be defined by introducing the model parameter M_{tc} with a negative sign, while Option B is established by defining M_{tc} with a positive sign.

In equations (3.47), (3.48), and (3.49), M_θ is the critical state friction ratio depending on the Lode's angle defined by Eq. (3.50), N is the volumetric coupling parameter (from Nova's flow rule), χ_{i} is the state-dilatancy parameter defined by Eq. (3.51), M_{tc} is the critical friction angle for triaxial compression (i.e. $M_\theta = M_{tc}$ *at* $\theta = \pi/6$), and ψ_{i} is the state parameter at the image conditions that can be defined by equation (3.52).

$$M_\theta = M_{tc} - \frac{M_{tc}^2}{3 + M_{tc}} \cos\left(\frac{3\theta}{2} + \frac{\pi}{4} \right) \tag{3.50}$$

$$\chi_i = \frac{\chi_{tc}}{1 - \chi_{tc}\lambda/M_{tc}} \tag{3.51}$$

$$\psi_i = e - e_c(p'_i) \tag{3.52}$$

The determination of the NorSand yield surface follows the same steps as Cam-clay as in Jefferies and Been (2006). Eq. (3.46) is substituted into Eq (3.53), which results from the normality condition and is true regardless of the soil's internal dissipation mechanism, as long as work hardening or perfectly plastic condition prevail (Jefferies & Been, 2006).

$$\frac{\dot{p'}}{p'} + \frac{\dot{\eta}}{D^p + \eta} = 0 \tag{3.53}$$

The integration of the normality condition (Eq. 3.53) together with the stress dilatancy rule leads to the NorSand yield surface (Eq. 3.54) (Jefferies & Been, 2006).

$$f(q, p', p'_i) = q - M_i \left[1 + \ln\left(\frac{p'_i}{p'}\right)\right] p' \tag{3.54}$$

Where p'_i is the mean effective stress at the image state, which defines the size of the yield surface, in a similar fashion to the role of p'_c in Cam-clay. Figure 3.9 shows the NorSand yield surfaces normalised by the mean effective stress at the image state, p'_i, for both loose and dense sand. In this figure, it can be further observed that an internal cap taken as a flat surface that crosses the outer yield surface is used to limit the maximum stress ratio, η_L.

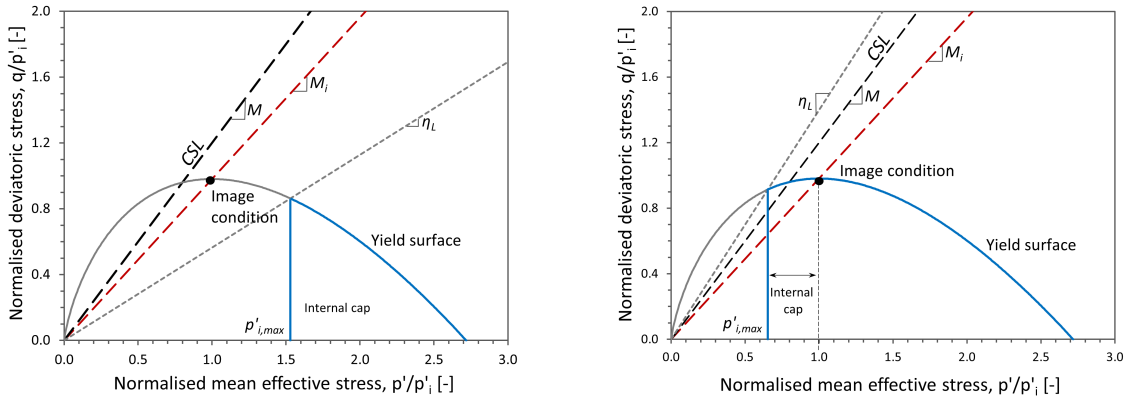

(a) Loose sand **(b)** Dense sand

Figure 3.9: Normalised NorSand yield surfaces and limiting stress ratios.

• Flow rule

NorSand uses the simple postulate that plastic work is only dissipated in distortion resulting in one form of stress-dilatancy which is the fundamental flow rule adopted. This is largely the same as Original Cam-clay (Schofield & Wroth, 1968), with the difference that NorSand allows the dissipation parameter (the zero-dilatancy 'frictional dissipation' stress ratio M_i) to vary with soil state under control of the soil property N rather than being just a function of the stress ratio M_{tc} which corresponds to critical state friction (Brinkgreve et al., 2022). This flow rule is expressed as a function of the plastic strain increments ratio by:

$$\frac{\dot{\varepsilon}^p_3}{\dot{\varepsilon}^p_1} = z_{3,tc} - (z_{3,tc} - z_{3,te}) \cos\left(\frac{3\theta}{2} + \frac{\pi}{4}\right) \begin{cases} z_{3,tc} = \dfrac{2D^p_{tc} - 3}{2D^p_{tc} + 6}; & D^p_{tc} = D^p \left(\dfrac{M_{i,tc}}{M_i}\right) \\ z_{3,te} = \dfrac{2D^p_{te} + 6}{2D^p_{te} - 3}; & D^p_{te} = D^p \left(\dfrac{M_{i,te}}{M_i}\right) \end{cases} \tag{3.55}$$

$$\frac{\dot{\varepsilon}_2^p}{\dot{\varepsilon}_1^p} = \frac{aD^p - 1 + \dfrac{d\varepsilon_3}{d\varepsilon_1}(cD^p - 1)}{1 - bD^p} \begin{cases} a(\theta) = \dfrac{\sin(\theta) + \sqrt{3}\cos(\theta)}{3} \\ b(\theta) = \dfrac{-2\sin(\theta)}{3} \\ c(\theta) = \dfrac{\sin(\theta) - \sqrt{3}\cos(\theta)}{3} \end{cases} \tag{3.56}$$

• Hardening rule

Similar to the parameter p'_c in the Cam-clay model, the parameter p'_i is the hardening parameter in the NorSand model. The hardening rule complies with the second axiom and is formulated as (Jefferies & Been, 2006):

$$\dot{p'_i} = \left[H \frac{p'}{p'_i} \frac{M_i}{M_{i,tc}} (p'_{i,max} - p'_i) - S_{soft} \right] \dot{\varepsilon}_q^p \tag{3.57}$$

$$H = H_0 - H_\psi \cdot \psi \tag{3.58}$$

Where H is the plastic hardening modulus, which is necessary since the NorSand yield surface is decoupled from the CSL and the parameter λ can no longer serve as plastic compliance (Jefferies & Been, 2015). The parameter H is a function of the state parameter, ψ, (Eq. 3.58) and the model parameters, H_0 and H_ψ, are dimensionless. The parameter $p'_{i,max}$ is the maximum mean effective pressure at the image state for a current stress state, which limits hardening and is defined by:

$$p'_{i,max} = p' \exp\left(-\frac{\chi_{tc}\psi}{M_{i,tc}} \right) \tag{3.59}$$

The original formulation of the NorSand hardening rule (Jefferies, 1993) did not include the softening parameter, S_{soft}, which was later considered in Jefferies et al. (2015), as well as an optional parameter in the model implementation in PLAXIS. This parameter was included in the formulation to avoid infringing the basic principle of the hardening limit ($p'_{i,max} > p'_i$) since contrary to drained loading, during undrained loading, the rate of change of p' can easily become faster than the basic hardening law leading to $p'_i > p'_{i,max}$. Therefore, the parameter S_{soft} is included in the hardening law to decrease the image stress under undrained conditions and is defined by:

$$S_{soft} = S\omega \left(\frac{\eta}{M_i} \right) \left(\frac{K}{p'} \right) D^p p'_i \tag{3.60}$$

$$\omega = 1 - \lambda \frac{\chi_{tc}}{M_{tc}} \tag{3.61}$$

Where S is the softening flag that can be defined equal to 0 for drained conditions and equal to 1 for undrained conditions. Figure 3.10 compares the results of an undrained triaxial compression test simulation with different values of the softening parameter. It can be observed that when the softening flag is activated (i.e. $S = 1$) reaches the critical state with a rate more rapid (i.e. at early strains) and presents a lower peak deviatoric stress than the response when the softening parameter is equal to 1.

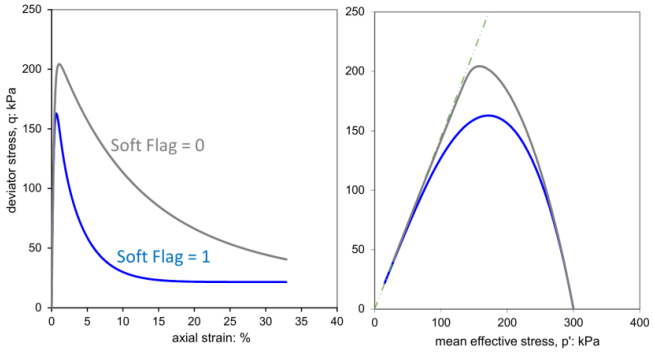

Figure 3.10: Mechanical behaviour during an undrained triaxial compression test using the softening parameter (Brinkgreve et al., 2022).

3.5.2. Summary of model equations

A summary of the NorSand formulation implemented into PLAXIS is presented in Table 3.3.

Table 3.3: Summary of the NorSand formulation and its parameters.

Description	Constitutive equation	Model parameters
Elastic behaviour	$G = G_{ref}\left(\frac{p'}{p'_{ref}}\right)^{n_G}$ (3.44) $K = 2G\frac{1+\nu}{3-6\nu}$ (3.45)	G_{ref}: reference shear modulus at the reference pressure n_G: exponent of the power-law elasticity p'_{ref}: reference mean pressure ν: Poisson's ratio
Critcal state	$e_c = \Gamma - \lambda \ln p'$ (3.42) $e_c = C_a - C_b\left(\frac{p'}{p'_{ref}}\right)^{C_c}$ (3.43)	Γ: intersection of the CSL with the p'-axis in the ($\ln p'$, e) space for a reference pressure of 1kPa λ: slope of the CSL in ($\ln p'$, e) space C_a: void ratio corresponding to a mean pressure equal to 0 kPa C_b: parameter of the power-law expression C_c: exponent of the power-law
Yield surface	$f = q - M_i\left[1 + \ln\left(\frac{p'_i}{p'}\right)\right]p'$ (3.54) $\psi < 0 \Rightarrow M_i = M\left(1 + \frac{N\chi_i\psi_i}{M_{tc}}\right)$ (3.47) $\psi \geq 0 \Rightarrow M_i = M_\theta$ (3.48) $\psi \geq 0 \Rightarrow M_i = M_\theta\left(1 - \frac{N\chi_i\psi_i}{M_{tc}}\right)$ (3.49) $\chi_i = \frac{\chi_{tc}}{(1 - \chi_{tc}\lambda/M_{tc})}$ (3.51) $\psi_i = e - e_c(p'_i)$ (3.52)	N: volumetric coupling parameter χ_{tc}: soil property that governs the slope of the minimum dilatancy as a function of the state parameter M_{tc}: friction ratio at critical state in triaxial compression
Flow rule	$\frac{\dot{\varepsilon}_3^p}{\dot{\varepsilon}_1^p} = z_{3,tc} - (z_{3,tc} - z_{3,te})\cos\left(\frac{3\theta}{2} + \frac{\pi}{4}\right)$ (3.55) $\frac{\dot{\varepsilon}_2^p}{\dot{\varepsilon}_1^p} = \frac{aD^p - 1 + \frac{d\varepsilon_3}{d\varepsilon_1}(cD^p - 1)}{1 - bD^p}$ (3.56)	
Hardening rule	$\dot{p'_i} = \left[H\frac{p'}{p'_i}\frac{M_i}{M_{i,tc}}(p'_{i,max} - p'_i) - S_{soft}\right]\dot{\varepsilon}_q^p$ (3.57) $p'_{i,max} = p'\exp\left(-\frac{\chi_{tc}\psi}{M_{i,tc}}\right)$ (3.59) $H = H_0 - H_\psi \cdot \psi$ (3.58) $S_{soft} = S\omega\left(\frac{\eta}{M_i}\right)\left(\frac{K}{p'}\right)D^p p'_i$ (3.60)	H_0, H_ψ : hardening rule model parameters S : softening flag

3.5.3. NorSand model parameters

The NorSand implementation into PLAXIS requires a total of 14 or 15 parameters depending on the option used for the critical state line (i.e. semi-log CSL or power-law CSL). Most of these model parameters are well-known in soil mechanics and are easily estimated from laboratory or in-situ tests. Table 3.4 presents these parameters and typical range of values for sand, as proposed in Jefferies and Been (2015) and Jefferies et al. (2015).

Table 3.4: Meaning and typical range of values for NorSand parameters.

Parameter	Description	Typical value or range
Elasticity		
G_{ref}	Reference shear modulus at reference pressure	–
p'_{ref}	Reference mean pressure	100 kPa
n_G	Exponent of the power-law elasticity	–
ν	Poissons's ratio	0.1 - 0.3
Critical state line		
Γ [A]	Intersection of the CSL with a pressure of 1kPa	0.9 - 1.4
λ [A]	Slope of the CSL	0.01 - 0.07
C_a [B]	Void ratio corresponding to $p' = 0$	–
C_b [B]	Parameter of the power-law expression	–
C_c [B]	Exponent of the power-law	–
Plasticity		
M_{tc}	Critical friction ratio in triaxial compression	1.2 - 1.5
N	Volumetric coupling parameter	0.2 - 0.5
χ_{tc}	State-dilatancy parameter	2.5 - 4.5
H_0	Hardening rule model parameter	–
H_ψ	Hardening rule model parameter	–
S	Softening flag	0 / 1
State parameters		
R	Isotropic overconsolidation ratio	$\geq$1
ψ_0	Initial state parameter	–

[A] Parameters for the semi-log form of the critical state line.
[B] Parameters for the power-law form of the critical state line.

4

Verification and sensitivity analysis of the constitutive models

4.1. Introduction

The application of computational mechanics through finite element analysis in geotechnical engineering problems requires the implementation of an appropriate constitutive soil (or rock) model into the finite element software. After the implementation, the model must be verified to ensure that they are able to reproduce accurately the concepts assumed during the model development and its solution. Additionally, the successful application of a constitutive model in design practice requires the users to have a good understanding of the concepts and assumptions behind the development of the model. In fact, the behaviour of real soils is far more complex than any constitutive model can describe, as soil models are a simplification of reality (Kavvadas & Amorosi, 1998).

The constitutive models CASM and NorSand, described in detail in the previous chapter, have recently been implemented as user-defined soil models (UDSMs) in the finite element analysis software PLAXIS (Bentley Systems, Inc., 2023). Even though verification exercises have already been carried out by the PLAXIS team and their collaborators, complementary verification exercises are undertaken in the present study. More specifically, simulations of element laboratory tests are performed, and the obtained results are compared against those reported in the literature corresponding to the analytical solution of the models or results of already verified implementations. In addition, sensitivity analyses are performed to evaluate the influence of the model parameters on the obtained response.

4.2. CASM verification

CASM has been implemented as a user-defined soil model in PLAXIS by the academic group of the Polytechnic University of Catalonia. An implicit Backward Euler method with automatic sub-stepping has been used. Details about the numerical implementation can be found in Arroyo and Gens (2021). In this section, the verification of this UDSM is performed by simulating element laboratory tests, specifically monotonic triaxial compression tests and direct simple shear tests. Both PLAXIS SoilTest (a tool to quickly perform laboratory tests on the basis of a single-point algorithm) and PLAXIS 2D have been used. Subsequently, the results have been compared with those published in Yu (1998) and Arroyo and Gens (2021).

4.2.1. Monotonic triaxial compression tests

In Yu (1998), several monotonic triaxial compression test simulations with CASM are reported, which can be used for verification purposes. A drained triaxial compression test on a sample of Erksak 330/0.7 sand isotropically consolidated under a mean effective stress of $p'_{ini} = 60$ kPa was selected to be simulated with PLAXIS SoilTest using the parameters reported in Yu (1998) (Table 4.1). To use Rowe's plastic potential formulation, as in Yu (1998), the parameter m has been set equal to -1. Note that the model is initialised based on Γ and e_{ini}.

Table 4.1: Parameters used in the CASM verification for a drained monotonic triaxial compression test.

Parameter	λ	κ	ν	ϕ_{cs} [°]	n	r	m	Γ	e_{ini}	p'_0/R	ψ_0
Value	0.0135	0.005	0.3	30	4	6792	-1	1.8167	0.677	Not used	Not used

The results of the simulation (solid blue line) show a perfect overlap with the ones reported by Yu (1998) (dashed red line), both in terms of stress ratio and volumetric strain evolution with deviatoric strains (Figure 4.1).

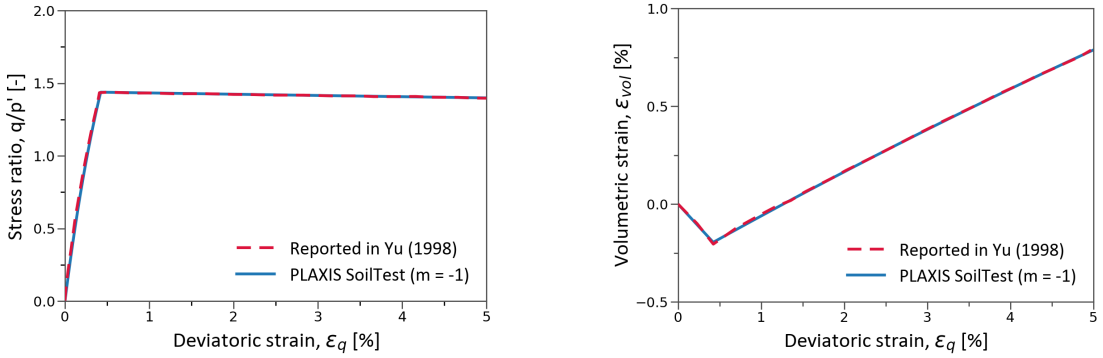

(a) Stress ratio evolution with deviatoric strain.

(b) Volumetric strains evolution with deviatoric strain.

Figure 4.1: Verification of a drained monotonic triaxial compression test on Erksak 330/0.7 sand.

Complementary, undrained triaxial compression tests were also simulated for verification purposes. Specifically, a monotonic undrained triaxial test simulation on a loose sample of Ottawa sand has been performed with the implementation of CASM into PLAXIS. The input parameters used for the simulation are those reported in Yu (1998) (Table 4.2) with an initial effective cell pressure, σ'_x, of 350 kPa. The simulation results were compared against those found in the literature, obtaining an excellent agreement in terms of effective stress path and stress-strain response, including the strain-softening behaviour. This verification comparison can be observed in Figure 4.2.

Table 4.2: Parameters used in the CASM verification for a drained monotonic triaxial compression test.

Parameter	λ	κ	ν	ϕ_{cs} [°]	n	r	m	Γ	e_{ini}	p'_0 [kPa]$/R$	ψ_0
Value	0.0168	0.005	0.3	29.77	3	25.93	-1	1.864	Not used	350	Not used

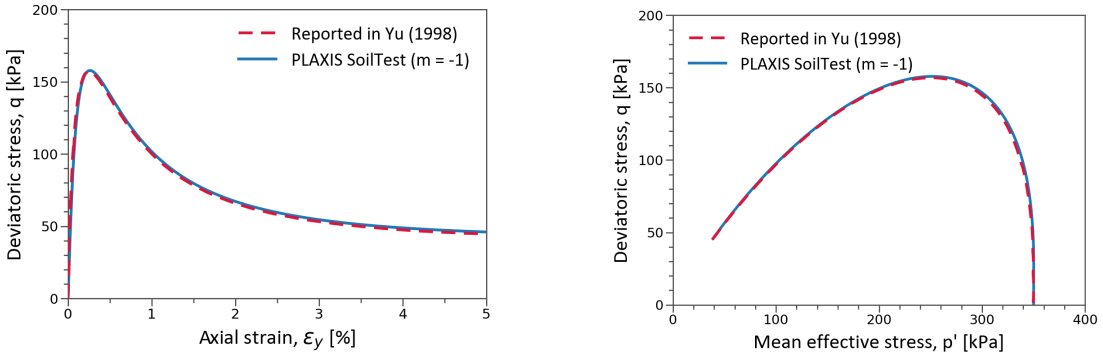

(a) Stress-strain response.

(b) Effective stress path.

Figure 4.2: Verification of an undrained monotonic triaxial compression test on Ottawa sand.

In Arroyo and Gens (2021), CASM was used to simulate anisotropically consolidated undrained triaxial compression tests performed at different strain rates on tailing materials called 'brown, red, and black evolved tailings'. In the present study, these tests were simulated with the SoilTest facility,

with the results being compared with those presented in Arroyo and Gens (2021).

The parameters of the model employed for each one of the different materials are presented in Table 4.3. Moreover, the initial test conditions, as reported in Annex F of Arroyo and Gens (2021), are displayed in Table 4.4. Note that in these cases, the model is initialised based on Γ and R.

Table 4.3: Model parameters used in the CASM verification for the undrained monotonic triaxial compression test.

Tailings material	λ	κ	ν	ϕ_{cs} [°]	n	r	m	Γ	p'_0/R	N	η [m^2 s kN^{-1}]
Brown	0.05	0.019	0.3	34.25	4.9	12.3	2.486	2.05	-1.05	5	4E-10
Red	0.056	0.019	0.3	35.73	3.25	5.18	2.367	2.14	-1.05	5	1E-09
Black	0.046	0.019	0.3	33.08	5.1	75	2.465	2.353	-1.05	5	1E-11

Table 4.4: Initial conditions of the undrained monotonic triaxial compression tests simulated for verification purposes.

Tailings material	Test	K_0 [-]	p'_{ini} [kPa]	Disp. rate [mm/min]
Brown	Bruma_R_S2_SP_CKU_C_3	0.5	408	0.02
Red	Bruma_R_S1_SP_CKU_F_6	0.5	504	0.2
Black	Bruma_R_S1_SP_CKU_G_7	0.5	100	0.002

Figure 4.3 shows the results of the simulation corresponding to the brown tailing material. It can be observed that the obtained results do not match perfectly those reported in Arroyo and Gens (2021). Some discrepancies can be particularly observed in terms of the effective stress path. An additional simulation considering a slightly higher initial mean effective stress (p'_{ini} = 420 kPa, rather than 408 kPa) was carried out. Although still not reaching a perfect match, the results obtained in the latter simulation (grey lines) show an improved match in terms of peak deviatoric stress. Given the fact that, as shown later, the results obtained in the other two simulations match very well those reported in Arroyo and Gens (2021), it is believed that the slight discrepancies observed for this simulation might be simply related to some inaccuracy in the reported initial conditions.

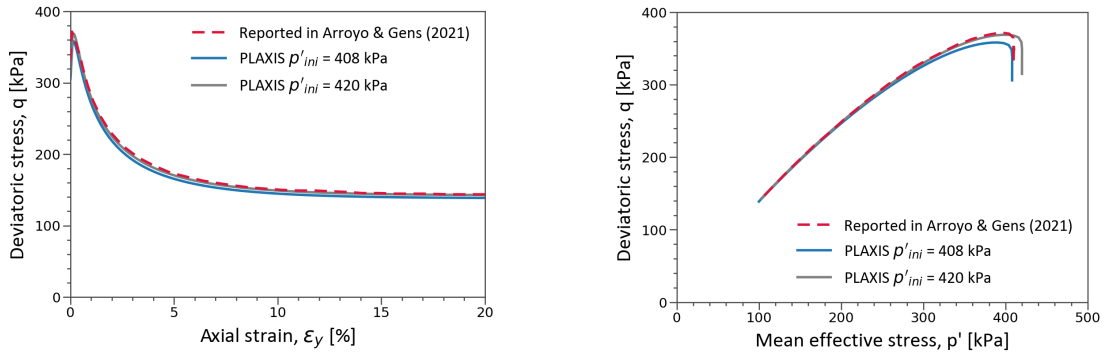

(a) Stress-strain response.

(b) Effective stress path.

Figure 4.3: Verification of undrained monotonic triaxial compression test for brown tailing material.

The tests on the red and black tailing materials have been simulated using both PLAXIS SoilTest and PLAXIS 2D. In the second case, the soil sample is modelled as an axisymmetric square of 1 unit length and with the boundary conditions shown in Figure 4.4. The results of both simulations perfectly overlap with those reported in Arroyo and Gens (2021) (Figure 4.5 and Figure 4.6).

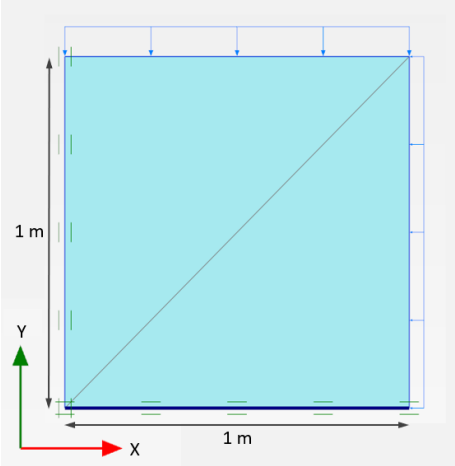

Figure 4.4: Boundary conditions defined for the PLAXIS 2D axisymmetric model simulation.

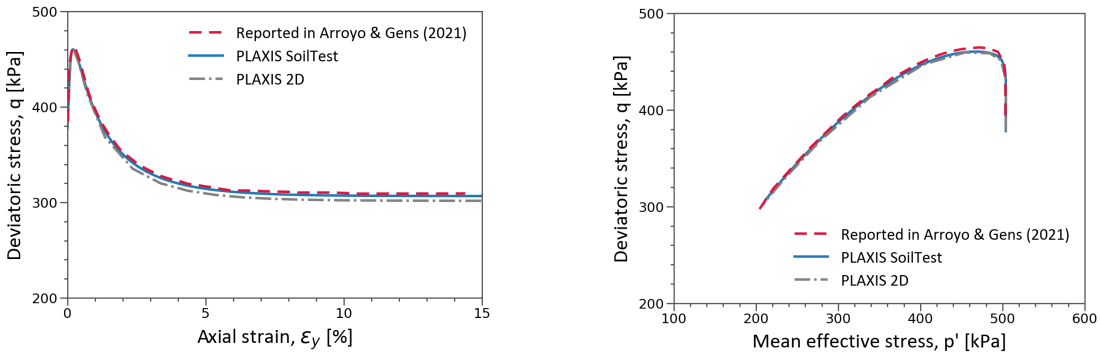

(a) Stress-strain response. **(b)** Effective stress path.

Figure 4.5: Verification of undrained monotonic triaxial compression test for red tailing material.

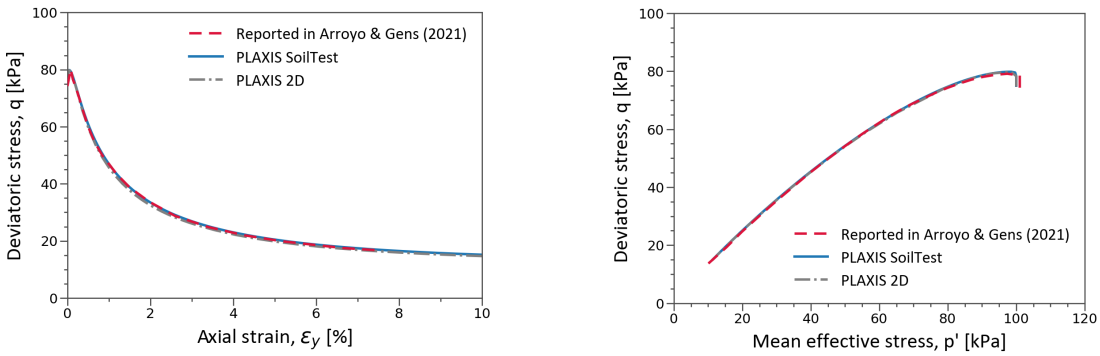

(a) Stress-strain response. **(b)** Effective stress path.

Figure 4.6: Verification of undrained monotonic triaxial compression test for black tailing material.

In addition, since the current udsm incorporates the effects of viscoplasticity, a new series of simulations were performed to investigate the effect of the displacement rate on the response. In this case, the results obtained in three different simulations of undrained monotonic triaxial compression tests performed with different displacement rates on black tailings are compared against those measured in the laboratory, as shown in Figure 4.7. It can be observed that the stress paths and the maximum deviatoric stresses are reasonably captured in the simulations. However, the strength reduction is not accurately captured, and the stiffness during the strain softening is overestimated by the simulations.

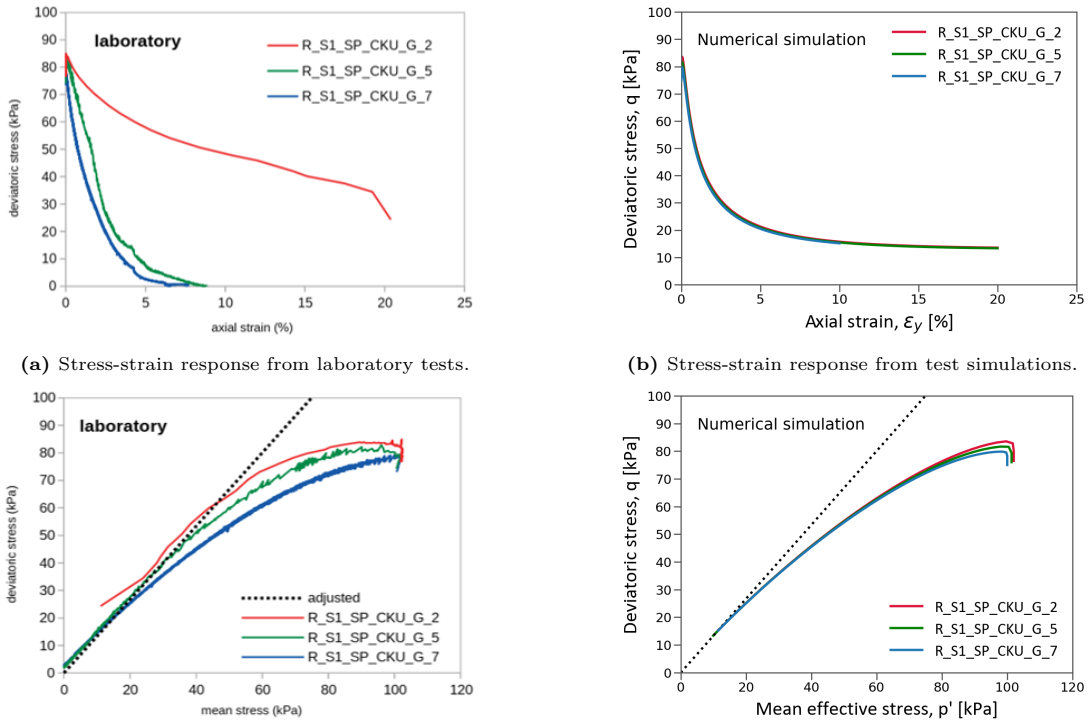

(a) Stress-strain response from laboratory tests.

(b) Stress-strain response from test simulations.

(c) Effective stress paths from laboratory tests.

(d) Effective stress paths from test simulations.

Figure 4.7: Undrained monotonic triaxial compression tests results from Arroyo and Gens (2021) and test simulations of black tailing material with different strain rates.

4.2.2. Direct simple shear tests

In this section, the simulation of direct simple shear tests are compared against the results reported in Yang and Yu (2006). The model parameters and initial test conditions are presented in Table 4.6, and correspond to loose and dense Erksak sand samples. Note that the model is initialised based on Γ and the over-consolidation ratio R. In particular, R has been set equal to -1 since it is reported in Yang and Yu (2006) that the initial stress state is on the yield surface.

Table 4.5: Parameters used in the CASM verification for the direct simple shear tests.

Erksak	λ	κ	ν	ϕ_{cs} [°]	n	r	m	Γ	p'_0/R	K_0	$\sigma'_{y,0}$ [kPa]
Loose	0.0135	0.005	0.3	30	4	6792	-1	1.8167	-1	0.6	191
Dense	0.0135	0.005	0.3	30	4	6792	-1	1.8167	-1	4	130

Figure 4.8 compares results of the DSS test simulations performed with PLAXIS SoilTest against those results reported in Yang and Yu (2006) obtained by using a user-defined model in the finite element software ABAQUS. For the loose Erksak sand simulation, a good agreement is observed, while for the dense Erksak sand simulation, some discrepancies can be observed. It is believed that these discrepancies might arise from differences in the input data (or their internal process within the user-defined models) used in the simulations carried out in the present study and those performed by Yang and Yu (2006). In effect, the values of the model parameters indicated in Table 4.5 - which were established according to what is reported in Yang and Yu (2006) - seem to result apparently in values of void ratio and state parameter different from those also reported. Specifically, the initial void ratio, e_{ini}, (not used as an input parameter) is reported in Yang and Yu (2006) to be equal to 0.59, while the value internally computed is equal to 0.67 according to (Eq. 3.38). Moreover, when the e_{ini} reported is used as an input parameter, the resulting R is higher than 1, contradicting the assumption of the initial stress state on the yield surface, also reflected in the results (Figure 4.8b). On the contrary, for loose Erksak sand, these discrepancies do not exist since the specified initial void ratio and the initial value of the hardening parameter in Yang and Yu (2006) ($e_{ini} = 0.82$ and $p'_0 = 204$kPa) are practically

equal to the ones internally computed ($e_{ini} = 0.822$ and $p'_0 = 204.13$kPa), which is reflected in the good match between the results shown in Figure 4.8a.

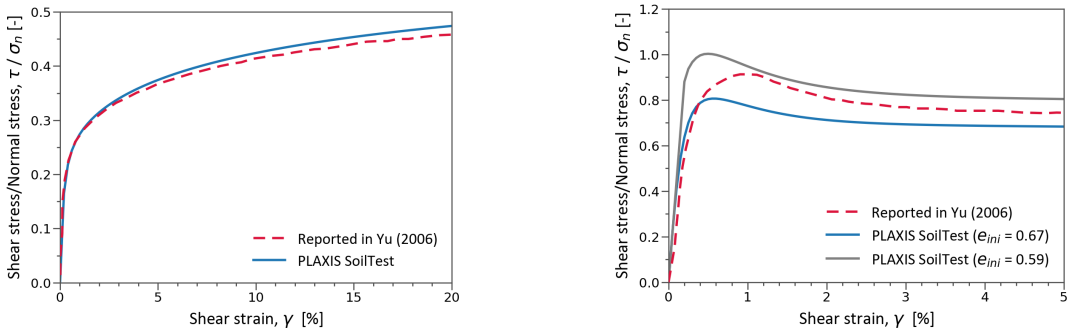

(a) Loose Erksak sand. **(b)** Dense Erksak sand.

Figure 4.8: Direct simple shear test simulations for the Erksak sand.

4.2.3. Verification exercises in boundary value problems

In addition to the verification exercises performed at the material point level with the simulation of laboratory tests, CASM implementation has been verified in the case of two simple boundary value problems: a rigid footing and an embankment. Both cases were analysed using MCC and CASM. In fact, CASM is formulated in such a way that the standard Cam-clay models can be recovered by simply choosing certain values of the material parameters. Specifically, in this case, the yield surface defined with $r = 2$ and $n = 1.7$, results in a very similar shape as the yield surface of MCC on the 'wet' side. Additionally, by setting the parameter $m = 2$, the plastic potential surface of CASM has the same elliptic shape as the one adopted in the MCC model (Arroyo & Gens, 2021). The same initial soil state conditions have been assumed, corresponding to slightly overconsolidated and normally consolidated materials (i.e. 'wet' side of critical state).

Rigid footing

The first boundary value problem analysis consists of the simulation of a circular rigid footing on a 4 meters deep clay deposit, overlying a rigid bedrock which is not explicitly modelled. Instead, its effect is described via a mechanically fixed boundary at the bottom of the model. The unsaturated and saturated unit weight of the clay layer are equal to 18 kN/m^3 and 20 kN/m^3, respectively. An axisymmetric analysis under drained conditions was carried out by applying a uniform line displacement to simulate the settlement of the footing rather than modelling the footing itself. The boundary conditions applied to the model and the dimensions are shown in Figure 4.9. Moreover, the parameters used for both models, CASM and MCC, are presented in Table 4.6. Note that MCC requires the value of the critical stress ratio as an input parameter, which can be determined based on the friction angle given as input to CASM, according to equation 3.26.

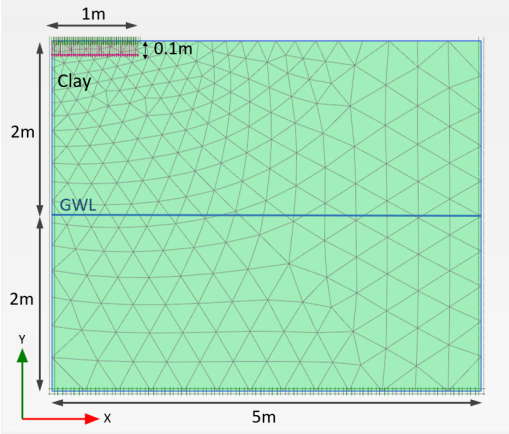

Figure 4.9: Boundary conditions and geometry of the rigid footing model.

Table 4.6: MCC and CASM parameters used for the clay layer in the rigid footing model.

Model	λ	κ	ν	ϕ_{cs} [°]	M	n	r	m	e_{ini}	R	OCR
MCC	0.16	0.03	0.2	–	0.9	–	–	–	1.84	–	1.2
CASM	0.16	0.03	0.2	23	–	1.7	2	2	1.84	-1.2	–

The results of the simulations with MCC and CASM in terms of total displacements and mean effective stresses are shown in Figure 4.10 and Figure 4.11, respectively. It can be observed very similar displacements and distribution of the mean effective stresses. Moreover, note that two vertical axes were defined (A-A* and B-B*) in the axis of symmetry and at the edge of the footing to show the results along them. These results are shown in Figure 4.12, where the mean effective stresses (Figure 4.12a) and the total displacements (Figure 4.12b) are plotted showing practically the same results obtained using both models.

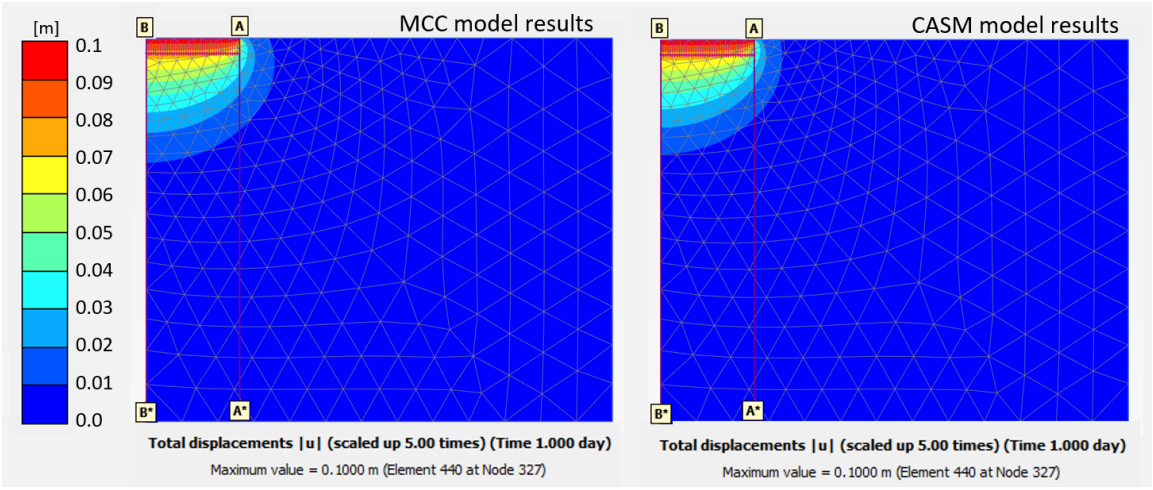

Figure 4.10: Total displacements at the end of the analysis.

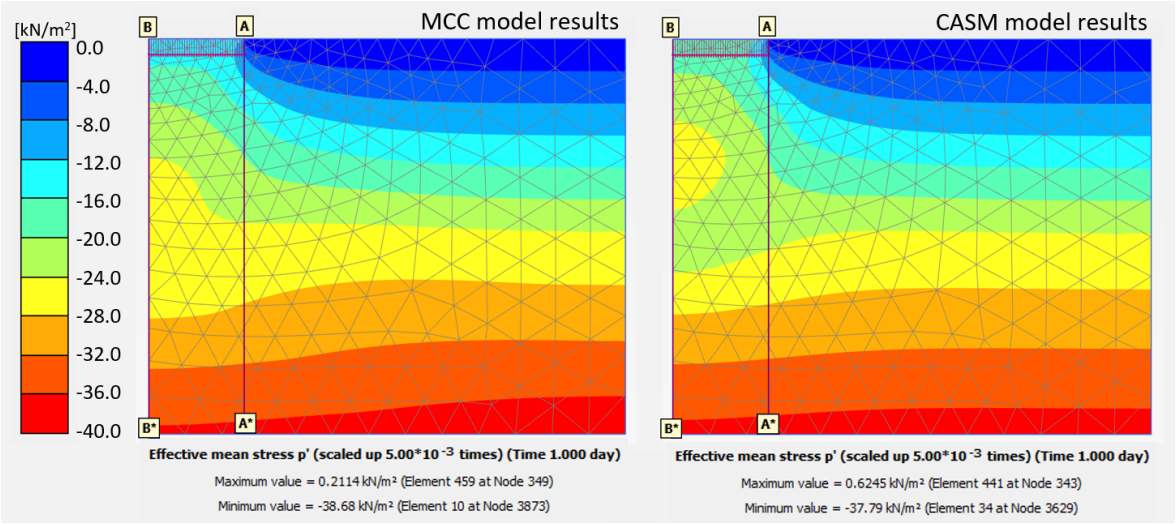

Figure 4.11: Mean effective stresses at the phase when the uniform line displacement of 0.1 meters is applied.

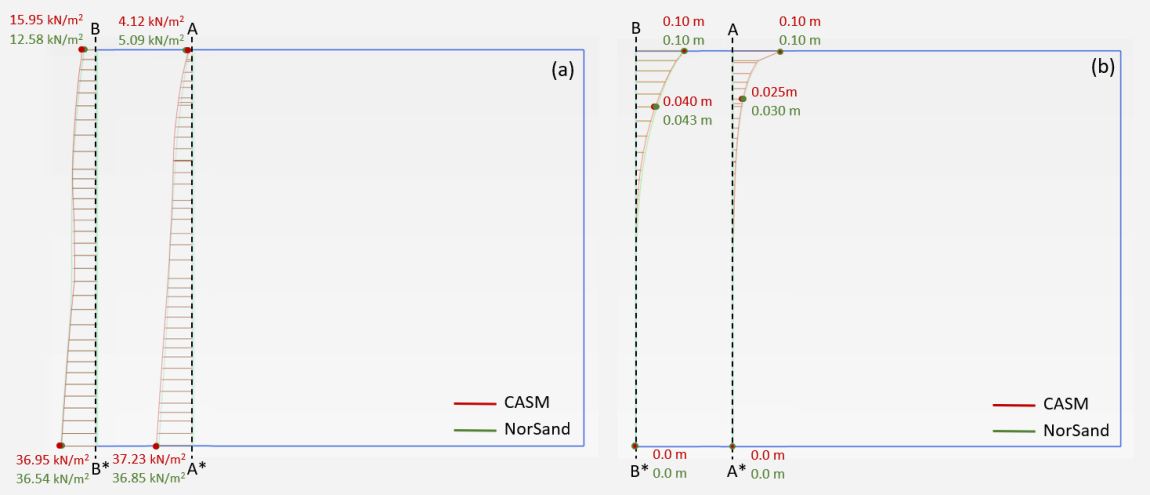

Figure 4.12: (a) Mean effective stresses and (b) total displacements results along the axis A-A* and B-B*.

Figure 4.13 shows the location of two nodes at different levels and three stress points at the foundation level, which were pre-selected to plot their results as shown in Figure 4.14 and Figure 4.15. The results extracted from the stress points are the volumetric strain evolution and the stress paths, which match very well with small differences that may be due to the slightly different shapes of the yield surfaces used in the models. The results extracted from the nodes are the vertical displacement evolution with vertical force applied during the simulations. These results show similar trends and magnitudes of displacements for the simulations using both models (i.e. MCC and CASM).

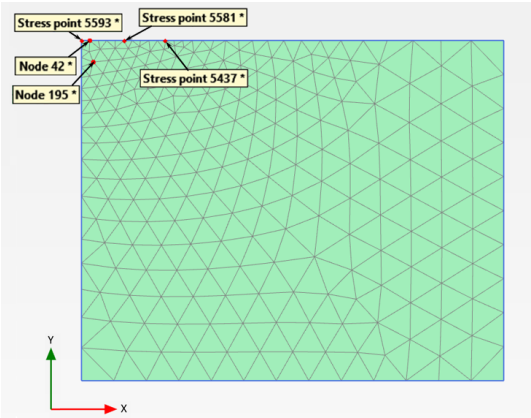

Figure 4.13: Pre-selected nodes and stress points.

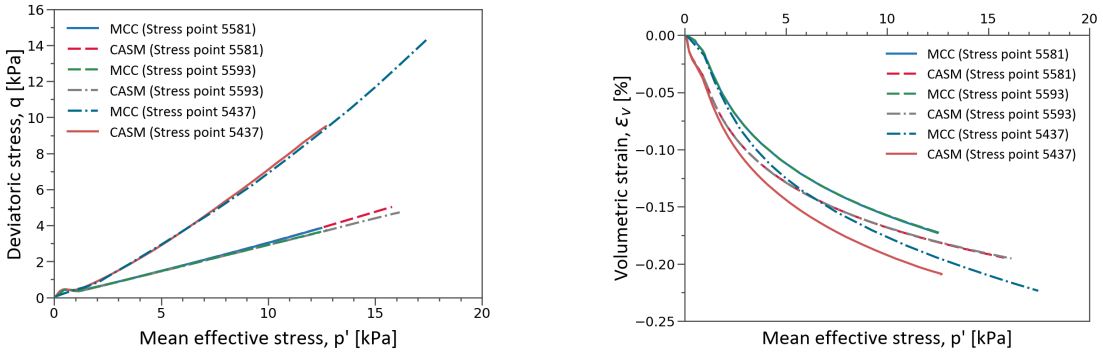

(a) Effective stress paths.

(b) Volumetric strain evolution with mean effective stress.

Figure 4.14: Results obtained from the pre-selected stress points for the rigid footing models.

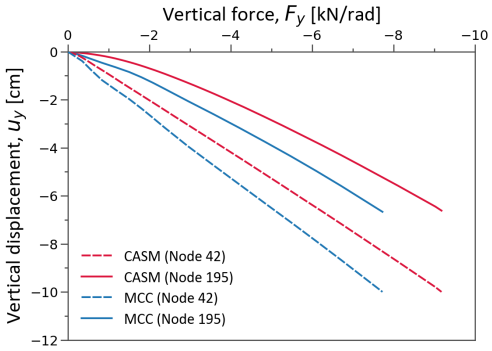

Figure 4.15: Vertical displacement evolution with vertical force for the pre-selected nodes.

Embankment

As a second boundary value problem verification exercise, the construction of an embankment over a soft clay deposit has been analysed as a plane strain model. The boundary conditions and geometry of the model are depicted in Figure 4.16. Five staged construction phases have been added to simulate the progressive construction of the embankment layers, of 1 meter each, until reaching a total height of 5 meters. The embankment is constructed on a 10-meter deep layer of soft clay. The embankment fill was modelled using the Mohr-Coulomb model with the parameters and properties given in Table 4.7, and the layer of soft clay was modelled with MCC and CASM with the parameters presented in Table 4.8 considering a saturated unit weight of 17 kN/m^3, an unsaturated unit weight of 16 kN/m^3. Note that the CASM parameters used to initialise the model are the initial void ratio, e_{ini}, and the over-consolidation ratio, R, in order to define the same initial soil state conditions as for MCC.

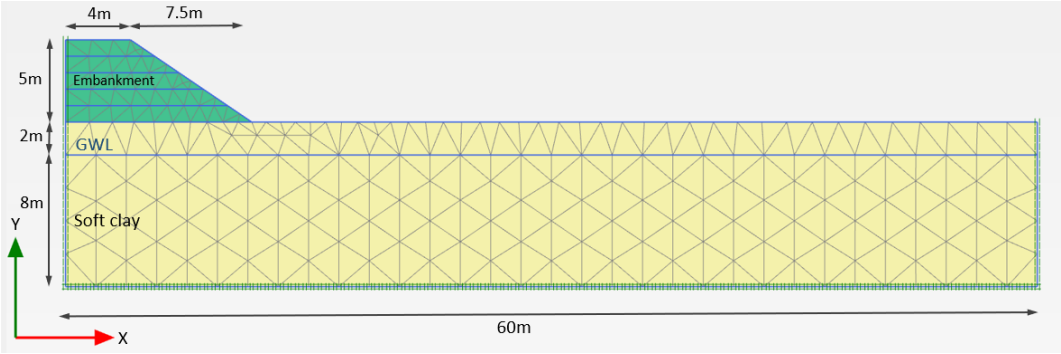

Figure 4.16: Boundary conditions and geometry of the embankment model.

Two types of analysis have been considered: a consolidation analysis, where each layer is built in 10 days, and an undrained analysis. In the first case, an isotropic permeability equal to 8.64E-3 m/day has been assumed.

Table 4.7: Properties used to model the embankment fill.

Property	Value
Unsaturated unit weight, γ_{unsat}	19 kN/m^3
Saturated unit weight, γ_{sat}	20 kN/m^3
Young's modulus, E_{ref}	20 MN/m^2
Poisson's ratio, ν	0.20
Cohesion, c'	0 kN/m^2
Friction angle, ϕ'	40°
Dilatancy angle, ψ	0°

Table 4.8: MCC and CASM parameters used for the soft clay layer in the embankment models.

Model	λ	κ	ν	ϕ_{cs} [°]	M	n	r	m	e_{ini}	R	OCR
MCC	0.22	0.022	0.2	–	1.287	–	–	–	1.5	–	1
CASM	0.22	0.022	0.2	32	–	1.7	2	2	1.5	-1	–

As expected, the results of the consolidation analyses with both models are very similar. Figure 4.17 shows the total displacements at the end of the embankment construction of the analyses with MCC and CASM. The heat maps show that the total displacements in the embankment and in the clay layer have similar magnitudes, with the maximum total displacements being located in the same node with a slight difference of about 1 centimetre. Likewise, the results of the excess pore pressures at the end of the construction of the embankment are presented in Figure 4.18. The evolution of excess pore pressures in the soft clay layer for the analyses with both models show the same response with a slightly smaller minimum value obtained with CASM.

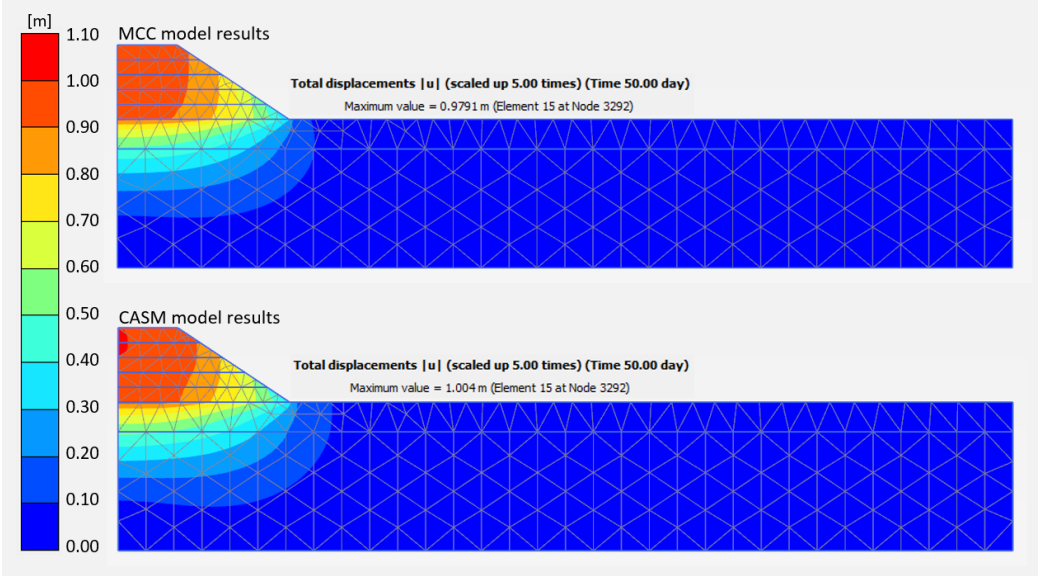

Figure 4.17: Total displacements at the last phase of the embankment construction simulation.

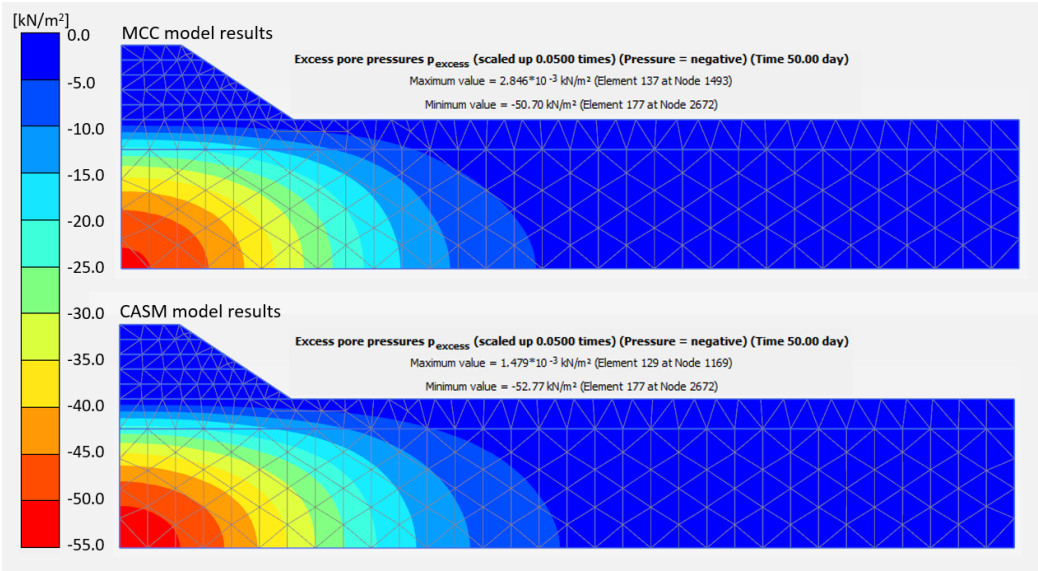

Figure 4.18: Excess pore pressures at the last phase of the embankment construction simulation.

In addition to the results indicated before, the evolution of the vertical displacements and excess pore pressure computed for both models at certain nodes were compared. These nodes were selected at different height levels as shown in Figure 4.19a, and their corresponding vertical displacements and excess pore pressure were plotted as a function of time (Figure 4.19b and Figure 4.19c). The results of both models show the same trends with slight differences.

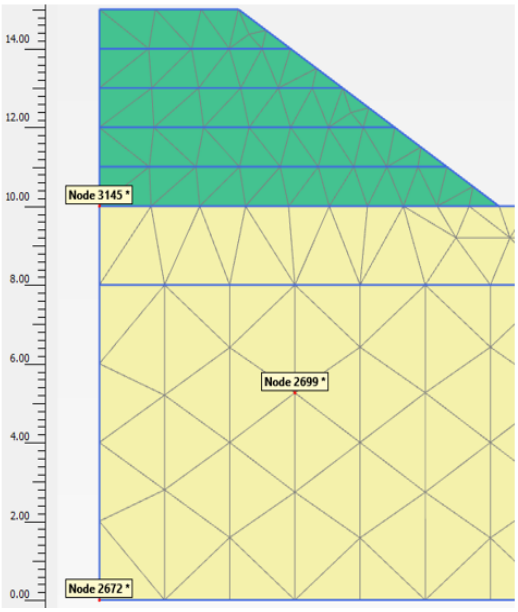

(a) Selected nodes at different levels.

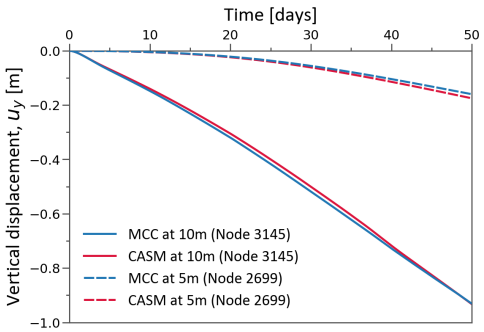

(b) Vertical displacement evolution.

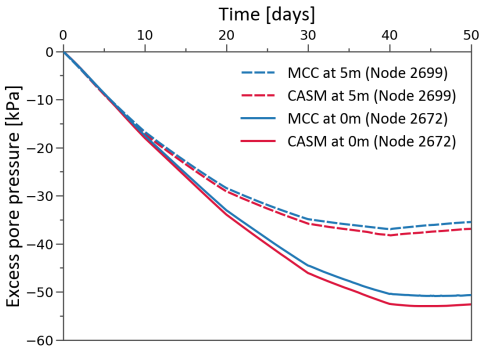

(c) Excess pore pressure evolution.

Figure 4.19: Results from the consolidation analysis at different nodes.

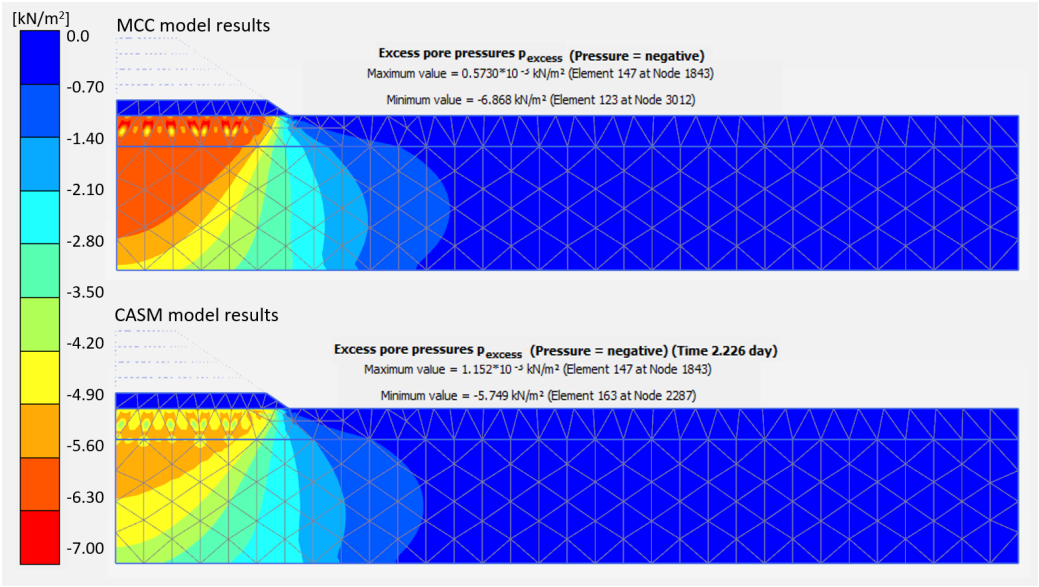

Figure 4.20: Excess pore pressures at the failure phase of the embankment construction simulation under undrained conditions.

For the analysis under undrained conditions, the simulations with both MCC and CASM models failed in the same construction phase. The excess pore pressures at this phase are shown in Figure 4.20, where a similar response and evolution of stresses can be observed with the larger excess pore pressures accumulated beneath the embankment. Note that the difference between the excess pore pressure of both models is around 1 kPa.

4.3. CASM sensitivity analysis

When compared with the Cam-clay models, CASM requires the definition of three additional parameters: r, n, and m. These parameters define important aspects of the model (namely, the distance between the Reference Consolidation Line and the CSL, as well as the shapes of the yield surface and plastic potential surface). Therefore, it is essential to get insight into their effect on the modelled response. With this objective, a series of monotonic triaxial compression tests were simulated using a reference set of parameters and changing the value of one of the target parameters. In addition, the effect of the viscosity parameters (i.e. η and N) is investigated in this section.

To perform the sensitivity analysis, the set of parameters corresponding to the 'red tailing' material found in Arroyo and Gens (2021) has been established as a reference, as well as the test conditions. These model parameters are presented in Table 4.9 and are used in the simulations of drained and undrained monotonic triaxial compression tests on anisotropically consolidated (K_0 = 0.5) looser (R = -1.05) and denser (R = -10) than the CS samples. These samples are subjected to an initial mean effective stress, p'_{ini} = 504 kPa, and sheared under a displacement rate of 0.2 mm/min. Moreover, the range of variation of the parameters was defined considering typical values reported by Yu (2006) (Table 3.2), increasing slightly the limits to observe more clearly the effect of the parameters in the model response.

Table 4.9: Reference CASM parameters for the sensitivity analysis.

Parameter	λ	κ	ν	ϕ_{cs} [°]	n	r	m	Γ	R	N	η [m^2 s kN^{-1}]
Value	0.056	0.019	0.3	35.73	3.25	5.18	2.367	2.14	-1.05/-10	5	1E-09

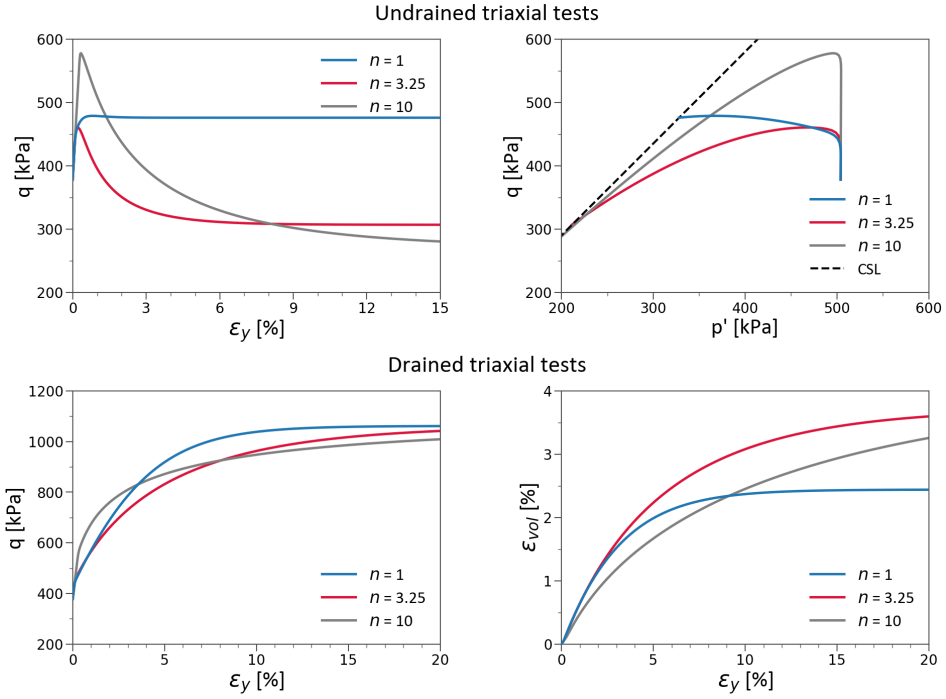

Figure 4.21: Sensitivity analysis results of parameter n.

The results of the sensitivity analysis for the stress-state coefficient, n, for loose samples are shown in Figure 4.21. It is observed that this parameter has a strong effect on the undrained peak deviatoric stress, which is expected since n controls the shape of the yield surface. Specifically, the greater the value of the parameter n, the greater the distortion of the yield surface towards the right-hand side ('wet' side). This distortion increases the elastic domain for initially looser than critical state samples and decreases the elastic domain for initially denser than critical state samples. Consequently, the stress path reaches the yield surface at larger effective stresses, with greater strain softening being subsequently required to reach the critical state. Figure 4.22 compares the stress paths evolution for the simulations with $n = 3.25$ and $n = 10$ until the moment that the yield surface is first reached in these simulations. Note that in Figure 4.21 the effective stress path corresponding to $n = 1$ is very different from the remaining ones since $n = 1$ results in a yield surface with the same shape as the one of the original Cam-clay, which does not allow the simulation of strain softening (Figure 4.22).

Under drained conditions, for larger values of n, it is observed an initially stiffer stress-strain response. In addition, less volumetric strains develop for the same axial strain. The latter does not apply for the case where $n = 1$ due to the different shape of the yield surface. The results of the sensitivity study for denser than the critical state samples show opposite responses since the corresponding stress paths start on the 'dry' side. For smaller values of n, larger undrained deviatoric stresses are obtained, and larger peak deviatoric stresses under drained conditions, as well as larger dilative volumetric strains. These results can be seen in Figure A.1 in Appendix A.

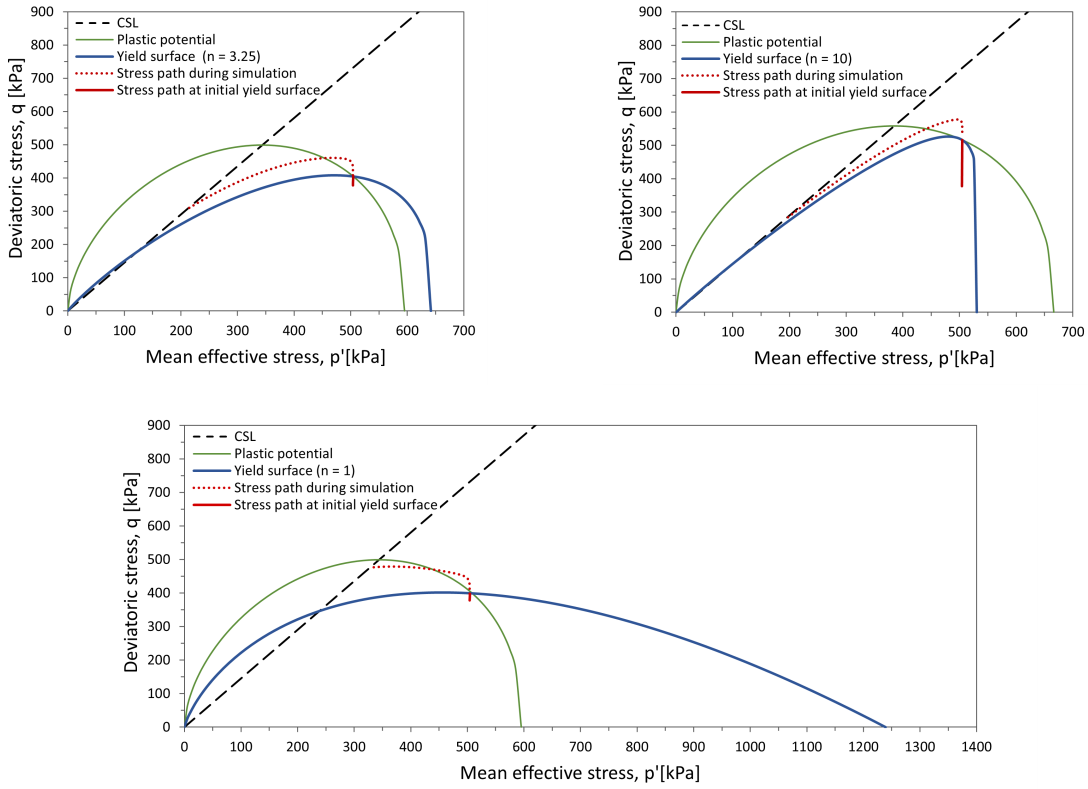

Figure 4.22: Moment at which the yield surfaces are reached for the undrained monotonic triaxial compression test simulation with $n = 3.25$, $n = 10$, and $n = 1$ (yield surface and plastic potential surface for the starting stress state).

Figure 4.23 shows the results when the spacing ratio, r, is changed for initially looser than the CS samples. It can be observed that larger values of r imply lower undrained peak deviatoric stresses and the critical state is reached at different effective stress states. Under drained conditions, a similar response is obtained in terms of deviatoric stress with softer stress-strain responses for larger values of r and larger volumetric strains.

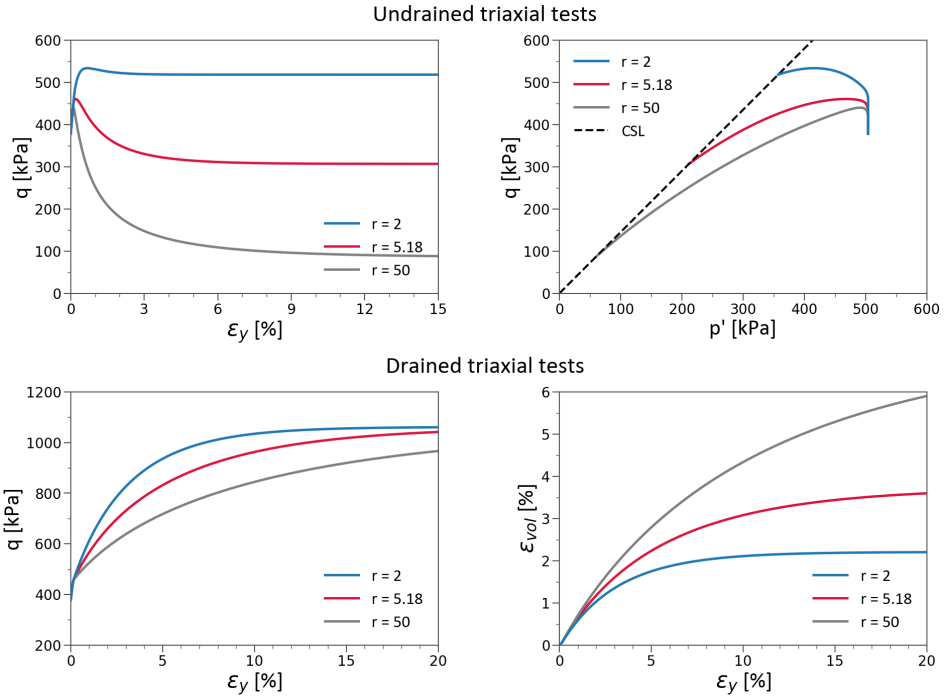

Figure 4.23: Sensitivity analysis results of parameter r.

The observed effect of the parameter r is explained since this parameter controls the size of the yield surface as illustrated in Figure 4.24, where the yield surfaces and stress paths are plotted at the moment in which the yield surfaces are firstly reached for the undrained simulations with $r = 5.18$ and $r = 50$. A larger value of r results in a larger yield surface, i.e. a larger elastic domain. In the ($\ln p'$, v) space, r defines the distance between the critical state line (CSL) and the reference consolidation line (RCL). Specifically, larger values of r imply a longer distance between the CSL and RCL, as shown in Figure 4.25. It is also observed that when r is larger, the mean effective stress at the critical state is lower. Therefore, higher excess pore pressures are built up. Note that this combination of input parameters (where R is used) results in simulations that do not start at the same initial state. The results for simulations on dense samples, which show similar responses as those for loose sands, are in Appendix A.

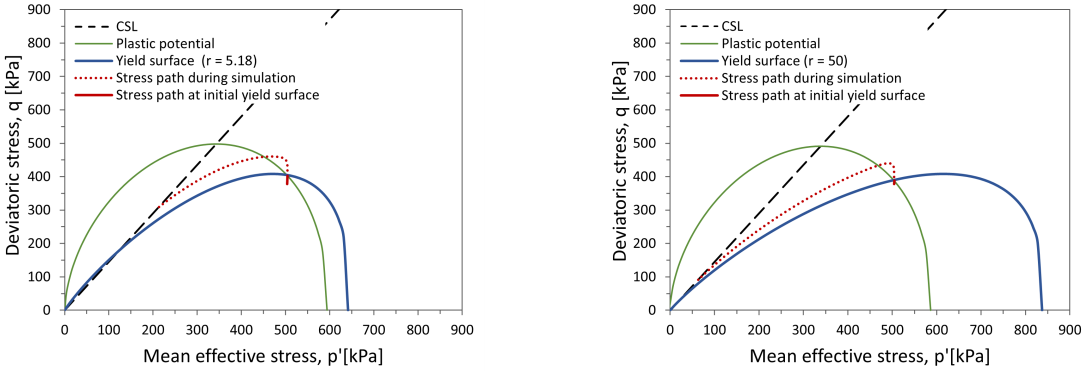

Figure 4.24: Moment at which the yield surfaces are reached for the undrained monotonic triaxial compression test simulation with $r = 5.18$ and $r = 50$ (yield surface and plastic potential surface for the starting stress state).

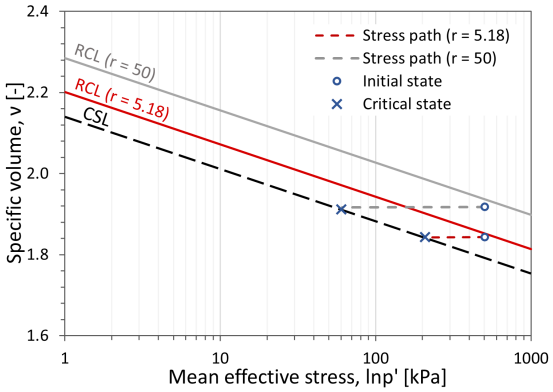

Figure 4.25: RCLs in the lnp' - v space for $r = 5.18$ and $r = 50$.

The results of the sensitivity analysis when m is changed under undrained and drained conditions for the looser than the CS sample are presented in Figure 4.26. Since the parameter m controls the shape of the plastic potential, the variation of this parameter does not affect the effective stress state at which the yield surface is first reached. Therefore, no effects are expected in terms of peak deviatoric strength. Nevertheless, from the moment that the yield surface is reached onward, the shape of the plastic potential influences the direction of the plastic strain increment through the flow rule affecting the hardening/softening evolution as observed in the results. More specifically, the larger the value of m, the stiffer the strain hardening/softening response, and the critical state is reached at smaller axial strains.

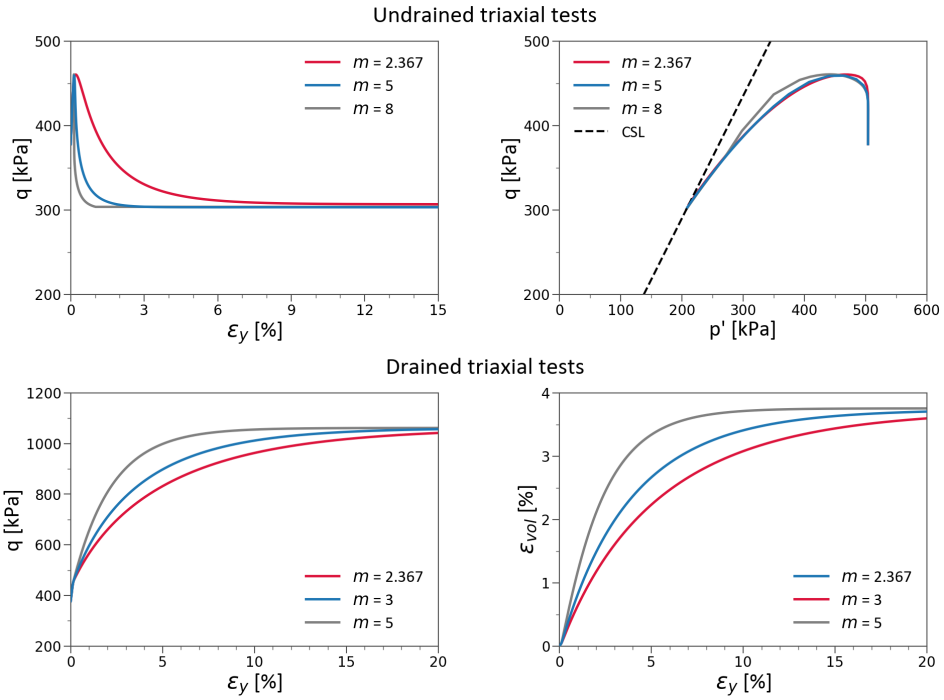

Figure 4.26: Sensitivity analysis results of parameter m.

Figure 4.27 compares the shape of the plastic potential surfaces at the moment in which the yield surface is first reached for the simulation in undrained conditions when $m = 2.367$ and $m = 5$. It can be observed a distortion on the plastic potential surface towards the right-hand side for the larger m. Naturally, this distortion affects the direction of the incremental strain vector, as indicated schematically in the figure. At the moment that the yield surface is reached, it is observed that the greater the value of m, the more horizontal the direction of the incremental plastic strains, meaning that the greater the

tendency to generate plastic volumetric strains for a given plastic deviatoric strain increment. Similar effects can be observed in the results for the dense sample where higher values of m imply a stiffer stress-strain response with a higher rate of volumetric strain evolution with axial strain, as well as a higher rate of strain softening as observed in Figure A.3 in Appendix A.

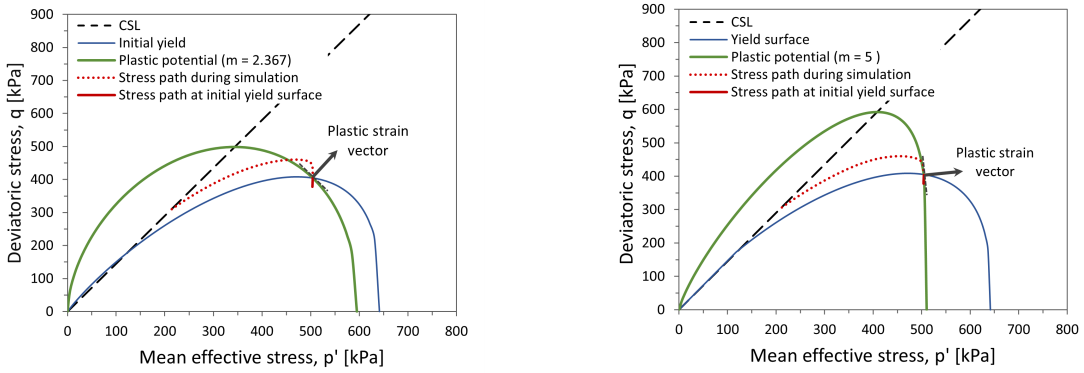

Figure 4.27: Moment at which the yield surfaces are reached for the undrained monotonic triaxial compression test simulation with $m = 2.367$ and $m = 5$ (yield surface and plastic potential surface for the starting stress state).

Regarding the viscosity parameters, three different simulations were performed using $N = 5$ and varying η between 1E-12 and 1E-06. While η = 1E-09 has been used for the sensitivity study on N, assuming an identical loading rate. Figure 4.28 and Figure 4.29 show the corresponding results for simulations on initially looser than the CS samples, where it can be observed that when the parameter η is increased, larger undrained peak and residual deviatoric stresses are obtained, as well as stiffer stress-strain response and smaller volumetric strains under drained conditions. Very similar effects can be observed when changing the value of the parameter N, with larger values of N implying larger deviatoric stresses under both drained and undrained conditions and lower volumetric strains under drained conditions. The results of the sensitivity study for the viscosity parameters corresponding to dense samples show the same response as for the loose samples and can be found in Appendix A.

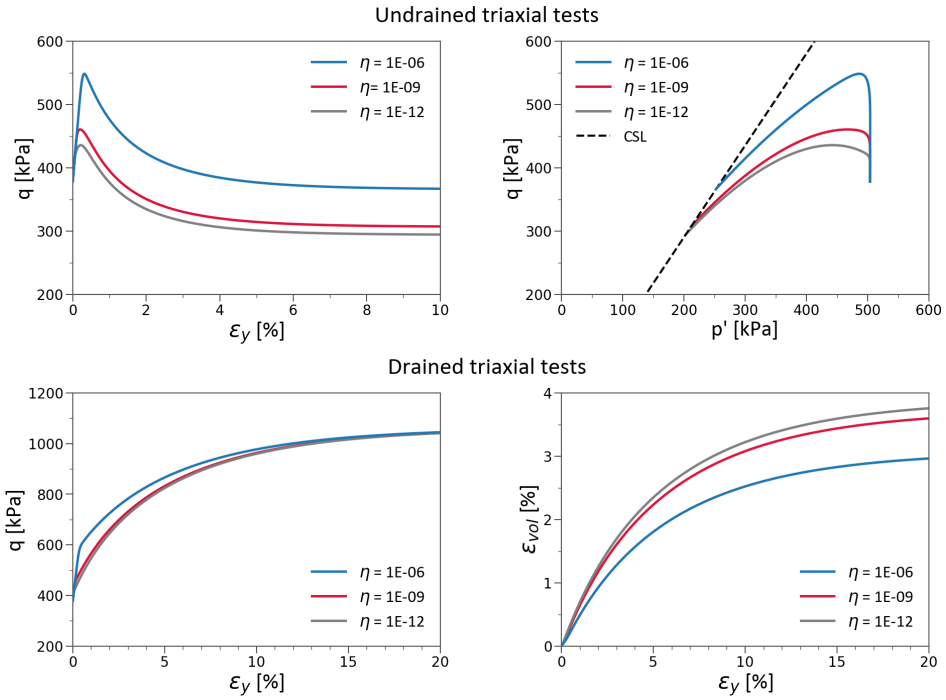

Figure 4.28: Sensitivity analysis results of parameter η.

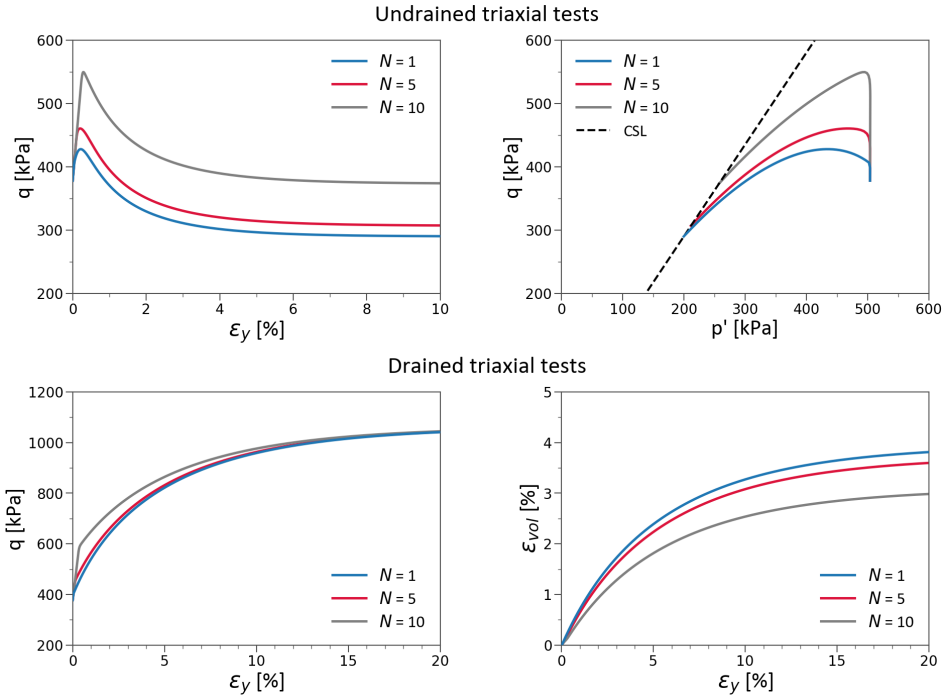

Figure 4.29: Sensitivity analysis results of parameter N.

The effect of the strain rate in the simulations has also been explored, setting N = 5 and eta = 1E-09 (Figure 4.30). When the strain rate is increased, higher peak and residual deviatoric stresses are obtained. This effect on the soil response simulations is consistent with what has been observed by researchers through experimental studies (Casagrande & Shannon, 1949; Lee et al., 1966), which state that an increase in strain rate produces an increase in strength. Additionally, the peak deviatoric stresses are plotted against different strain rates for simulations where η is changed (Figure 4.31). It can be observed a constant increase in the maximum deviatoric stress when the strain rate is increased, as well as practically no effect in the deviatoric stresses (blue dashed line) when the viscosity parameters are defined as zero (i.e. inviscid).

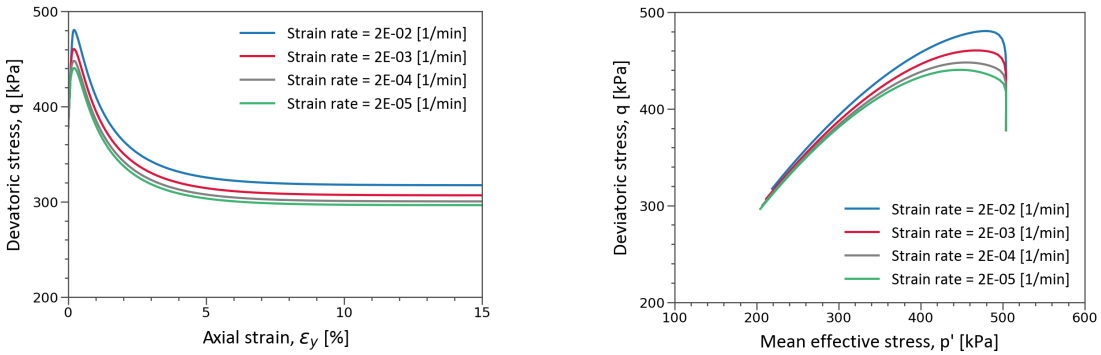

(a) Stress-strain response.

(b) Effective stress paths.

Figure 4.30: Undrained monotonic triaxial compression test simulations for different strain rates.

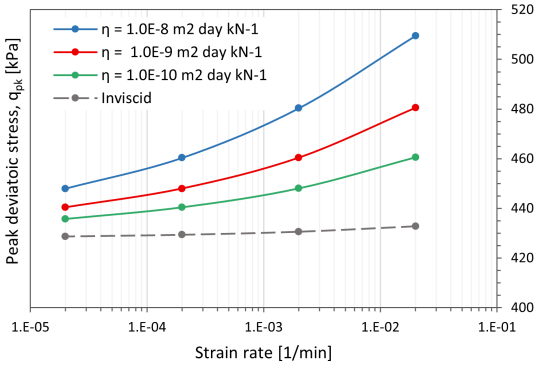

Figure 4.31: Effect of the viscosity parameters in the peak undrained deviatoric stresses.

4.4. NorSand verification

The verification of the NorSand model implementation into PLAXIS has already been carried out by Woudstra (2021). In this research, additional verification simulations were performed in this section comparing the results of single stress point analyses in the PLAXIS SoilTest facility with the results of NorSand implemented in Visual Basic for Applications (VBA) in Excel. This NorSand implementation in VBA was carried out by the authors of the model (Jefferies, 1993; Jefferies & Been, 2015) applying numerical methods to approximate results since NorSand is a non-linear model without a closed-form solution. The Excel VBA version used in this study is version 18.

Drained and undrained monotonic triaxial compression test simulations were performed at this verification stage for which the model parameters and the test conditions applied were obtained from Cheng and Jefferies (2020) and are shown in Table 4.10. Moreover, dense and loose samples defined by the initial state parameter were considered with ψ_0 = -0.05 for the dense material and ψ_0 = 0.05 for the loose material, both subjected to an initial consolidation stress equal to 100 kPa.

Table 4.10: Parameters used in the NorSand verification.

Parameter	G_{ref} [kPa]	p'_{ref} [kPa]	n_G	ν	Γ	λ_e	M_{tc}	N	χ_{tc}	H_0	H_ψ	R	S
Value	30000	100	1	0.15	0.9	0.02	1.2	0.3	3.5	300	0	1	0

The results of the drained and undrained simulations are compared in Figure 4.32 and Figure 4.33, respectively. In both cases, there is a good match between the PLAXIS and the VBA simulations in terms of stress-strain response, as well as in terms of dilative and contractive volumetric behaviour.

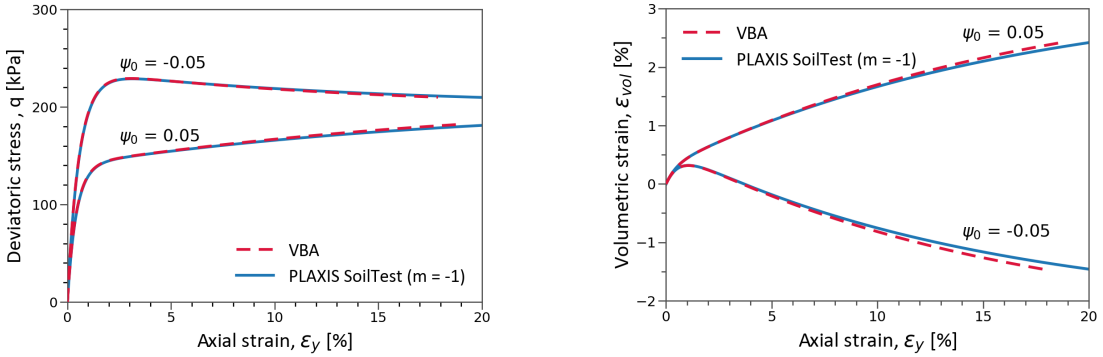

(a) Stress-strain response.

(b) Volumetric strain evolution with axial strain.

Figure 4.32: Drained triaxial compression test simulations comparison between PLAXIS and VBA.

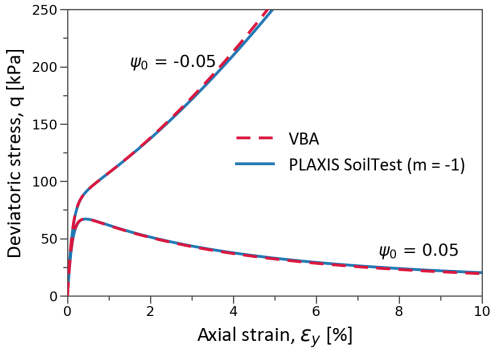

(a) Undrained stress-strain response.

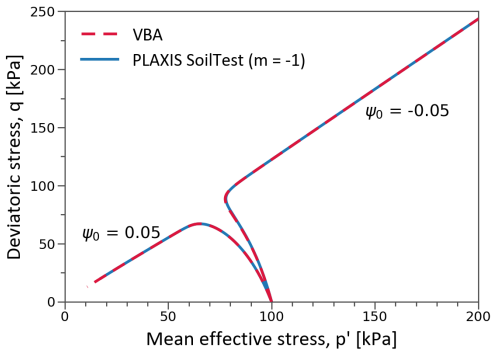

(b) Undrained stress paths.

Figure 4.33: Undrained triaxial compression test simulations comparison between PLAXIS and VBA.

Based on the same set of parameters (Table 4.10), undrained direct simple shear test simulations were performed for both the loose and dense cases. Moreover, the initial consolidation pressure is considered anisotropic with K_0= 0.5 and the initial effective vertical stress equal to 100 kPa. As it can be seen in Figure 4.34, the shear stress-strain response and the stress paths match very well in both cases (loose and dense states). However, slight differences can be observed in terms of stresses that may be the result of the different time stepping used in the implementations.

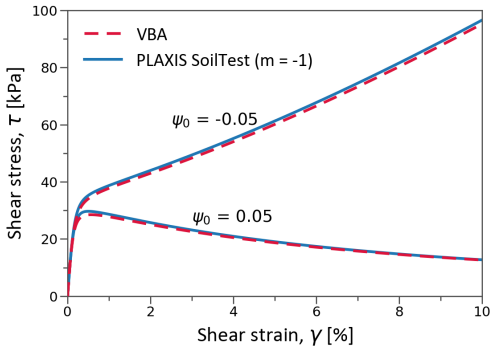

(a) Shear stress-strain response.

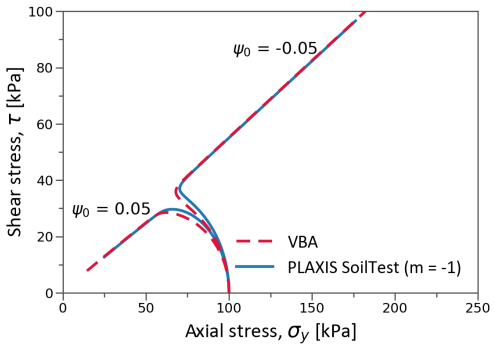

(b) Shear stress evolution with vertical stress.

Figure 4.34: Undrained direct simple shear test simulations comparison between PLAXIS and VBA.

4.5. NorSand sensitivity analysis

Similar to the CASM sensitivity analysis presented in subsection 4.3, in this subsection, a sensitivity analysis has been performed simulating drained and undrained monotonic triaxial compression tests using the SoilTest facility. Naturally, to isolate its influence from those of the other parameters, only a single parameter was varied at each simulation. The parameters analysed are those parameters that are particular to the NorSand model (i.e. N, χ_{tc}, H_0, and H_ψ).

The reference parameters considered for the sensitivity analysis are those found in Shuttle et al. (2021), calibrated for the Mildred Lake tailings (Table 4.11). Moreover, the typical range of parameters proposed by Jefferies et al. (2015) (Table 3.4) were considered for the variable parameters during the sensitivity analysis. An initial isotropic consolidation pressure of 250 kPa was considered for both the looser than the critical state material ($\psi_0 = 0.06$) and the denser than the critical state material ($\psi_0 =$ -0.10).

Table 4.11: Reference NS parameters for the sensitivity analysis.

Parameter	G_{ref} [kPa]	p'_{ref} [kPa]	n_G	ν	Γ	λ_e	M_{tc}	N	χ_{tc}	H_0	H_ψ	R	S
Value	17000	100	0.5	0.2	0.89	0.028	1.29	0.45	4.1	70	775	1	1

The results of the sensitivity analysis are shown from Figure 4.35 to Figure 4.38. These results correspond to the simulations performed for the looser than the critical state material, while the results for the denser than the critical state, which show similar effects, can be found in Appendix A.

The results when the parameter, N is changed are presented in Figure 4.35. The most noticeable effect is observed in terms of peak deviatoric strength. This is explained since the increase of this parameter implies a gentler line in the stress-dilatancy space, which implies smaller maximum stress ratio values. Therefore, increasing the parameter N decreases the peak strength in both drained and undrained conditions in looser than CS material. Similar results with larger effects can be observed in the simulations for the dense material.

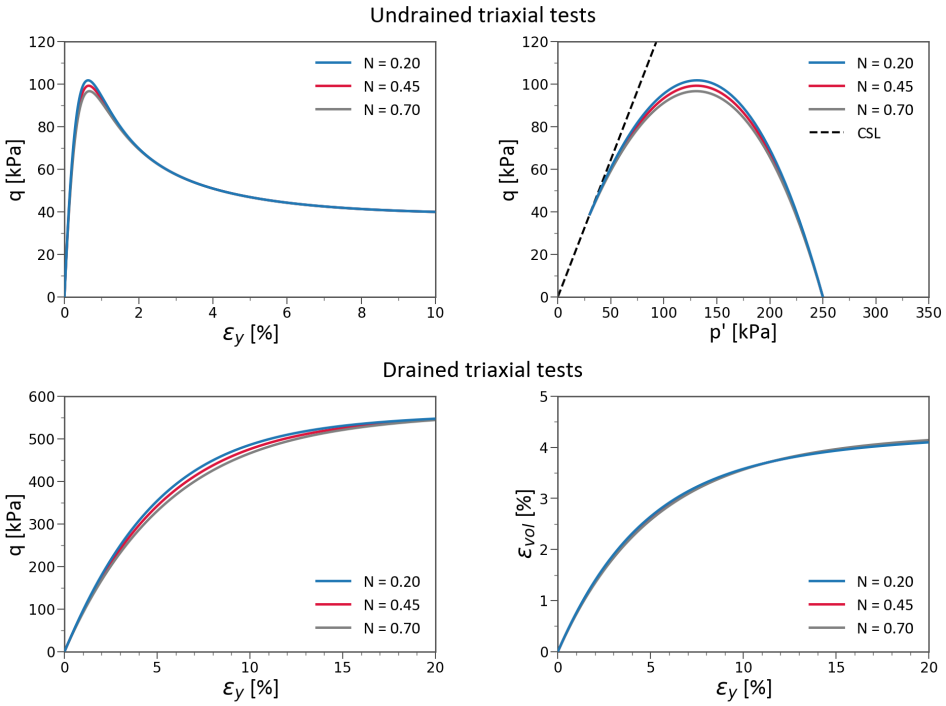

Figure 4.35: Sensitivity analysis results of the volumetric coupling parameter, N, on loose material.

The effect of the variation of the state-dilatancy parameter, χ_{tc}, can be observed in Figure 4.36. Larger values of χ_{tc}, which indicate larger minimum dilatancy for a certain state parameter, lead to lower undrained peak deviatoric stresses. Under drained conditions, a similar response of the deviatoric stresses is observed at smaller axial strains. However, at larger strains, the deviatoric stresses become relatively the same. Moreover, for larger values of χ_{tc}, larger contractive volumetric strains are observed. The opposite response is obtained when simulating dense material, as it can be seen in Figure A.7 in Appendix A.

The increase of the hardening rule model parameter, H_0, implies the increase of the plastic hardening modulus, H, (Eq. 3.58). Larger values of H_0 accelerate the hardening process; therefore, the critical state is reached at smaller strains as it can be seen in Figure 4.37. Moreover, under undrained conditions for loose samples, larger values of H_0 imply larger peak deviatoric stresses, while under drained conditions, a stiffer stress-strain response is observed, as well as smaller volumetric strains. A similar response is obtained for the dense material with larger dilative volumetric strains for larger values of H_0, as it can be observed in Figure A.8 in Appendix A.

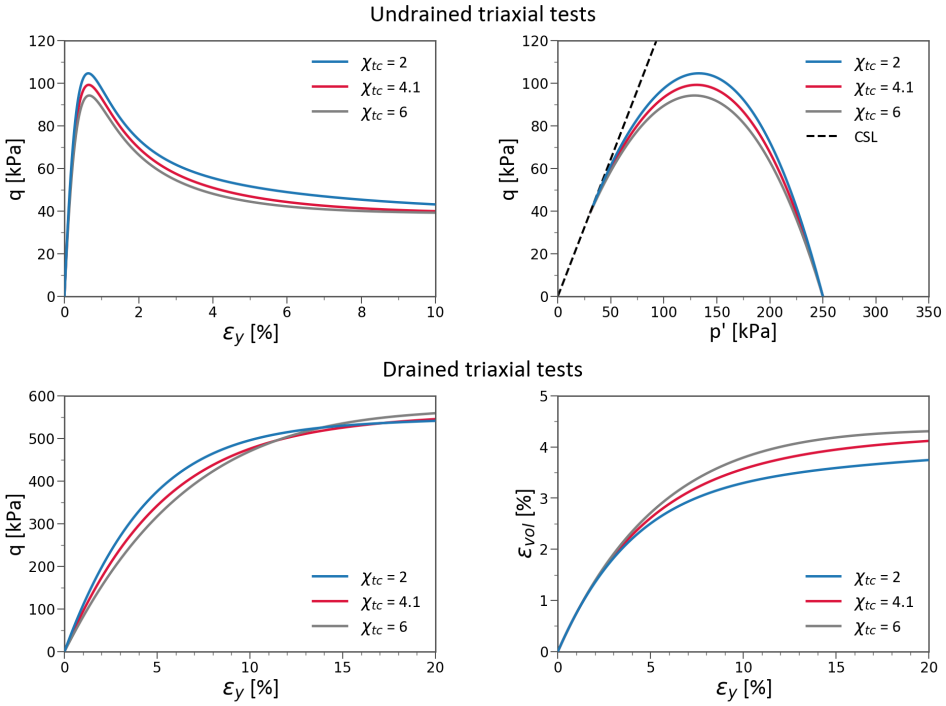

Figure 4.36: Sensitivity analysis results of the state-dilatancy parameter, χ_{tc}, on loose material.

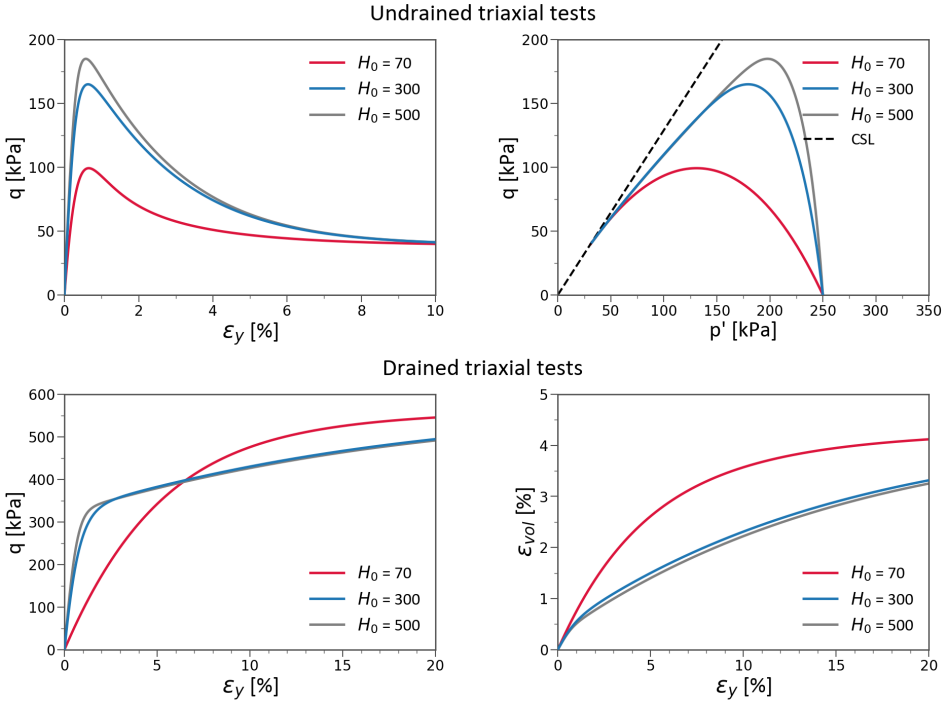

Figure 4.37: Sensitivity analysis results of the hardening parameter, H_0, on loose material.

The effect of the variation of the parameter H_ψ for loose sand has the opposite effect described for the variation of H_0 since the increase of H_ψ leads to a decrease of the plastic hardening modulus (Figure 4.38). Larger values of H_ψ imply lower undrained deviatoric stresses and softer stress-strain response under drained conditions with larger volumetric strains. On the contrary, for dense materials, the effect of H_ψ in the model response is similar to the effect of H_0 due to the cancellation of the negative signs in equation 3.58 by the negative state parameter corresponding to dense materials.

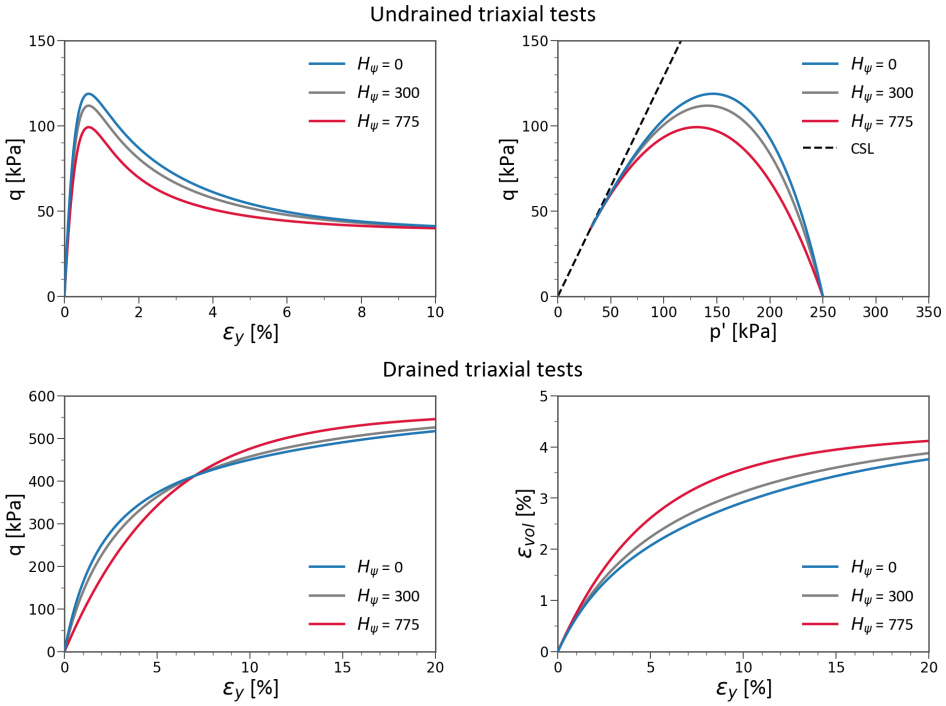

Figure 4.38: Sensitivity analysis results of the hardening parameter, H_ψ, on loose material.

The implementation of CASM into PLAXIS was successfully verified in this section through the comparison of the obtained results with those reported in the literature. The verification exercises consisted of monotonic triaxial compression test simulations and direct simple shear test simulations. Moreover, the model was set to be comparable with Modified Cam-Clay (MCC) model through the definition of certain values for the parameters n, r and m. Two simple boundary value problems were analysed using CASM and MCC and the results in terms of total displacements and stresses show practically the same response. Likewise, additional verification exercises for NorSand are presented with very good agreement between the obtained results with the implementation into PLAXIS and those obtained with the implementation in VBA.

The parametric sensitivity analysis performed for CASM demonstrated the versatility of the model due to the possibility of defining different yield surfaces and plastic potential surfaces. These different surfaces and the parametric analysis of the viscosity parameters showed to have an effect on the response of the model in terms of strength and stiffness. Moreover, the viscoplasticity extension of the model was proven with larger strengths obtained for larger strain rates. Finally, the sensitivity analysis performed for the NorSand parameters showed that the hardening parameters, H_0 and ψ, have a great influence on the model response in terms of strength and stiffness on loose and dense samples, while the effect of the volumetric coupling parameter, N, and state-dilatancy parameter, χ_{tc}, is mostly observed on dense materials.

5

Study case: Tar Island Dyke slump

5.1. Introduction

The mining sector has a fundamental role in the global economy, being one of the main industries for many countries which have thousands of active mines and, therefore, a great quantity of tailings dams with different risk categories. Islam and Murakami (2021) reported mining countries where over the years, tailings facilities incidents generated a large negative impact on the environment and where high-risk tailings are located. Some of these countries are the US and Canada, the latter with the largest oil sand deposit on the planet.

The oil sands or tar sands are sediments or sedimentary rocks composed of sand, clay minerals, water and bitumen. In Canada, the oil sand deposits are found in three regions within Alberta and Saskatchewan, being the Athabasca deposit the largest one in the world (Figure 5.1). The commercial-scale production of this material started in 1967 when the Great Canadian Oil Sands (now Suncor Energy) started the operation for which several tailings facilities were constructed over the years. One of these facilities is the Tar Island Dyke, which is a tailings dam of about 95 m in height built to retain sand tailings. This dyke is located on the west bank of the Athabasca River in Northern Alberta, Canada and is part of the storage facility called Pond 1, as shown in the aerial view in Figure 5.1.

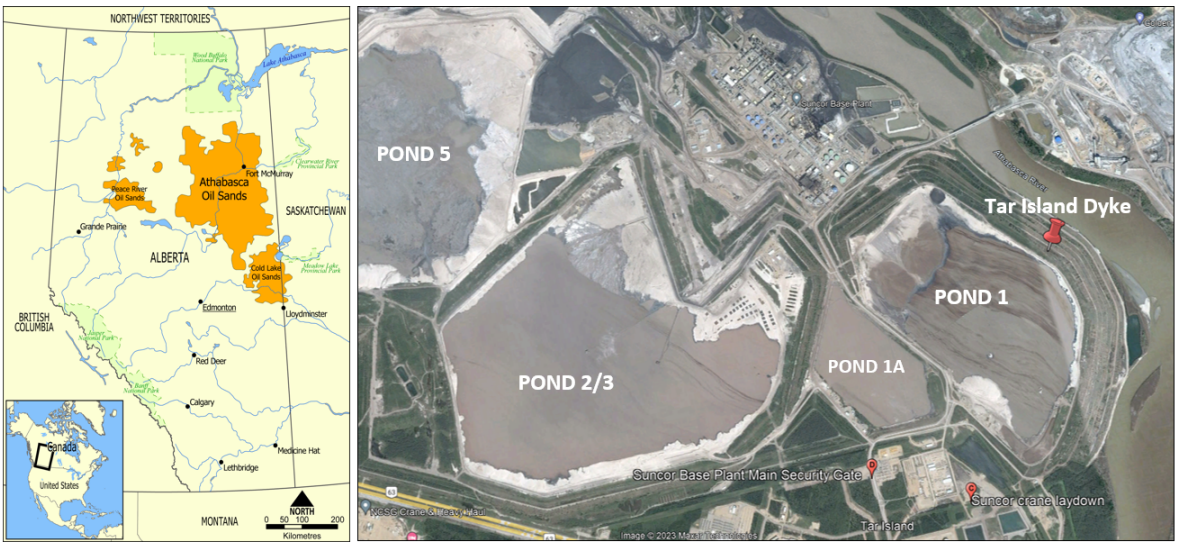

Figure 5.1: Location and aerial view of the Tar Island Dyke in 2006 (Google Earth Pro 7.3.6, 2023).

The Tar Island Dyke has been lifted in phases, experiencing failure events at different magnitudes, with the largest one occurring in 1974 due to flow liquefaction (Plewes et al., 1989). This failure incident is taken as a study case in the present research, and in this chapter, important general aspects are described, as well as a brief geotechnical characterisation of the site, which are useful for the finite element analysis of the event.

5.2. Construction

The construction of the Tar Island Dyke started in the 1960s using a modified upstream construction method which is depicted in Figure 5.2. Initially, the dyke was designed as a 23 m high centreline earth structure built out of overburden that was part of the mining operation. However, in 1967 while the plant was operating, it became evident that the volume of tailings required was greater than the one considered during the design phase. Therefore, the dyke was raised with hydraulically placed sand tailings using a variant of the upstream method of cell construction described by Mittal and Hardy (1977). The construction of the dyke with tailings sand instead of overburden was considered due to the economic factor. The final height of about 95 m was reached in 1984, with additional construction activities at the north end of the dyke until 1986.

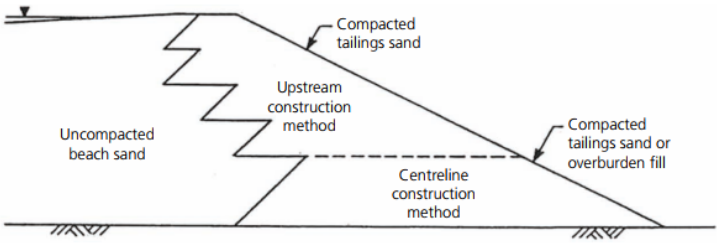

Figure 5.2: Modified upstream method construction of the Tar Island Dyke (Plewes et al., 1989).

The adopted modified upstream construction method employed resulted in three different zones within the earth structure and the adjacent tailings. These zones are identified in Plewes et al. (1989) and Shuttle et al. (2021) as compacted tailings sands or overburden fill; hydraulically placed tailings sand deposited on beaches above the pond surface ('beach above water': BAW), and hydraulically placed sand deposited below the pond surface ('beach below water': BBW). The compacted fill consisted of tailings cells 500-700 m long and 30-90 m wide, oriented parallel to the centreline of the dyke. The sand beaches were formed by discharging tailings from the upstream dyke crest, with the finer-size tailings travelling into the pond to form the BBW zones and the coarser-size tailings forming the BAW zones, whose length depended on the pond level.

5.3. Liquefaction event, August 1974

While the dyke was raised, four flow liquefaction events leading to slumps were reported at the upstream face of the Tar Island Dyke between 1972 and 1974 (Plewes et al., 1989). These events did not affect the integrity and stability of the dyke; however, they represented a significant risk for the operating personnel and equipment during the construction phase of the structure.

The largest slump took place on August 23, 1974, when the dyke was about 60 m in height. It is reported that when this slump occurred, a compacted cell of 12.8 m thick and about 36 m wide with a front slope of 1V:1H was being placed on an approximately 9 m thick layer of BBW sand recently deposited. The cell was placed in five lifts over the period from May 14 to August 22, 1974, as detailed in Figure 5.3, resulting in an estimated average rise rate of 0.1m/day (Shuttle et al., 2021).

During the construction of the first four lifts, it was not reported any failure signals, and the slump started near the completion of the last lift when the final compaction works were being carried out. Plewes et al. (1989) describes some essential aspects of the subsidence, which are fundamental for assessing the failure. The whole 36 m compacted cell settled about 4.5 m with the surface slightly

tipped toward the pond, and the subsidence spread along the upstream dyke crest approximately 460 m. This was important to the failure to be defined as a plane-strain event by Shuttle et al. (2021) since the ratio of the slump was 13:1. Moreover, no uplift at the toe of the upstream face of the compacted cell was observed, and the tailings sand from the cell did not liquefy, behaving as a rigid slab.

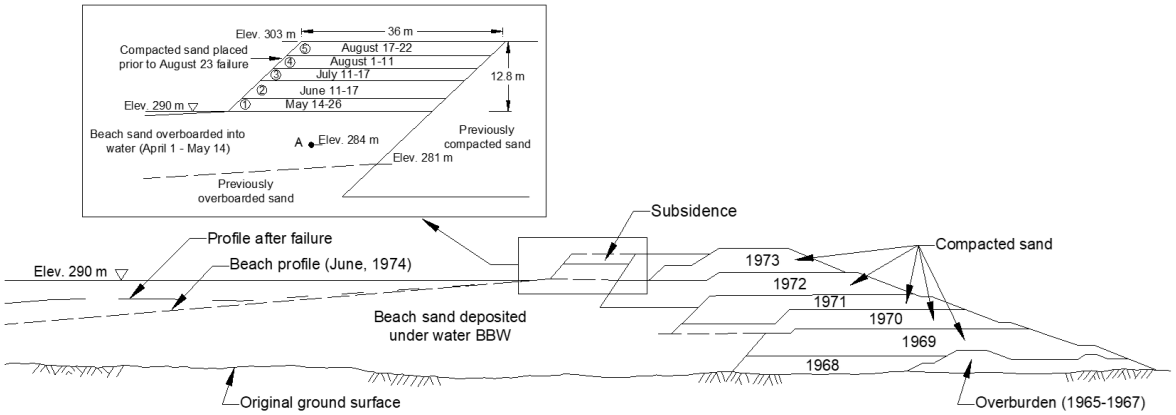

Figure 5.3: Upstream liquefaction subsidence at Tar Island Dyke - August 23, 1974 (Altered from Plewes et al. (1989)).

It was concluded that the cause of the slump was liquefaction. The BBW beach sand below the cell liquefied and flowed out into the pond, generating a rapid failure and a soil movement that extended about 250 m. As described in Plewes et al. (1989), the construction rate and the height of the compacted cell are believed to be the trigger of liquefaction since both the rate of construction during the last lift (0.3 - 0.35 m/day) and the height of the cell were greater than previously experienced.

5.4. Brief description of the geotechnical site characterisation

The geotechnical site characterisation considered for the Tar Island Dyke model in this study corresponds to the presented in Shuttle et al. (2021), which used field and laboratory data. The field data were obtained from CPT soundings which were not exactly performed in the area of failure. Nevertheless, was useful since the soundings were carried out in adjacent areas where the tailings have remained from the same source, and the construction methods have not suffered any alteration. The experimental laboratory data comprises sieve analysis and monotonic triaxial compression tests performed on samples obtained near the area with tailings derived from the same McMurray Formation. The set of triaxial test data is termed Mildred Lake.

Assessing the in situ conditions of the tailings was fundamental for defining the material properties in the numerical model. From laboratory tests, it was determined that the sand tailings presented in the site contained uniform fine to medium sand with the presence of silt. The particles were distributed during deposition, with the fines retained mainly in the BBW zone. The density of the tailings was determined by means of downhole nuclear logging techniques (Plewes et al., 1988), the results o which are presented in Table 5.1 together with the unit weights of the tailings.

Table 5.1: Summary of bulk unit weights by tailings deposition environment (Shuttle et al., 2021).

Zone	Nuclear-logged density [kg/m^3]	Representative unit weight [kN/m^3]
Compacted tailings cell above water table	1850 - 1980	18.6
Compacted tailings cell below water	1980 - 2060	19.6
BAW	1950 - 2000	19.1
BBW	1880 - 1930	18.8

The state conditions of the tailings were assessed by Shuttle et al. (2021) using the concept of the state parameter, which was computed using the CPT data shown in Figure 5.4. These data belong to four soundings carried out along the impoundment, extending from the cell across the BAW over a horizontal distance comparable to the distance of the slump propagation. The CPT results denote variation in the tailings that follow the deposition trend with the presence of a dense layer depicted by the dashed line AA in the figure. Shuttle et al. (2021) describe this dense layer as a possible BAW zone from an earlier stage of the impoundment, and the tailings above this layer are considered as BBW.

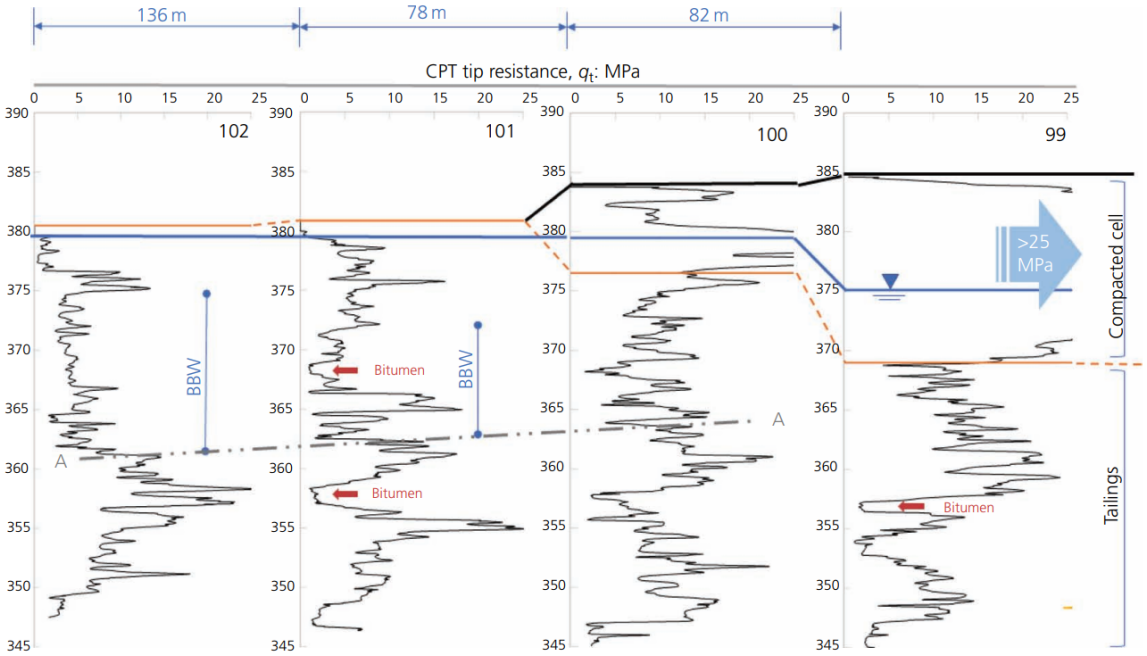

Figure 5.4: CPT tests results. Line AA is an example of an apparent top of 'previously over-boarded sand' (Shuttle et al., 2021).

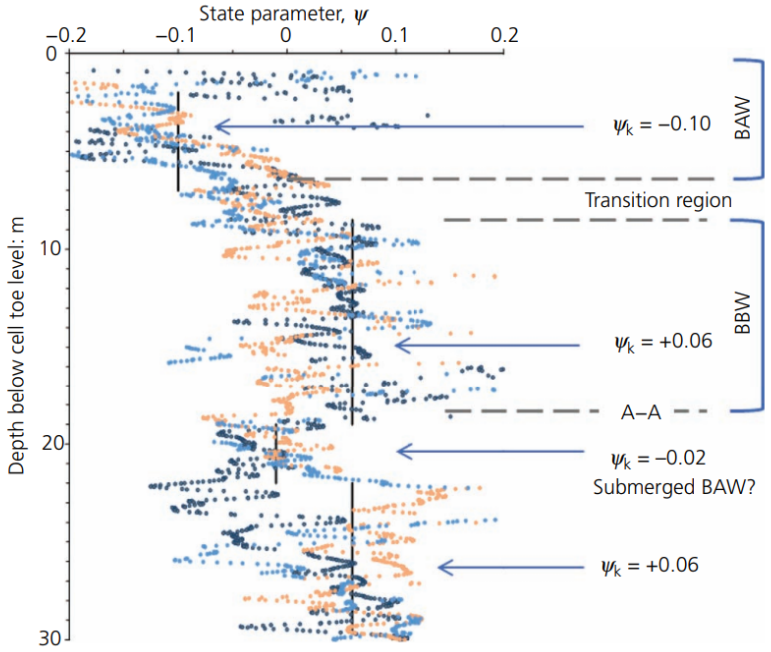

Figure 5.5: In situ state of tailings from inversion of three CPT soundings (Shuttle et al., 2021).

Based on the two upstream CPT results and the CPT carried out in the newly placed cell (Figure 5.4), the in situ state parameters were computed, and the results are presented in Figure 5.5. The three different soundings are shown on the same plot in terms of state parameter with depth, taking the toe of the cell as a reference level. Moreover, four zones, defined by a characteristic state parameter, ψ_k, can be distinguished. Starting from the surface to a depth of around 5 m, a layered stratum of BAW deposition comprising non-liquefying materials is defined by a characteristic state parameter, ψ_k = -0.10. The BAW stratum is underlain by a transition zone from dense to loose material, which is considered part of the BAW stratum. Underneath the transition zone, a large BBW zone extending to a depth of about 19 m is identified. This layer comprises loose tailings characterised by $\psi_k = 0.06$. Underlying this zone, a 3 to 5 m thick dense layer was identified, which is believed to be an earlier BAW presenting looser state conditions (ψ_k = -0.02) than the BAW layer on the top. Finally, the last zone presents more variable state conditions, possibly due to hydraulic segregation and is characterised by $\psi_k = 0.06$; however, a more contractive material can also be considered (Shuttle et al., 2021).

The Tar Island Dyke flow liquefaction event of August 1974 is a perfect alternative to test the capabilities of the models simulating a flow failure due to the information and observation records provided in Plewes et al. (1989) and Shuttle et al. (2021). The information described above, together with experimental data corresponding to the Albian tailings and Mildred Lake tailings, are the starting point of the calibration of the models and their further application at a material point level and boundary value problem level described in the next chapters.

6

CASM calibration and validation for Tar Island tailings

6.1. Introduction

Constitutive soil models are frequently calibrated against experimental data to obtain a model capable of predicting accurately the response of soils. The calibration process consist of determining or estimating the values of the model parameters through procedures where experimental data is often used as well as empirical formulations. The calibration exercise provides insight into the ability of the model to describe real soil response and, therefore, is crucial for the validation of the model.

In Shuttle et al. (2021), NorSand model is calibrated against field and laboratory test data and, subsequently, applied to the simulation of the well-known flow liquefaction case of the Tar Island Dyke slump. The calibration was carried out for two materials: Mildred Lake and Albian tailings. In this chapter, the information provided in the mentioned source (i.e. Shuttle and Jefferies (2010)) was used to calibrate CASM for the same tailings and later compare its performance with NorSand when simulating laboratory tests. Moreover, some validation exercises are performed by comparing the numerical results against available experimental data.

6.2. Available data

The information used to perform the calibration includes CPT soundings carried out in the Tar Island Dyke slump area, some of them including geophones used to measure the shear wave velocity, from which the elastic shear modulus can be estimated. Moreover, other relevant test data is available for the two 'in situ' tailing materials: Mildred Lake and Albian. Data available for the Mildred Lake tailings comprises drained monotonic triaxial compression tests for dense samples, while data available for the Albian data includes drained monotonic triaxial compression tests for both loose and dense samples. This information was obtained from Jefferies and Been (2015) and Shuttle and Jefferies (2010).

6.3. Calibration strategy

As already described, as it is implemented in PLAXIS, CASM requires a minimum of 8 model parameters (κ, ν, λ, Γ, ϕ_{cs}, n, r, and m). Some of these parameters, namely κ, ν, λ, Γ, and ϕ_{cs}, have a clear physical meaning, and their values can be simply obtained by curve fitting over conventional experimental data. The calibration of the remaining parameters n, r, m is often more challenging since a larger number (and/or types) of laboratory tests than typically available or additional assumptions may be required.

6.3.1. Critical state parameters

The estimation of the critical state parameters λ, Γ, and ϕ_{cs} is often carried out using lab test data, as described in Been et al. (1991), where a critical state line (CSL) is defined for the Erksak 330/07 sand using triaxial compression test data. The CSL is defined in the $\ln p'$ - v space as the line that best fits

the points that have reached critical state conditions (i.e. no change in stress and volume with further shear straining). In the mentioned space, the CSL is defined by the parameters λ and Γ while in the p'-q space, the slope of the CSL is defined by the parameter M, which is used to determine the parameter ϕ_{cs} by means of Eq. (3.26).

Since one of the objectives of this study is to compare simulations performed with CASM and NorSand, and assuming that a unique CSL exists for a given material, the Critical State Lines proposed by Shuttle et al. (2021) for the Mildred Lake and Albian tailings were also adopted for the calibration of CASM. The corresponding model parameters are presented in Table 6.1.

Table 6.1: Parameters used in the CASM verification for the direct simple shear tests.

Tailings	λ	Γ	ϕ_{cs}
Mildred Lake	0.02826	1.890	32.06°
Albian	0.01913	1.849	34.35°

Shuttle and Jefferies (2010) recommended an alternative to estimate the parameter M using data from drained triaxial compression tests on dense samples. This alternative consists of plotting the peak stress ratio, $\eta_{\max} = q_{peak}/p'$ against the minimum dilatancy, D_{min} (i.e. the minimum due to the tension negative convention), where M is defined by extrapolating the stress ratio at $D = 0$, as shown in Figure 6.1 for the Mildred Lake ($M = 1.29$) and Albian ($M = 1.39$) tailings. Having estimated the values of M, it is possible to determine the corresponding values of ϕ_{cs} using equation (3.26), resulting, in this case, in $\phi_{cs} = 32.06°$ for the Mildred Lake tailings and $\phi_{cs} = 34.35°$ for the Albian tailings.

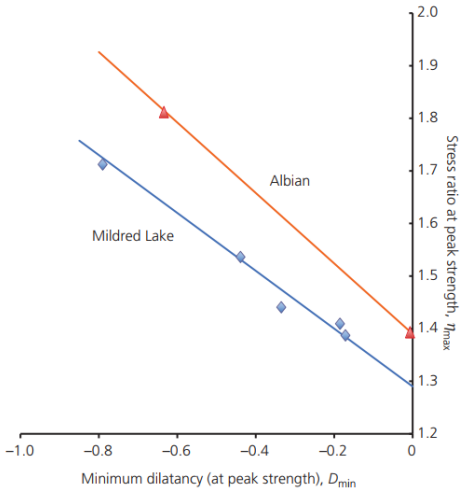

Figure 6.1: Stress ratio at peak strength evolution with minimum dilatancy for Mildred Lake and Albian tailings. (Shuttle et al., 2021).

6.3.2. Elasticity parameters

Shuttle et al. (2021) calibrated the elasticity parameters of NorSand - G_{max} and n_G - based on data inferred from seismic CPTs carried out in the Tar Island tailings site. These parameters were estimated by fitting the constitutive equation for the elastic shear modulus, G, to the lower bound of the inferred experimental data, as shown in Figure 6.2. This resulted in $G_{max} = 50$ MPa for a reference pressure of $p'_{ref} = 100$ kPa and with the exponent $n_G = 0.5$.

The CASM elasticity parameters κ and ν were estimated based on a similar methodology. Recalling that CASM defines a linear dependency of G on the specific volume and mean effective stress, a line passing through the lower bound of the inferred experimental data was defined, as shown in Figure 6.2. This procedure results in $\kappa = 0.004$, with the Poisson's ratio being set as $\nu = 0.2$, which lies within the

range of $0.1\lambda < \kappa < 0.4\lambda$ suggested in Jefferies and Been (2015) and also represented in the figure with dashed lines.

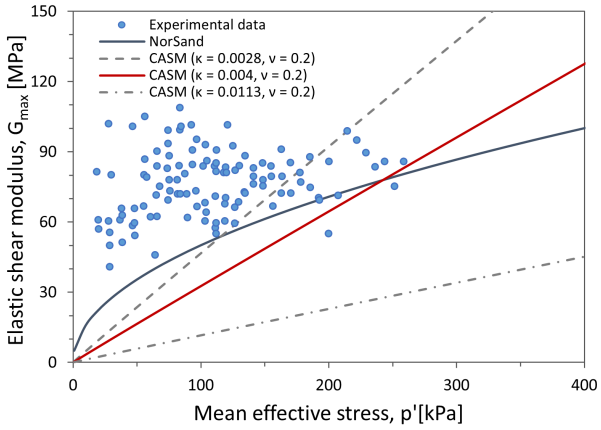

Figure 6.2: Estimation of the evolution of the maximum shear modulus with the mean effective stress (data from Shuttle et al. (2021)).

6.3.3. Plasticity parameters

- **Estimation approaches**

Yu et al. (2005) describes an approach to estimate the parameters n and r against laboratory test data. The parameter n can be determined by plotting the stress ratio - state paths measured in some triaxial tests (both drained and undrained) conducted on samples subjected to different initial states in terms of stress ratio, η, evolution with the state parameter, ψ (Figure 6.3). Using the general stress-state relation adopted in CASM (Eq. 3.13), the experimental boundary surfaces should be regarded as a straight line in the plot of $\ln(1 - (\psi/\psi_R))$ against $\ln(\eta/\mathrm{M})$, with the stress-state coefficient, n, being the slope of the state boundary surface in this particular log-log plot as shown in Figure 6.3. Regarding the spacing ratio, r, it can be determined from Eq. (3.10) assuming the reference state parameter, ψ_R, to be equal to the initial state parameter, ψ_0, of the loosest sample.

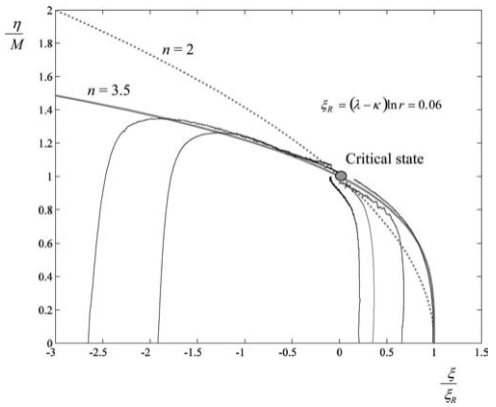

Figure 6.3: Determination of the stress-state coefficient, n, from drained and undrained triaxial tests (Yu et al., 2005).

An alternative to the estimation approach by Yu et al. (2005) is described by Mánica et al. (2022). This approach considers that tailings are found in normally consolidated conditions. Under these conditions, CASM formulation imposes that all constant η stress paths correspond to a unique state parameter described by Eq. (6.1). This equation establishes a relationship between the parameters n and r for a given state parameter. Note, however, that an additional relationship is required to calibrate the two parameters mentioned above.

$$\psi = (\lambda - \kappa) \ln r \left[1 - \left(\frac{\eta}{M}\right)^n\right] \tag{6.1}$$

Note also that, for normally consolidated conditions, it is generally preferred to define the initial state of the material using the state parameter, ψ_0 rather than specific volume, v_{ini}, or void ratio, e_{ini}, since these last two generally vary with depth and might be difficult to estimate with a good degree of accuracy (Mánica et al., 2022). The initial specific volume can be initialised in terms of the initial state parameter by considering:

$$v_{ini} = \psi_0 + \Gamma - \lambda \ln p'_{ini} \tag{6.2}$$

The additional relationship required for the calibration of the parameters n and r is obtained by introducing the normalised peak undrained shear strength concept within the CASM formulation. For this, the relationship defined by Eq. 6.3, which is proposed as a calibration constraint in (Mánica et al., 2022) is used.

$$S_p = \frac{s_{u,peak}}{p'_{ini}} \tag{6.3}$$

Where $s_{u,peak}$ is the peak undrained strength that can be related to the CASM parameters assuming that this is reached when the stress state is at the highest point of the yield surface. The stress ratio at this point is determined by Eq. (6.4), and the peak deviatoric stress is defined in terms of the undrained strength ratio as shown in Eq. (6.5).

$$\eta_{peak} = \frac{q_{peak}}{p'_{peak}} = \frac{M_\theta}{\sqrt[n]{n \cdot \ln r}} \tag{6.4}$$

$$q_{peak} = 2S_p \cdot p'_{ini} \tag{6.5}$$

As normally consolidated conditions are assumed, the initial stress state lies on the yield surface as shown in Figure 6.4. Therefore, the initial hardening parameter, p'_0 can be derived from the yield surface function (Eq. 3.19) resulting in the Eq (6.6).

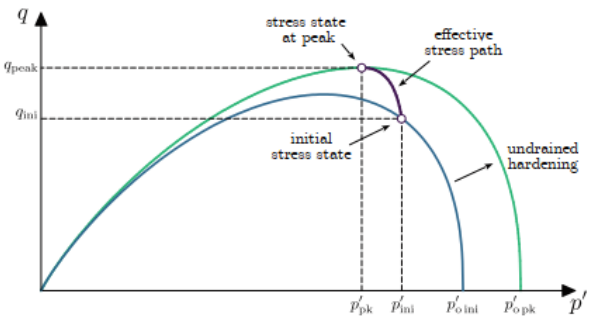

Figure 6.4: Hardening during undrained loading in CASM (Mánica et al., 2022).

$$p'_{0,ini} = p'_{ini} \exp\left[\left(\frac{\eta_{ini}}{M_\theta}\right)^n \ln r\right] \tag{6.6}$$

At peak, the stress state remains on the yield surface, obtaining a similar relationship:

$$p'_{0,peak} = p'_{peak} \exp\left[\left(\frac{\eta_{peak}}{M_\theta}\right)^n \ln r\right] \tag{6.7}$$

Furthermore, since the total volume remains constant during undrained loading, elastic and plastic volumetric deformations must be equal with opposite signs, as shown in the following equation:

$$(\lambda - \kappa) \ln\left(\frac{p'_{0,peak}}{p'_{0,ini}}\right) = -\kappa \ln\left(\frac{p'_{peak}}{p'_{ini}}\right) \tag{6.8}$$

The relationship that relates the unknown parameters n and r can be derived by substituting Eq. (6.4) to (6.7) into (6.8) resulting the Eq 6.9.

$$\exp\left[\left(\frac{1}{\sqrt[n]{n \cdot \ln r}}\right)^n \ln r\right] = \frac{M}{2S\sqrt[n]{n \cdot \ln r}} \cdot \exp\left[\left(\frac{\eta_{ini}}{M}\right) \ln r\right] \cdot \exp\left[\frac{\kappa}{\lambda - \kappa} \ln\left(\frac{M}{2S\sqrt[n]{n \cdot \ln r}}\right)\right] \tag{6.9}$$

As explained in Mánica et al. (2022), an iteration procedure is necessary to determine the two model parameters from Eq. (6.9), where a first estimation of r can be carried out by neglecting the terms in brackets in Eq. (6.1).

• Estimation of parameters n and r

Since available triaxial test data is very limited in the present study, the approach followed to estimate the parameters n and r is the one described by Mánica et al. (2022). To solve Eq. (6.9), the initial stress ratio, η_{ini} is calculated using Eq. (6.10) with $K_0 = 0.6$, which was determined in oilsand tailings (Shuttle et al., 2021). The undrained strength ratio, S, is calculated using the correlation proposed by Olson and Stark (2003), which correlates the normalised peak undrained shear strength with the corrected CPT tip resistance, q_t, as described by Eq (6.11). Note that this correlation normalises the undrained strength with the effective vertical stress; therefore, Eq (6.12) is used to calculate the undrained strength normalised by the mean effective stress.

$$\eta_{ini} = \frac{3(1-K_0)}{1+2K_0} \tag{6.10}$$

$$S_{p_{\sigma'_{v0}}} = \frac{s_{u,peak}}{\sigma'_{v0}} = 0.205 + 0.0143 q_t \pm 0.04 \tag{6.11}$$

$$S_{p_{p'}} = \frac{3 S_{p_{\sigma'_{v0}}}}{1+2K_0} \tag{6.12}$$

From the CPT data available in Shuttle et al. (2021), an average corrected tip resistance that is equal to 6.5 MPa was estimated for both tailings, resulting in a normalised peak undrained shear strength, $S_{p_{p'}}$, equal to 0.46. The parameter r was first estimated neglecting the terms in brackets in Eq (6.1) using as state parameter the value characterising the loosest sample ($\psi_k = 0.028$). Afterwards, the parameter n was evaluated solving Eq. (6.9). Having followed this procedure, the parameters n and r for the Albian tailings were estimated as 8.7 and 6.4, respectively. The same procedure was followed for the Mildred Lake tailings, with n being estimated as 7.9 and r as 11.9.

• Estimation of parameter m

The plastic potential shape controlling parameter, m, can be related directly to the coefficient of earth pressure at rest, K_0, and the critical state parameters. From oedometer conditions tests, the following relationship is established (Mánica et al., 2022):

$$\frac{9(\lambda-\kappa)(2\nu-1)}{2\kappa\eta_{K_0}(\nu+1)+6\lambda(2\nu-1)} = \left(\frac{M}{m}-M\right)\frac{\eta_{K_0}}{M} + \left(M-\frac{M}{m}\right)\left(\frac{\eta_{K_0}}{M}\right)^{1-m} \tag{6.13}$$

Where the stress ratio in one-dimensional consolidation η_{K_0} is given by equation 6.14

$$\eta_{K_0} = \frac{3(1-K_0)}{1+2K_0} \tag{6.14}$$

In order to estimate the parameter m for the Tar Island tailings, equations (6.13) and (6.14) were used, using the critical state parameters and elasticity parameters already estimated together with K_0 = 0.6. A value of $m = 2$ was obtained for the Albian tailings, while $m = 2.05$ was estimated for the Mildred Lake tailings. It should be noted that if oedometer test results would have been available, the parameter m could have been alternatively calibrated by simulating this type of test and comparing the obtained stress path against that measured in the laboratory.

Available experimental data of the Mildred Lake tailings were used to verify the calibration of the parameter m. The evolution of the stress ratio with dilatancy measured in a series of drained triaxial compression tests performed on dense Mildred Lake tailings samples are plotted in Figure 6.5 together with a set of curves arising from using the stress-dilatancy relationship implemented in CASM (Eq. 3.30) with different values for the parameter m, including the value estimated (i.e. $m = 2.05$). It can be observed that when the parameter m is equal to 2.05, the analytical stress-dilatancy curve exhibits a qualitatively similar trend to that corresponding to the experimental data, while it deviates for larger values of m. Note that in the model implementation, the minimum possible value to define

the parameter m is 2 and, therefore, $m = 2.05$ was the minimum value used in this small parametric study.

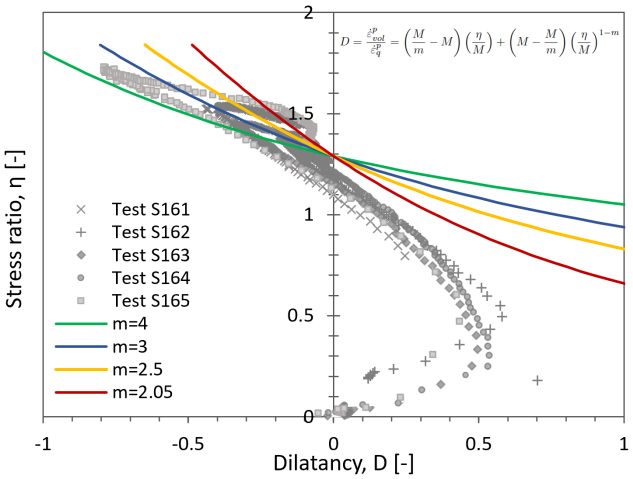

Figure 6.5: Stress-dilatancy relationship for the Mildred Lake tailings.

A summary of the CASM parameters calibrated for the Albian and Mildred Lake tailings is presented in Table 6.2. It is important to note that a single set of parameters was defined for each material, since the model accounts for the state of the material.

Table 6.2: CASM parameters for the Tar Island tailings.

Parameters	λ	κ	ν	ϕ_{cs}	Γ	n	r	m
Albian tailings	0.01913	0.004	0.2	34.35°	1.849	8.7	6.4	2
Mildred Lake tailings	0.02826	0.004	0.2	32.06°	1.89	7.9	11.9	2.05

6.4. CASM validation for Tar Island tailings

The validation of a model implies assessing its capability to reproduce accurately the behaviour observed in reality (e.g. in laboratory tests). Using the calibrated sets of parameters indicated in the previous subsection (Table 6.2), the ability of CASM is assessed by simulating drained monotonic triaxial compression tests on Albian and Mildred Lake tailings samples and comparing the computed results with experimental data. Similarly, simulations were also conducted using NorSand with the parameters presented in Table 6.3 and the obtained results compared against those measured in the laboratory. The SoilTest facility of PLAXIS was used to perform the simulations.

Table 6.3: NorSand parameters for the Tar Island tailings.

Parameters	G_{ref}	p'_{ref}	n_G	ν	Γ	λ_e	M_{tc}	N	χ_{tc}	H_0	H_ψ
Albian tailings	50 MPa	100 kPa	0.5	0.2	0.849	0.01913	1.39	0.33	4.1	150	775
Mildred Lake tailings	50 MPa	100 kPa	0.5	0.2	0.890	0.02826	1.29	0.45	4.1	70	775

6.4.1. Drained monotonic triaxial compression tests on Albian tailings

Drained monotonic triaxial compression test simulations were performed for a loose and a dense sample of Albian Lake tailings consolidated under isotropic consolidated conditions. The initial state of the samples was defined by setting the state parameter as input. For the loose sample, the initial state parameter, ψ_0, is equal to 0.028, while for the dense, it is equal to -0.185. An initial effective cell pressure of 100 kPa was used in both simulations.

Figure 6.6 shows the results of the simulations for the loose sample using CASM and NorSand and compares them with the experimental data. A very good agreement between the numerical results and the experimental data can be observed in terms of deviatoric stress evolution and volumetric strains. For the simulation results with CASM, it is observed that the peak deviatoric stress matches very well with the experimental data, although a slightly stiffer stress-strain response can be observed at the early stages of loading. Moreover, it can be observed that the numerical results for the evolution of the volumetric strains match very well with the experimental data, with only very slight differences at large strains.

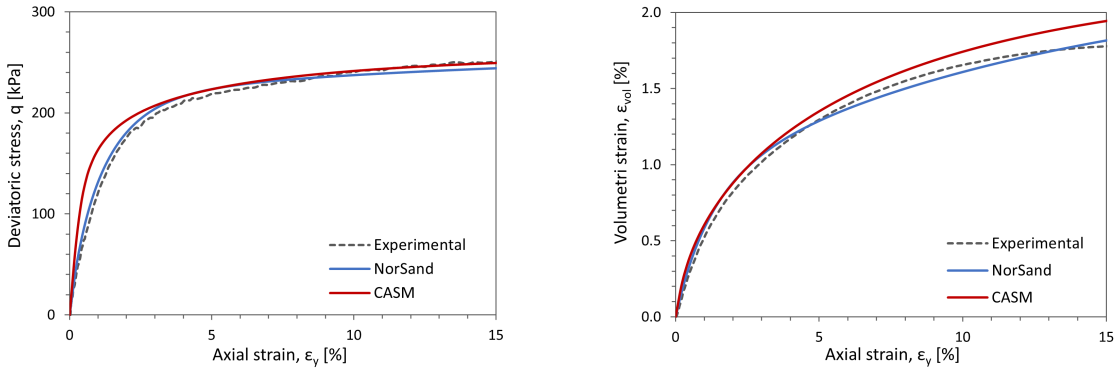

(a) Stress-strain response. **(b)** Volumetric strain evolution with axial strain.

Figure 6.6: Drained monotonic triaxial compression test on a loose sample of Albian tailings.

In Figure 6.7, the stress paths for the numerical simulations performed on loose sample are presented in the p' - q and lnp' - e spaces, as well as the initial yield surfaces. As observed in the p' - q space, both simulations start at normally consolidated conditions, with the yield surfaces being relatively similar in size. In the lnp' - e space, the NorSand normal compression line (NCL) and CASM reference consolidation line (RCL) are located in the same position.

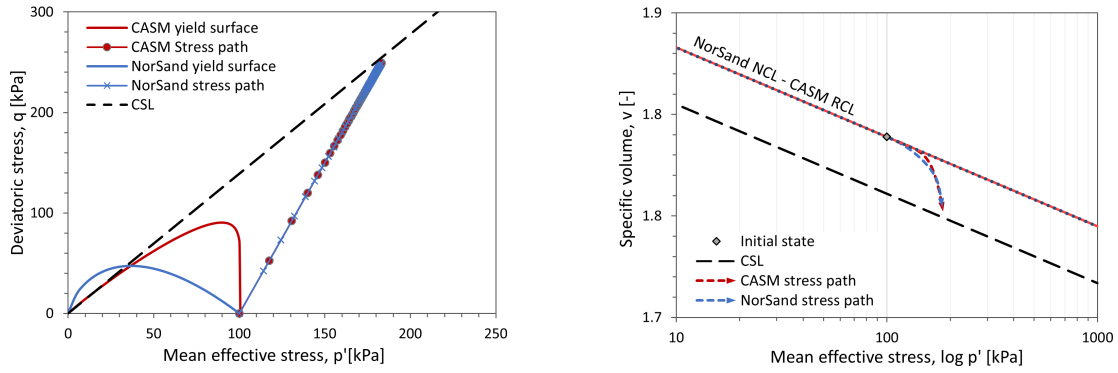

(a) Stress paths and initial yield surfaces in the p' - q space. **(b)** Stress path evolution in the lnp' - e space.

Figure 6.7: Stress paths evolution for drained monotonic triaxial test on a loose sample of Albian tailings.

The results of the simulations for the Albian dense sample are shown in Figure 6.8. In this case, the results of the numerical simulations, particularly those obtained when using CASM, do not match so well experimental data as for the loose sample. A stiffer stress-strain response is observed at the early stages of loading, followed by an apparent linear softening. Moreover, in terms of volumetric strains, CASM seems to start dilating earlier than what is observed in the laboratory, underpredicting the rate of dilation as well.

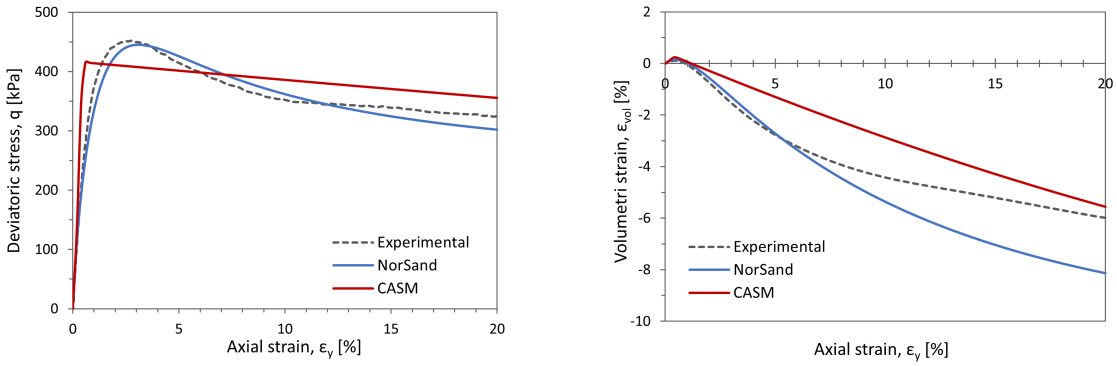

(a) Stress-strain response. **(b)** Volumetric strain evolution with vertical strains.

Figure 6.8: Drained monotonic triaxial compression test for a dense sample of Albian tailings.

The corresponding stress paths of the simulations on the dense Albian tailings are depicted in Figure 6.9. In the p' - q space (Figure 6.9a), it is observed that the response obtained with CASM is elastic almost until reaching the peak deviatoric stress. On the contrary, the initial stress state when using NorSand starts on the yield surface. Moreover, the initial yield surface for each model is very different, with CASM being characterised by a very large yield surface, as shown in the subfigure. This can be explained considering that, in the lnp' - v space (Figure 6.9b), contrary to the simulations for the loose samples, the NCL and the RCL are not located in the same position. Since NorSand does not consider a single NCL, the simulation of denser than critical state samples (i.e. $\psi_0 < 0$) is allowed to start at normally consolidated conditions (e.i. the initial state starts at the NCL in the lnp' - e space and the initial stress state starts on the yield surface in the p'- q space). Conversely, the RCL line of CASM is unique and always lies on the right side of the CSL. As such, a normally consolidated state can only be described by a point on this line, meaning that a dense sand is always assumed to be overconsolidated.

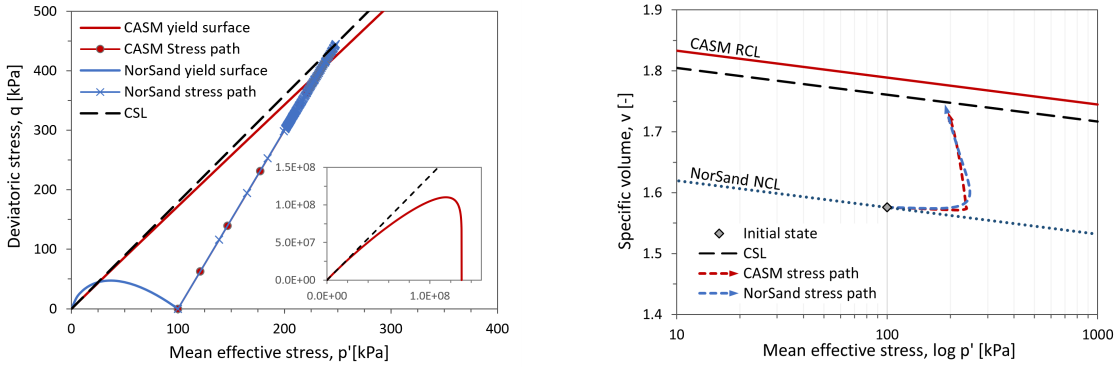

(a) Stress paths and initial yield surfaces in the p' - q space. **(b)** Stress path evolution in the lnp' - e space.

Figure 6.9: Stress paths evolution for drained monotonic triaxial test on a dense sample of Albian tailings.

6.4.2. Drained monotonic triaxial compression tests on Mildred Lake tailings

Two drained monotonic triaxial compression tests on Mildred Lake tailings were simulated using CASM with the parameters shown in Table 6.2. The results of these simulations were compared with those simulated with NorSand and experimental data. The simulations correspond to triaxial compression tests termed S161 and S163, which were performed on denser than the critical state samples. For the S161 test, an initial effective cell pressure, σ'_x, equal to 100 kPa was applied to a sample with an initial state parameter, ψ_0, equal to -0.124. Likewise, for the S163 test, an initial effective cell pressure of 300 kPa and an initial state parameter equal to -0.105 were defined. The NorSand parameters used in these simulations are presented in Table 6.3.

Figure 6.10 and Figure 6.11 compare the numerical and experimental results of the simulations. Similar to what was observed for the dense Albian tailings, the simulations with CASM present a stiffer response than that obtained with NorSand and that observed in the laboratory. Once again, the initial stiff response computed by CASM (i.e. before reaching the peak deviatoric stress) is explained by the large initial value of the hardening parameter, which leads to a large size for the yield surface (in other words, a large elastic domain). Note that, in the figure, two different simulations with CASM are depicted. The solid red lines correspond to the simulations performed with the parameters resulting from the calibration. Even though this set of parameters results in a qualitatively good response in terms of stress-strain response, the volumetric strains are underestimated. Therefore, the volumetric strain evolution is not well predicted. This underestimation has been improved by performing a sensitivity analysis for the parameter m and selecting a value that makes the model response closer to the experimental data. These results are depicted in Figure 6.10 and Figure 6.11 with the dotted red lines.

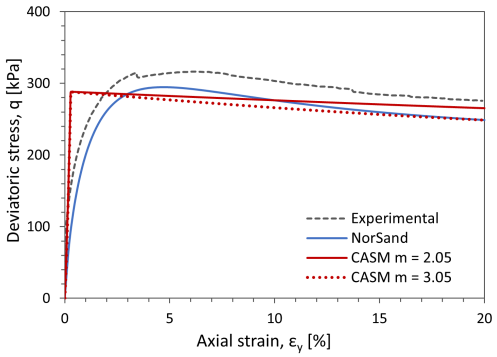

(a) Stress-strain response.

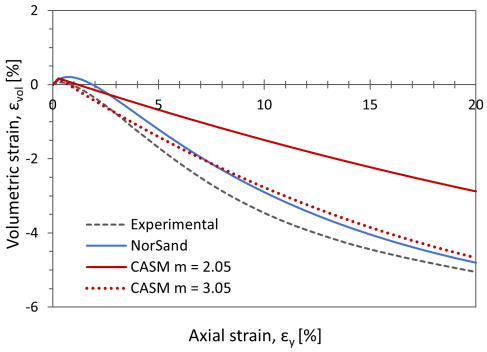

(b) Volumetric strain evolution with vertical strains.

Figure 6.10: Drained monotonic triaxial compression test for the dense sample of Mildred Lake tailings S161.

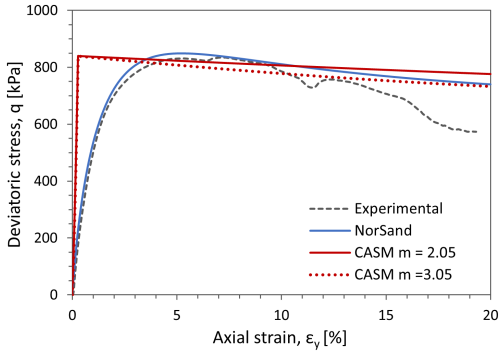

(a) Stress-strain response.

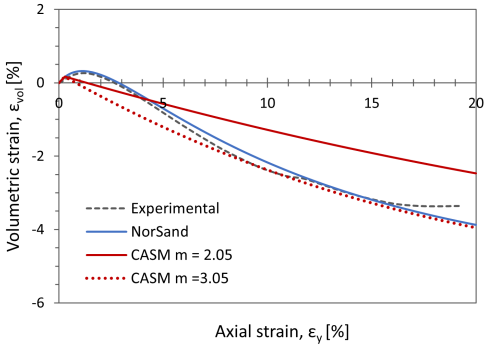

(b) Volumetric strain evolution with vertical strains.

Figure 6.11: Drained monotonic triaxial compression test for the dense sample of Mildred Lake tailings S163.

The calibration of CASM for the Tar Island tailings shows that the model can reproduce the experimental results obtained from tests performed on loose materials. However, for materials characterised by a denser than critical state, it is observed that CASM results in a stiffer stress-strain response until reaching the peak deviatoric stress due to a large elastic domain since it relies on the assumption of a single RCL, therefore treating the material as highly overconsolidated. Nevertheless, since loose materials are generally required for flow liquefaction to occur, and it has been proven that CASM reproduces very well the response of loose Tar Island tailings, CASM can be considered as an appropriate choice for modelling the Tar Island problem.

6.5. Comparison of laboratory test simulations using CASM and NorSand

Tailings derived from beach deposition are usually loose (Vick, 1996) and, therefore, generally modelled as loose or normally consolidated materials in the analysis of tailings dams (Ledesma et al., 2022; Mánica et al., 2022; O'Brien et al., 2021). In fact, Shuttle et al. (2021) performed the numerical analysis of the Tar Island dyke, assuming mainly loose tailings defined by a characteristic state parameter, which was derived from in-situ testing data and the NorSand set of parameters calibrated for the Mildred Lake tailings (Table 6.3).

Since the objective of the present study is to compare the performance of NorSand and CASM when analysing the Tar Island dyke slump, in this subsection, CASM and NorSand are compared at the material point level by simulating different laboratory tests on loose Mildred Lake tailings. This represents a first level of comparison, considering that the model response depends on the boundary conditions directly applied to the single point. At a larger scale, the model response is a function of not only its constitutive laws but also of the complex interaction between the different elements defining the geometry, meaning that a larger number of variables and conditions are involved. Moreover, due to the fact that the experimental laboratory data available for loose Mildred Lake tailings is limited, the comparison was undertaken by considering initial conditions similar to those characterising the Tar Island dyke slump boundary value problem. These conditions consist of an anisotropic consolidation with K_0 equal to 0.6 and an initially looser than the critical state sample with a state parameter of ψ_0 = 0.06.

6.5.1. Monotonic triaxial compression test simulations

Monotonic drained, and undrained triaxial compression tests were simulated using the CASM set of parameters calibrated in the previous subsection (Table 6.2) and the NorSand parameters for the Mildred Lake tailings showed in Table 6.3. Moreover, an initial effective cell pressure, σ'_x, of 100 kPa was applied for these test simulations.

Figure 6.12 compares the results of the monotonic triaxial compression test simulations under drained conditions. In addition to the simulations performed with the mentioned parameters, two simulations with CASM (dotted red line and dashed grey line) have been performed to improve the match with NorSand results. Since the results obtained in the simulation with the CASM set of parameters calibrated (solid red line) present a stiffer response and lower volumetric strains compared with those simulated with NorSand, the elastic domain has been reduced by changing the shape of the yield surface (i.e. changing the value of n) from $n = 7.9$ to $n = 2$ and maintaining the normally consolidated conditions, for which a re-calculation of the parameter $r = 11.9$ to $r = 20.4$ was necessary. As observed, these changes in the parameters n and r result in a softer stress-strain response with larger volumetric strains, which are closer to the stress-strain response and volumetric strains evolution with axial strains obtained with NorSand.

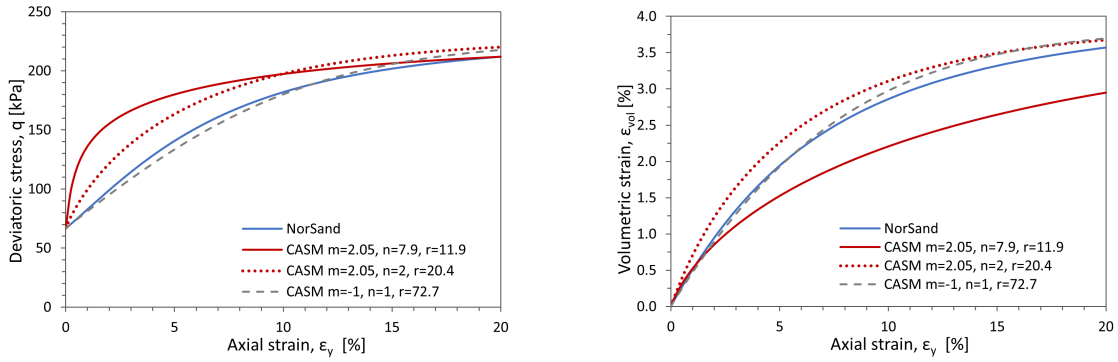

(a) Stress-strain response.

(b) Volumetric strain evolution with vertical strains.

Figure 6.12: Drained monotonic triaxial compression test simulations for a loose sample of Mildred Lake tailings.

Since the implementation of CASM into PLAXIS allows for the definition of the yield surface and plastic potential surface of the Original Cam-clay, which are the surfaces defining NorSand, a set of parameters that employs the OCC surfaces (i.e. $n = 1$ and $m = -1$) was considered as an additional alternative. Moreover, the parameter r was defined so that normally consolidated conditions are considered. As expected, the results of the simulations using this set of parameters (dashed grey line) match very well those obtained with NorSand in terms of both stress-strain and volumetric strain responses as shown in Figure 6.12.

Similar to the drained triaxial test simulations, undrained triaxial tests simulations were performed with the sets of parameters mentioned above and with the same initial conditions (i.e. σ'_x, of 100 kPa, $\psi_0 = 0.06$, and $K_0 = 0.6$). The results of these simulations are presented in Figure 6.13, where it can be noted that the simulation with the set of parameters initially calibrated (solid red line) presents a larger peak deviatoric stress than that obtained with NorSand, while the simulations with the alternative sets of parameters (dotted red line and dashed grey line) result in stress-strain responses and stress paths very close to each other, as well as close to those obtained when using NorSand.

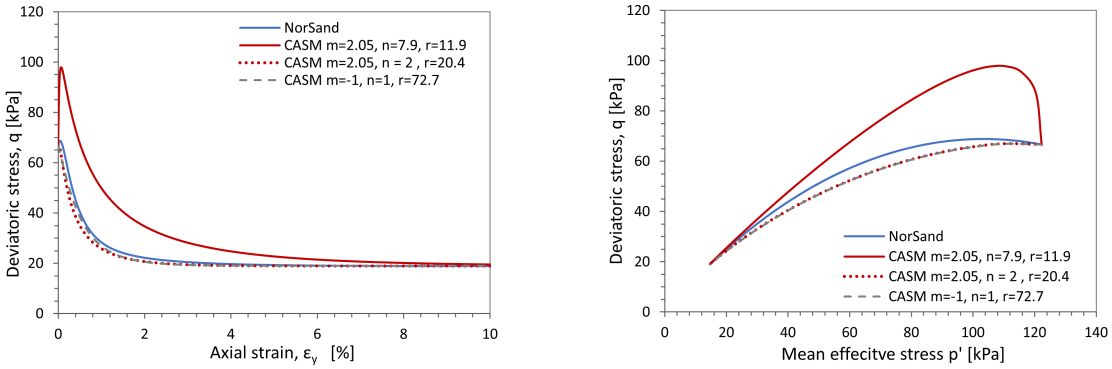

(a) Stress-strain response. **(b)** Effective stress paths.

Figure 6.13: Undrained monotonic triaxial compression test simulations for a loose sample of Mildred Lake tailings.

6.5.2. Direct simple shear test simulations

Direct simple shear tests were simulated under both drained and undrained conditions applying an axial initial effective stress $\sigma'_y = 100$ kPa on samples anisotropically consolidated ($K_0 = 0.6$) and initially looser than the critical state ($\psi_0 = 0.06$). As for the monotonic triaxial compression test simulations, the CASM set of parameters presented in Table 6.2 and the NorSand parameters showed in Table 6.3 for the Mildred Lake tailings together with the set of parameters proposed as alternatives were used in the simulations.

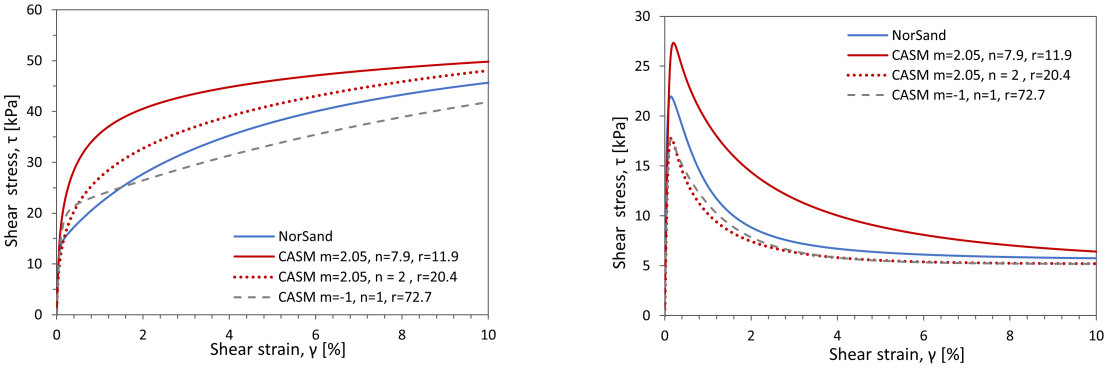

(a) Stress-strain response under drained conditions. **(b)** Stress-strain response under undrained conditions.

Figure 6.14: Direct simple shear test simulations for a loose sample of Mildred Lake tailings.

The DSS test simulation results are presented in Figure 6.14, where it can be noted that the results obtained using the CASM parameters estimated in Section 5.3. (solid red line) present larger shear stresses than those obtained using NorSand under drained and undrained conditions. Nevertheless, these differences are reduced with the alternative CASM set of parameters. Specifically, when the parameters used are $n = 2$ and $r = 20.4$ under drained conditions, a softer shear stress-strain response is observed, as well as a lower peak undrained shear stress. When the CASM set of parameters uses the same yield surface and plastic potential as NorSand (dashed grey line), it is obtained lower shear stresses under drained and undrained conditions.

6.5.3. Oedometer test simulations

Oedometer tests were simulated using the CASM and NorSand set of parameters for the Mildred Lake tailings. For these simulations, loose samples defined by $\psi_0 = 0.06$ were considered, and the axial stresses were applied in stages until reaching a maximum value of 3000 kPa. The results of these simulations are presented in Figure 6.15.

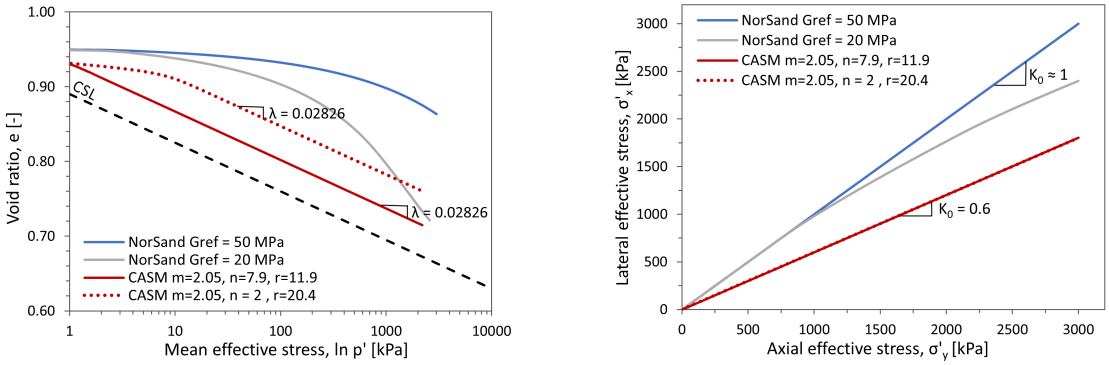

(a) Void ratio evolution with mean effective stress.

(b) Effective stress path in terms of axial and lateral stresses.

Figure 6.15: Oedometer test simulations performed on Mildred Lake tailings samples.

Given that CASM assumes the parameter λ to be the slope of the reference consolidation line (RCL), and since the set of parameters corresponds to a normally consolidated material, it can be observed that the response obtained in terms of void ratio and mean effective stress follows the consolidation line with the slope $\lambda = 0.02826$ (input parameter). Note that the effect of the parameter r (distance between the RCL and CSL) is also observed in the ($\ln p'$, e) space with the larger distance for the simulation performed with $r = 20.4$. Moreover, in terms of axial and lateral effective stresses, the response denotes a K_0 equal to 0.6, which was the value assumed during the calibration of the parameter m.

For the simulations performed using NorSand, two different plots can be identified, for which the same set of parameters was used with a different value of G_{ref}. This was carried out to illustrate the effect of this parameter on the results. Compared with the simulations performed using CASM, both NorSand simulations show initially stiffer responses with the trends not following the λ slope. This can be explained since NorSand considers λ as the slope of the CSL but not of the normal consolidation line (NCL). Furthermore, contrary to the results obtained with CASM, the computed K_0 during the simulations are much higher than the expected value of $K_0 = 0.6$. More specifically, when using $G_{ref} =$ 50 MPa, the value of K_0 is around 1, which is an unrealistic value under one-dimensional consolidation test conditions. The decrease of the parameter G_{ref} shows a significant effect on the results in terms of the K_0 computed, as well as in terms of the void ratio evolution.

7

CASM and NorSand comparison in boundary value problems

7.1. Introduction

The design and analysis of geotechnical structures are often carried out using finite element methods. The quality of the results depends on several aspects of the analysis, such as the boundary conditions, the discretisation of the domain, the constitutive models and sets of parameters used for the materials, the ability of the software to capture the coupled phenomena, etc. Among these aspects, it is important to highlight the key role of the constitutive models, which should be able to reproduce the mechanical behaviour of the materials with a satisfactory degree of accuracy.

CASM and NorSand are constitutive soil models often considered as alternatives in the analysis of flow liquefaction. In fact, it has been shown that both models can reproduce this phenomenon successfully (Arroyo & Gens, 2021; Mánica et al., 2022; Shuttle et al., 2021; Zheng et al., 2022). Having already calibrated CASM and NorSand for the Mildred Lake tailings, the abilities of these constitutive models are explored in this chapter in the context of boundary value problems involving these materials. More specifically, these constitutive models are firstly applied to the simulation of an embankment construction with a simple geometry to gain some fundamental insight into their main abilities and differences. Subsequently, both models are applied to the simulation of the well-known Tar Island failure, referring to Shuttle et al. (2021) in the case of NorSand.

7.2. Embankment model

The first boundary value problem analysed corresponds to the simulation of the embankment construction already described in Section 4.2.3. Three different analyses were performed: drained, undrained and consolidation. The boundary conditions and geometry are depicted in Figure 7.1. The embankment fill is idealised as a linear elastic material, while the 'in situ' soil deposit is defined as loose Mildred Lake tailings modelled with both CASM and NorSand.

The CASM parameters were already calibrated in Chapter 6, while the NorSand parameters correspond to those reported in Shuttle et al. (2021) for the same tailings. Table 7.1 and Table 7.2 present the values of these model parameters. The initial state of the tailings were characterised by the initial state parameter $\psi_0 = 0.06$.

Table 7.1: CASM parameters for the Mildred Lake tailings.

Parameters	λ	κ	ν	ϕ_{cs}	Γ	n	r	m	ψ_0
Values	0.02826	0.004	0.2	32.06°	1.89	2	20.4	2.05	0.06

Table 7.2: NorSand parameters for the Mildred Lake tailings (Shuttle et al., 2021).

Parameters	G_{ref}	p'_{ref}	n_G	ν	Γ	λ_e	M_{tc}	N	χ_{tc}	H_0	H_ψ	R	S	ψ_0
Values	50 MPa	100 kPa	0.5	0.2	0.890	0.02826	1.29	0.45	4.1	70	775	1	0	0.06

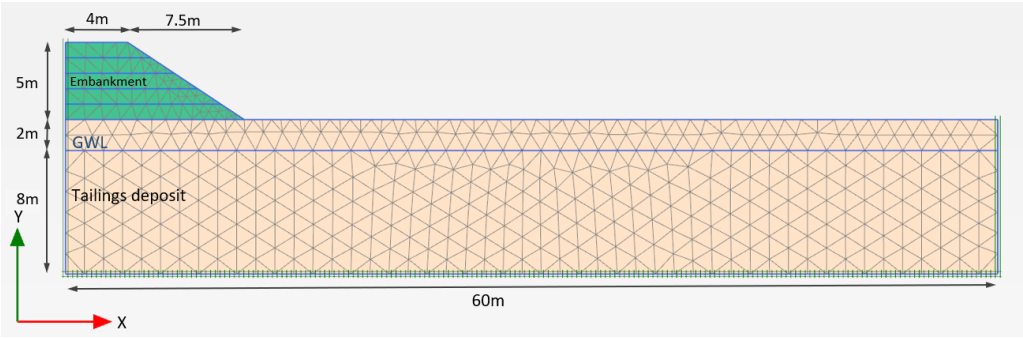

Figure 7.1: Boundary conditions and geometry of the embankment construction simulation.

7.2.1. Drained analysis

For the drained analysis, six phases were defined in PLAXIS to simulate a staged construction of the embankment. The first (plastic) phase was defined to compute the initial stress state and the next five phases correspond to the construction of each 1 m embankment layer. The results of the simulations with both constitutive models in terms of total displacements at the end of the simulations are shown in Figure 7.2.

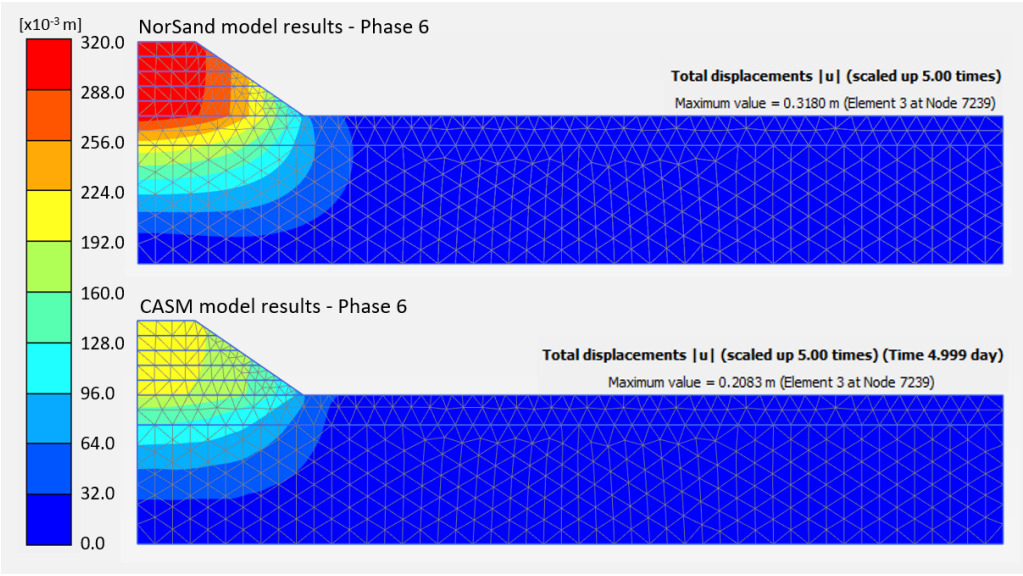

Figure 7.2: Total displacements results for the drained analysis at the end of the simulations.

It can be observed that the simulation performed with NorSand computed larger total displacements at the end of the embankment construction. These differences are observed during all the simulation phases. In Figure 7.3, it is show that slightly larger values of total displacements are accumulated in the case of the NorSand deposit, already during the first loading stage (Phase 2). Moreover, Figure 7.4 and Figure 7.5 show considerable differences in terms of both mean effective stresses and deviatoric stresses at the end of phase 2. In the case of NorSand, larger mean effective stresses and lower deviatoric stress (close to zero) are obtained in the area just below the embankment, with respect to those obtained with CASM, likely as a consequence of the different effective stress distributions obtained as the load is applied. The small deviatoric stresses developed below the embankment in the simulation using

NorSand resemble what was observed in the oedometer test simulation using this constitutive model. In principle, when the embankment is raised, one-dimensional consolidation conditions can be found in the area underneath the embankment, particularly along the axis of symmetry of the problem.

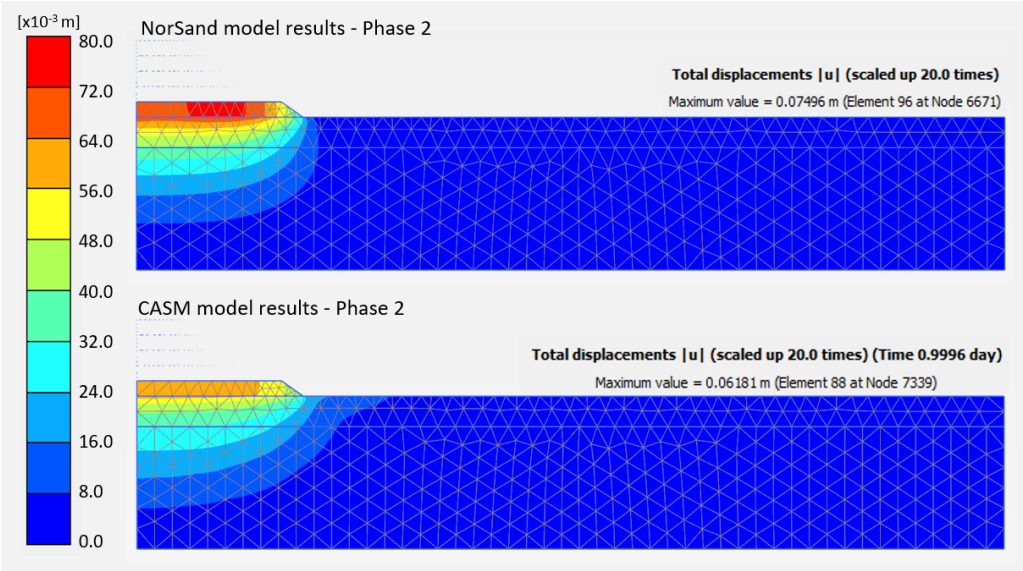

Figure 7.3: Total displacements results for the drained analysis at the end of phase 2.

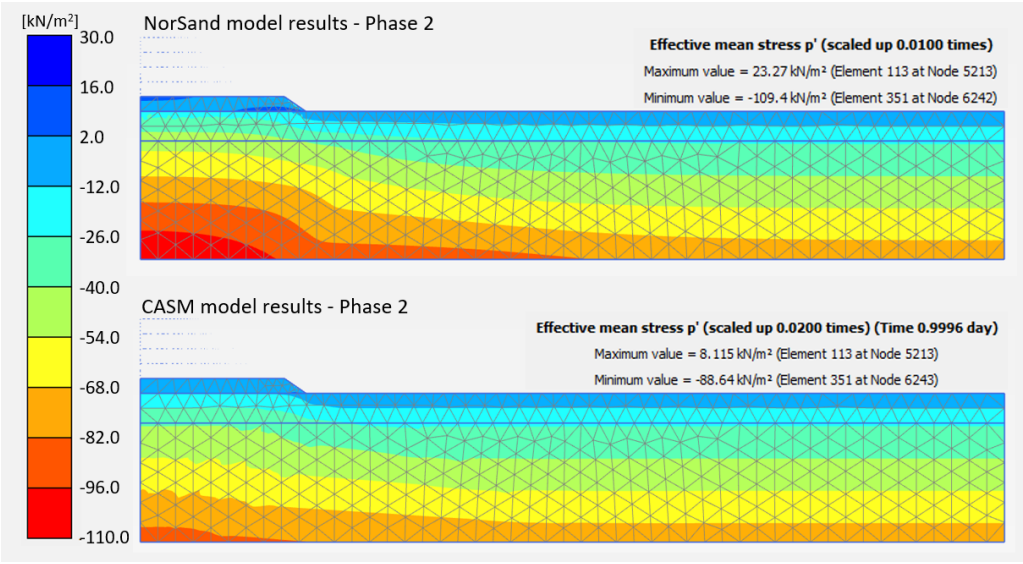

Figure 7.4: Results for the simulations at the end of phase 2 in terms of mean effective stresses.

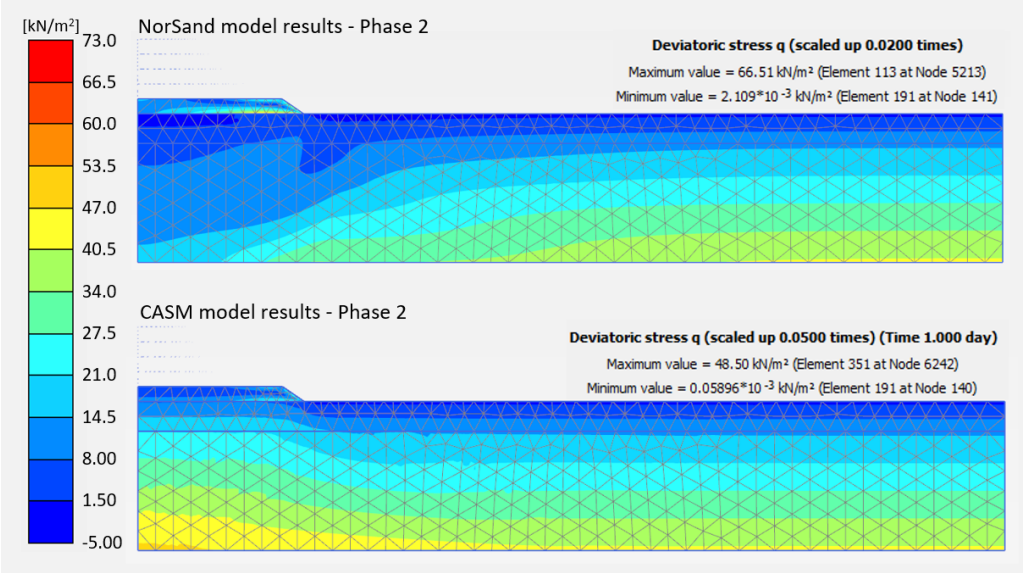

Figure 7.5: Results for the simulations at the end of phase 2 in terms of deviatoric stresses.

The horizontal and vertical effective stress distributions are shown in Figure 7.6 and Figure 7.8. A significant difference of about 30 kPa can be seen in terms of horizontal effective stresses. In addition to the one-dimensional consolidation conditions explained before, this difference may be the result of the different plastic potential surfaces used by the models, which lead to different plastic strain components, as illustrated in Figure 7.7, where the vertical and horizontal strains are plotted for two stress points located in the tailings deposit (Figure 7.7a), and it can be observed a considerable difference in the magnitude of the strains computed (Figure 7.7b). Finally, the vertical effective stresses present very similar trends since the same vertical load was imposed in both analyses, corresponding to the construction of the embankment (Figure 7.8).

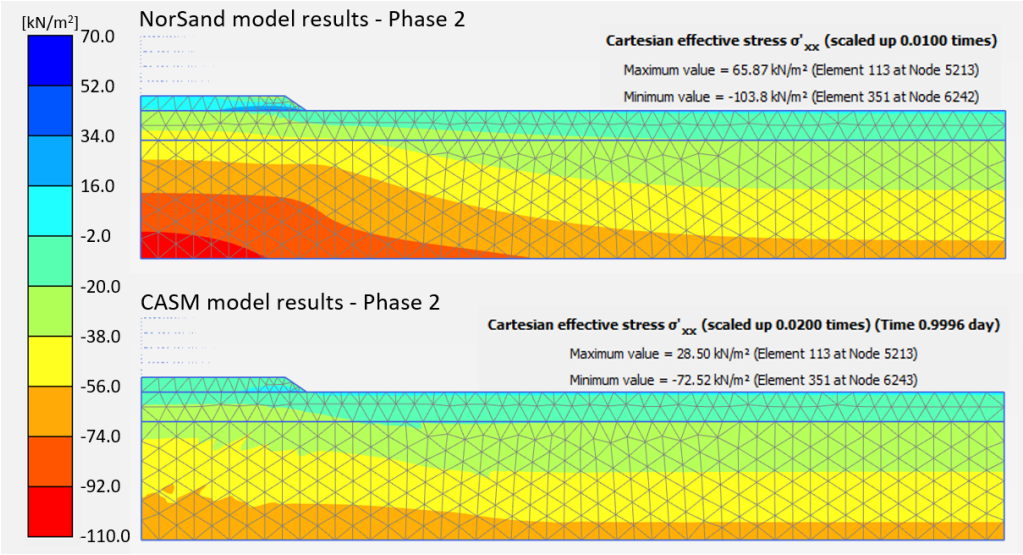

Figure 7.6: Results for the simulations at the end of phase 2 in terms of horizontal effective stresses.

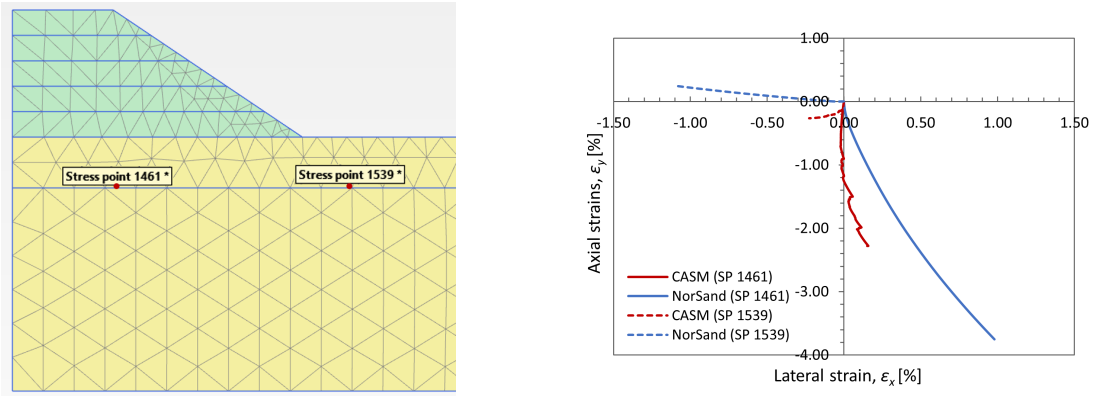

(a) Stress points pre-selected.

(b) Axial strain evolution with lateral strain.

Figure 7.7: Strain results for two different stress points using NorSand and CASM.

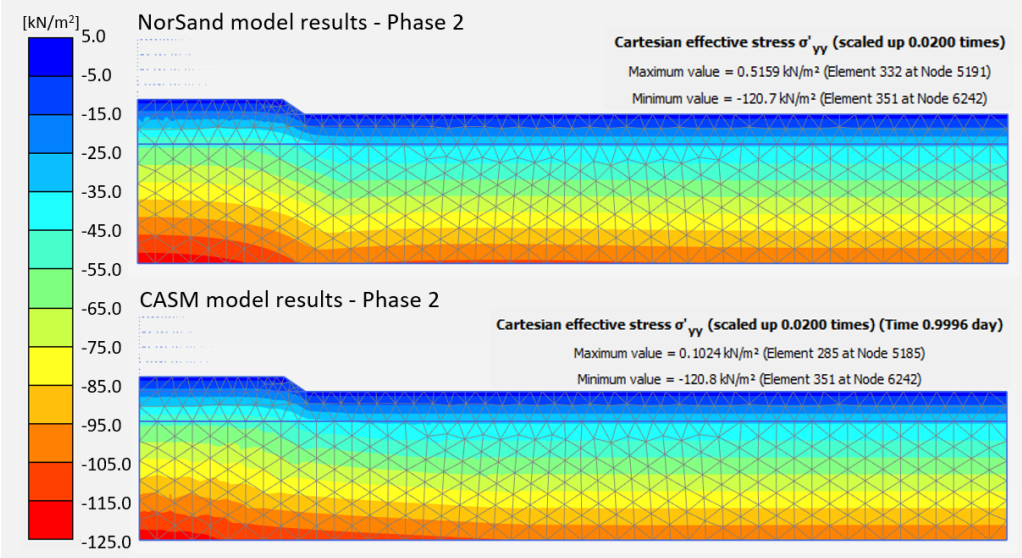

Figure 7.8: Results for the simulations at the end of phase 2 in terms of vertical effective stresses.

7.2.2. Undrained analysis

The undrained analysis was performed defining a single 2 m-thick layer. The results at the end of the simulations (i.e. when failure is reached) are shown in Figure 7.9a and 7.9b for NorSand and CASM, respectively. It can be observed that larger excess pore pressures are obtained when using NorSand. Note, however, that the results obtained with NorSand correspond to a greater value of ΣMstage, meaning that a greater portion of load (i.e. weight of the embankment material) was activated in that case. To compare the results for a similar load activation, the excess pore pressure developed in the NorSand simulation at the same value of ΣMstage reached at failure with CASM (ΣMstage = 0.315) is shown in Figure 7.9c. It can be observed that, for the same load, lower excess pore pressures are developed with NorSand in this boundary value problem.

Figure 7.10 shows the incremental deviatoric strains obtained at failure for both NorSand and CASM simulations and at an intermediate stage of the simulation for NorSand (ΣMstage = 0.315). The larger incremental deviatoric strains are observed at the toe of the embankment, with a softer response obtained when using CASM. Note that at ΣMstage = 0.135 the response of the simulation with NorSand is characterised by small incremental deviatoric strains (Figure 7.10c).

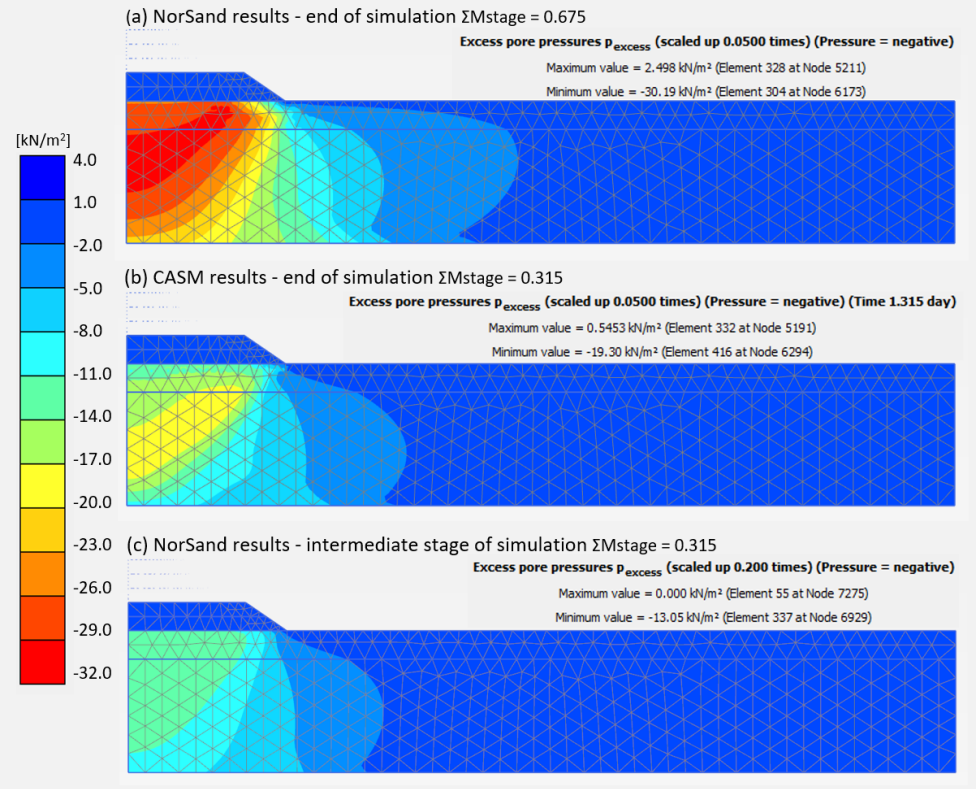

Figure 7.9: Excess pore pressures developed in the undrained simulation of an embankment construction with NorSand and CASM

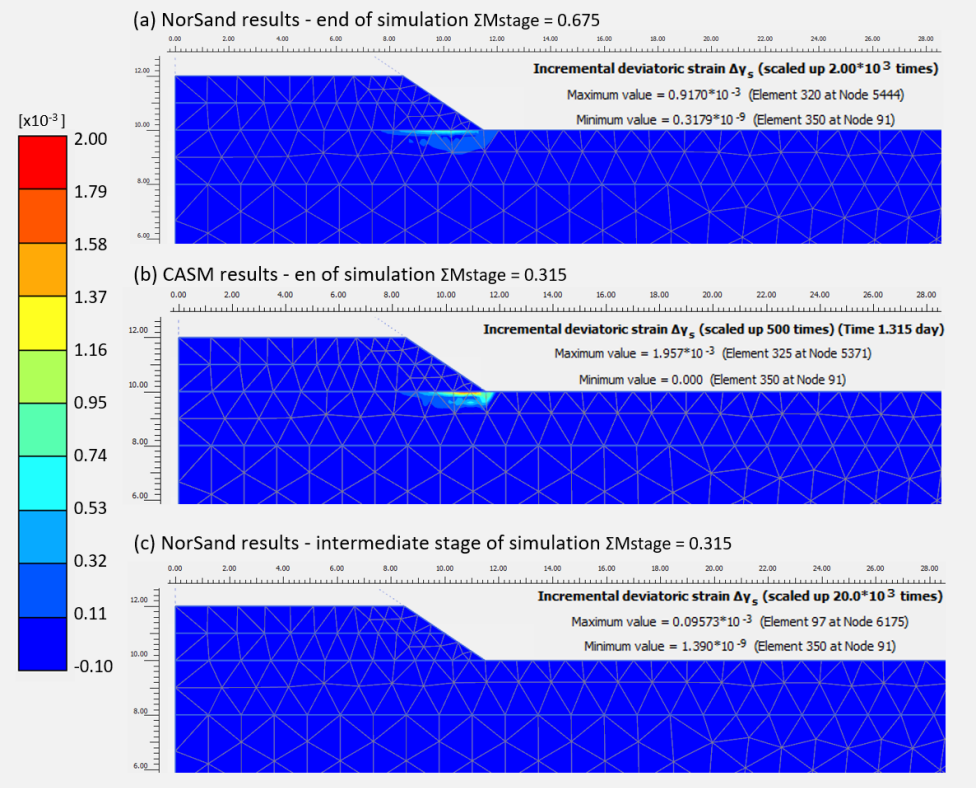

Figure 7.10: Incremental deviatoric strains developed in the undrained simulation of an embankment construction with NorSand and CASM.

7.2.3. Consolidation analysis

Similar to the drained analysis, for the consolidation analysis, five phases were defined to simulate the staged construction of the embankment. Moreover, a duration of 20 days was chosen for each phase, and a hydraulic conductivity of 1E-06 m/s was assumed for the tailings deposit. The results of the simulations after 100 days in terms of total displacements and excess pore pressures are presented in Figure 7.11 and Figure 7.12, respectively.

Similar to the drained analysis results, it can be observed that larger total displacements are computed with NorSand. In fact, the values of displacements obtained during the consolidation analysis are practically the same as those obtained in the fully drained analysis (Figure 7.2). This can also be observed in terms of excess pore pressures since the computed values are small, indicating that the time defined for each phase was enough to dissipate most of the excess pore pressures. Therefore, the results of these consolidation analyses can be considered as practically drained.

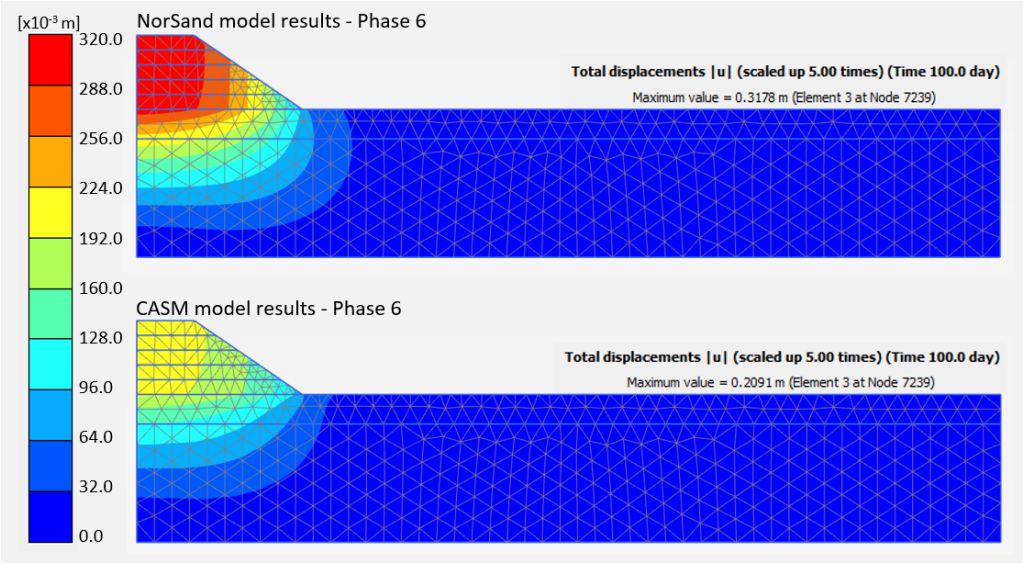

Figure 7.11: Total displacements at the end of the consolidation analysis.

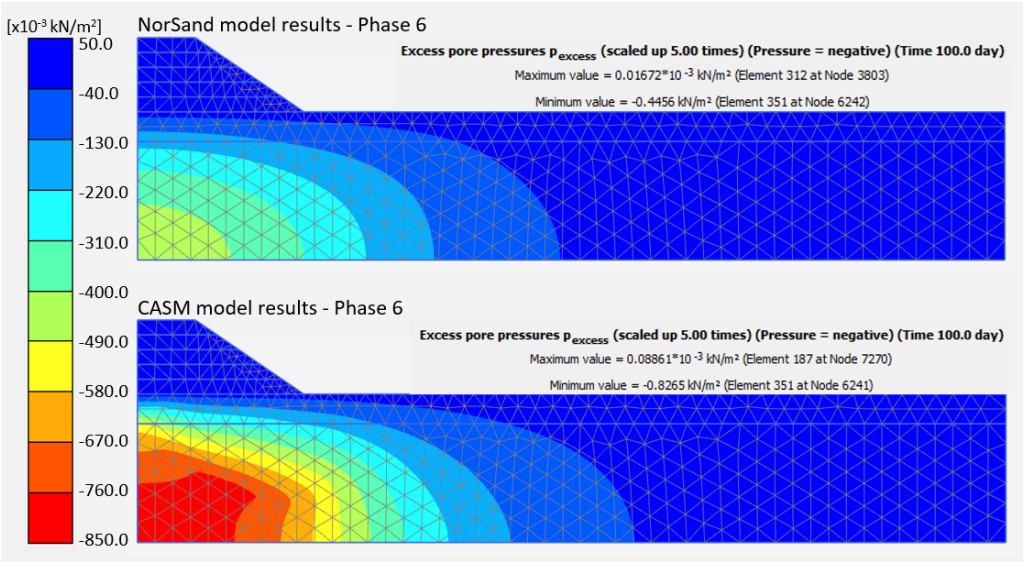

Figure 7.12: Excess pore pressures at the end of the consolidation analysis.

Figure 7.13 compares the maximum total displacement obtained at the end of each construction phase in both analyses. It can be observed that larger displacements are obtained when using NorSand, with a difference between them of about one-third of the larger total displacement. These considerable differences at each phase can be explained due to the combination of the differences between the models. CASM and NorSand use different yield surfaces and plastic potential surfaces, which, together with the different hardening rules, result in different plastic strains computed, leading to different displacements.

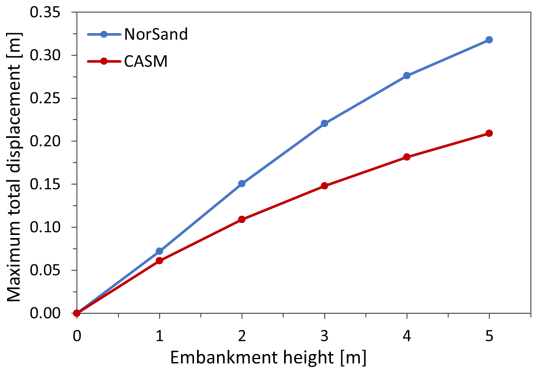

Figure 7.13: Maximum total displacements for each embankment raise.

7.3. Tar Island Dyke model

The flow liquefaction event that occurred in the Tar Island Dyke in August 1974, already described in Chapter 5, was simulated in this section using CASM, with the results being compared against those obtained when using NorSand (Shuttle et al., 2021).

7.3.1. General aspects

In general, the same criteria and assumptions adopted by Shuttle et al. (2021) were followed in the analysis performed with CASM, as described in detail in the next lines.

Model configuration and material properties

The model size was defined considering the failure mechanism observed in reality (Shuttle et al., 2021). As such, only the upstream zone of the dyke was defined as part of the domain as illustrated in Figure 7.14. Moreover, the upstream domain was extended by more than 430 m from the toe of the compacted cell (to the left-hand side) to ensure that the failure mechanism was not affected by the boundary constraints.

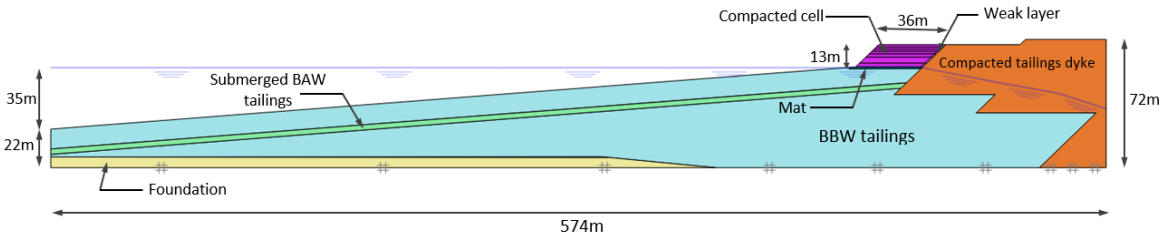

Figure 7.14: Tar Island Dyke model.

Different components of the dam (i.e. dyke, compacted cell, foundation, etc.) were defined in the model. The Mohr-Coulomb model under drained conditions was used to model the response of the compacted tailings sands of the dyke, the foundation, and the compacted cell. Moreover, the influence of a tension crack was taken into account by including a weak layer in between the compacted cell and the dyke (Figure 7.14). The material properties used for these components are presented in Table 7.3.

Table 7.3: Material properties and Mohr-Coulomb parameters for the model components, as reported in Shuttle et al. (2021).

Component	γ_{unsat} [kN/m^3]	γ_{sat} [kN/m^3]	E_{ref} [MPa]	ν	$c'ref$ [kPa]	ϕ' [°]	ψ [°]
Compacted tailings dyke	18.6	19.6	80	0.2	5	48	0
Compacted cell	18.6	19.6	80	0.2	5	48	0
Weak layer	18.6	19.6	80	0.2	2	5	0
Foundation	20	22	144	0.2	1000	50	0

Both uncompacted tailings, referred to as BBW (Beach Below Water), and dense tailings, indicated as BAW (Beach Above Water), were modelled using the constitutive models studied in this research (i.e. NorSand and CASM). The dense tailings observed in the CPT data were modelled as a 3 m thick layer parallel to the surface of the tailings. Table 7.4 presents the unit weight of soil of both tailings. The model parameters used are those calibrated for the Mildred Lake tailings, shown in Table 7.1 and Table 7.2 (Chapter 6). The only difference between the BAW and BBW set of parameters is the value assigned to the initial state parameter, ψ_0, equal to 0.06 for BBW and -0.02 for BAW.

Table 7.4: Unit weights for the BBW and BAW tailings.

Tailings	γ_{unsat}	γ_{sat}
BBW	16.8 kN/m^3	18.8 kN/m^3
BAW	17.1 kN/m^3	19.1 kN/m^3

The last material to be described is a mat, on top of which the compacted cell was deposited. Shuttle et al. (2021) assume this mat consists of a 1 m thick layer of the denser upper material identified in the CPTs (Figure 5.5). Therefore, this mat was considered as BAW tailings with ψ = -0.10.

Groundwater conditions

Based on the CPT data, a hydrostatic pore pressure profile is considered below the pond level, as depicted in Figure 7.14. Moreover, as reported by Shuttle et al. (2021), the water table falls within the dyke due to the downstream drainage system.

Geostatic stress initialisation

The initial stress state was generated using a 'K_0' procedure, which requires the definition of the earth pressure coefficient at rest, K_0. Unfortunately, no K_0 information from the site was reported. However, Shuttle et al. (2023) estimated $K_0 = 0.6$ from self-bored pressuremeter (SBP) data for normally consolidated oil-sand tailings, and this value was used in the model.

Model drainage conditions

As already described in Chapter 5, the compacted cell was constructed in 5 lifting stages, with the failure occurring after the last lift. This aspect was simulated by considering a phased loading. For the first four lifting stages, drained conditions were assumed for the BBW and submerged BAW tailings and the last stage was divided into two distinct phases, with the first one (lower half of the layer) being considered to occur in drained conditions, while undrained conditions were imposed during the subsequent phase to simulate the occurrence of rapid loading and slower than expected dissipation of construction-induced pore pressures caused by residual hydrocarbon traces identified in the tailing materials, which affected their porosity (Shuttle et al., 2021).

Mesh

In terms of element type and mesh, 15-node triangular elements were used in the present simulation with smaller elements being adopted in the zones of the model where larger strains are expected (i.e. below the tailings cell where liquefaction will develop). A coarser mesh is adopted in the zones of the model where smaller strains are likely to develop (i.e. compacted dyke and zones far from failure). Figure 7.15 illustrates the mesh adopted in the present analysis.

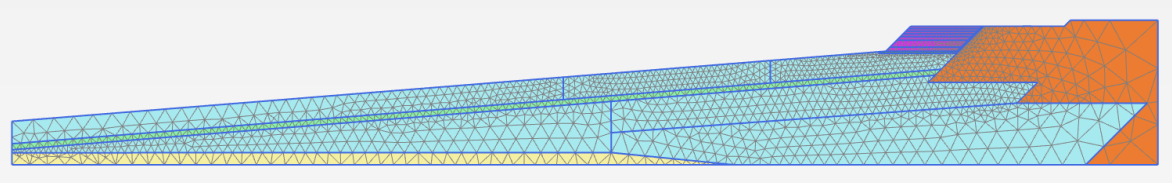

Figure 7.15: Mesh adopted for the simulation of the Tar Island Dyke problem.

7.3.2. Model scenarios

Two different scenarios were considered to be modelled. The first scenario was modelled assuming the existence of a continuous BAW stratum as described above (Figure 7.14), while a single BBW tailings material was considered for the second scenario (i.e. inexistence of BAW stratum). As reported by Shuttle et al. (2021), this latter scenario led to the closest match between the numerical results and those observed in the field in terms of settlement and upstream soil movement.

7.3.3. Obtained results

In what follows, the results obtained for the two scenarios when using CASM are presented in terms of excess pore pressures, state parameters and total displacements. The incremental deviatoric strains retrieved at different moments (i.e. different values of ΣMstage) of the last phase of each simulation to show the development of the failure mechanism are also depicted. Moreover, the results for Scenario 2 computed with CASM and NorSand are compared.

Flow liquefaction is often evaluated using the critical state soil mechanics theory and the state parameter, ψ, framework. Under undrained shearing conditions, a loose material characterised by a positive state parameter experiences a continuous increase of excess pore pressures until reaching critical state conditions (i.e. until the state parameter becomes zero). In this section, flow liquefaction is assessed based on the results obtained in terms of excess pore pressures and state parameters assuming that liquefaction starts when a build-up of excess pore pressures occurs, and the state parameter of the tailings approaches zero.

Scenario 1

Figure 7.16 shows the contours of the excess pore pressures computed at the end of the simulation. It can be observed that during the undrained loading, large excess pore pressures of about 200 to 300 kPa build-up, especially underneath the compacted cell and along a deeper plane that is apparently formed from the weak layer.

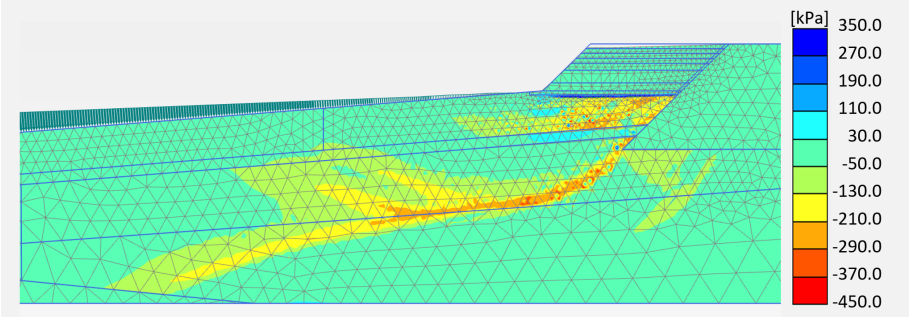

Figure 7.16: Excess pore pressures at the end of the simulation for Scenario 1.

Figure 7.17 shows state parameter contours for the tailing materials. At the start of the undrained loading (Figure 7.17a), it can be observed that the values of the state parameter for the tailings are not far from that defined as input ($\psi_0 = 0.06$). Conversely, at the end of the simulation (Figure 7.21b), the tailings deposited below the compacted cell reach values of state parameters close to zero. These results, together with those described above regarding the excess pore pressures, suggest that the model failure occurs due to flow liquefaction.

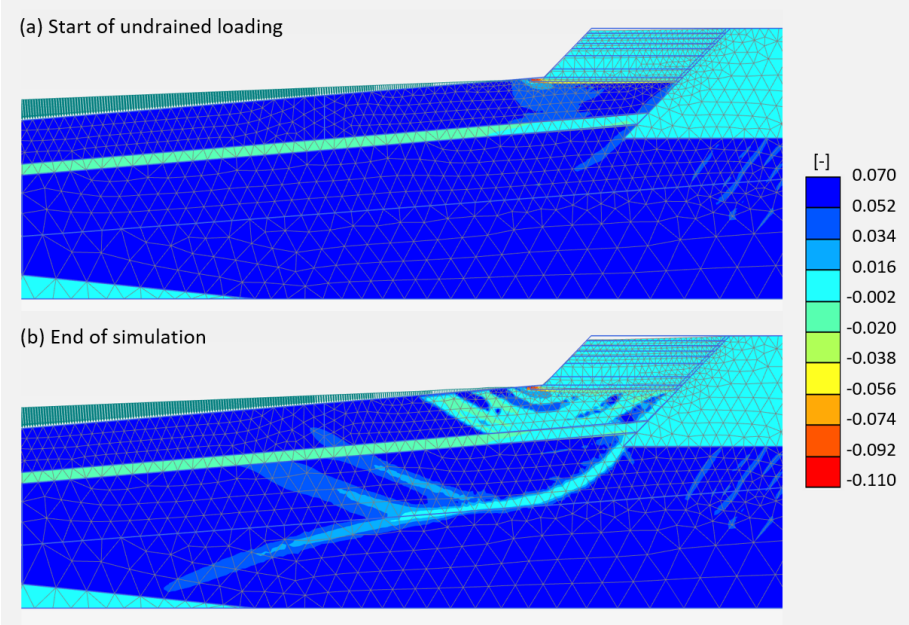

Figure 7.17: State parameter contours for different undrained loading moments for Scenario 1.

The results of the simulation in terms of incremental displacements and total displacements are presented in Figure 7.18a and Figure 7.18b, respectively. As reported in Plewes et al. (1989) the figures suggest that the whole compacted cell was affected during the flow failure (i.e. it is part of the moving mass). The maximum total displacement computed at the end of the simulation is 1.17 m. Moreover, from the incremental displacements plot, it can be observed that the length affected by the failure mechanism spreads approximately 160 m from the upstream dyke crest.

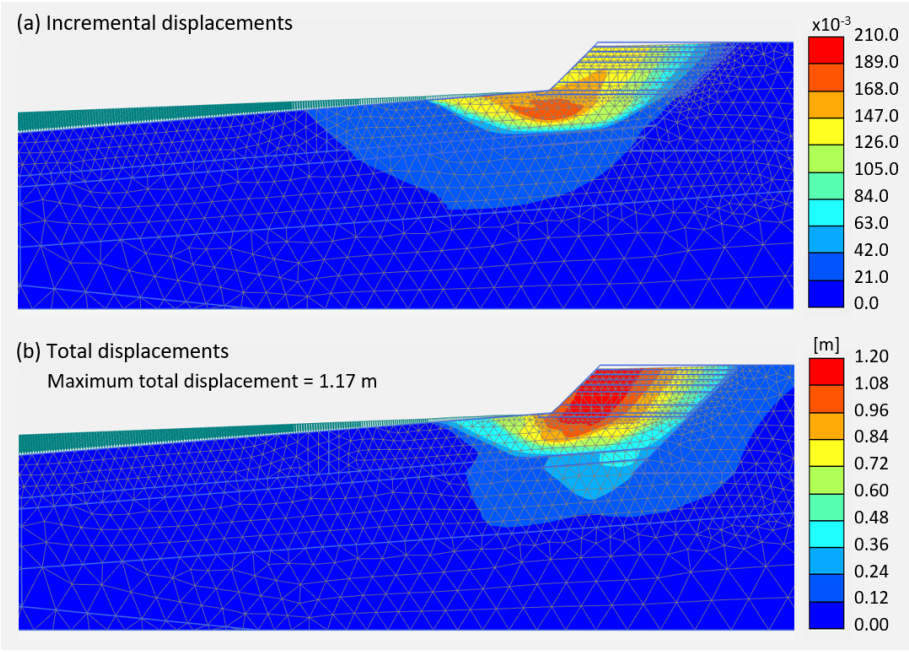

Figure 7.18: Incremental displacements and total displacements at the end of simulation of Scenario 1.

Figure 7.19 shows the incremental shear strains at different moments of the last compacted cell raise. In Figure 7.19a, it can be observed little incremental deviatoric strains at the start of the last lift, mostly located along the weak layer between the compacted cell and the dyke. Figure 7.19b shows the strains at the start of liquefaction, which occurred when 0.35 m of the second half of the last lift

was loaded. At this stage, it is observed that the incremental deviatoric strains are localised beneath the toe of the compacted cell and along the weak layer. Finally, 7.19c and 7.19d show the incremental deviatoric strains during the propagation of flow liquefaction and at the end of the simulation. In these last figures, it can be observed that the strains along the weak layer reach greater depths and lengths without forming a complete failure mechanism.

Taking as a reference the toe of the compacted cell, the failure mechanism extends around 30 m to the upstream direction and to a depth of about 11 m. The vertical evolution of the failure mechanism is apparently constrained by the presence of the submerged BAW tailings, which are denser than the BBW tailings.

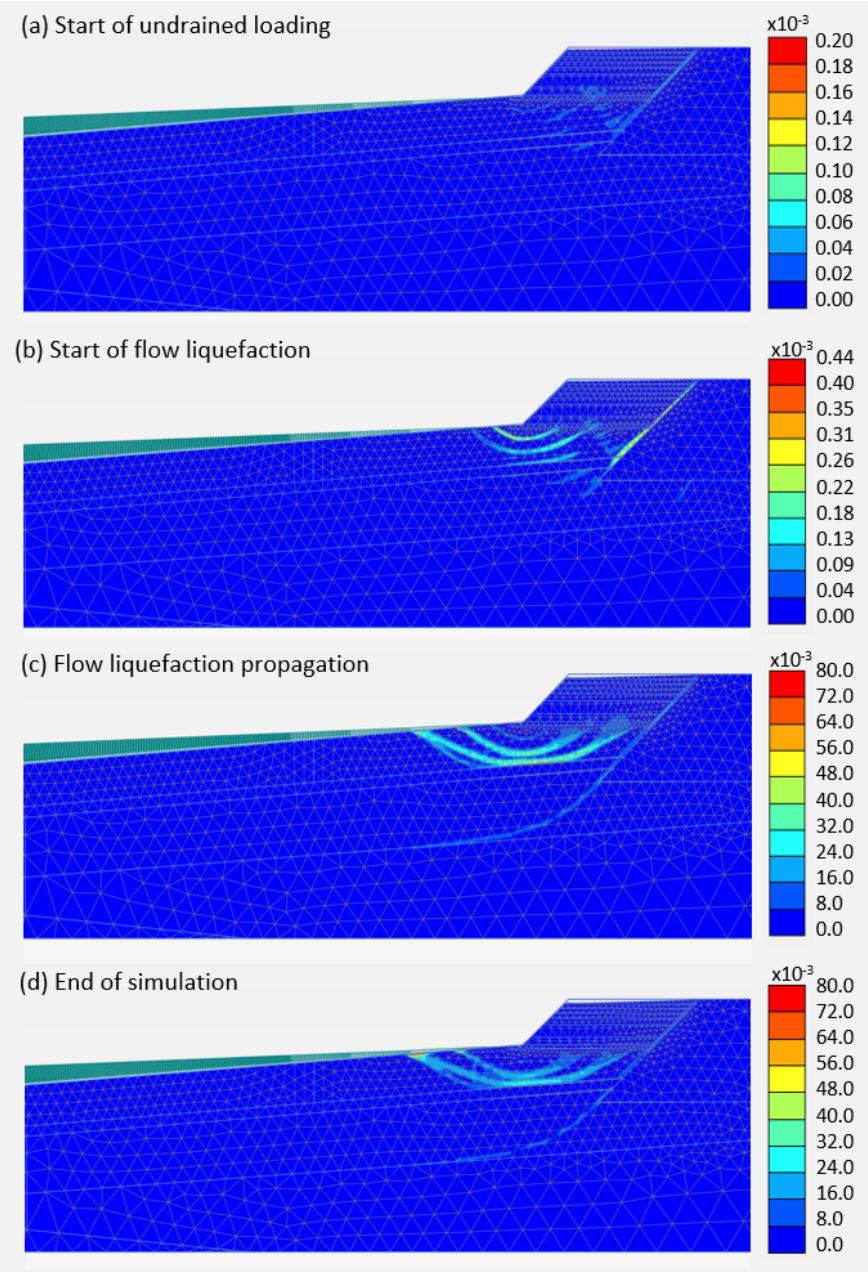

Figure 7.19: Incremental deviatoric strains for different moments of loading for Scenario 1.

Scenario 2

Figure 7.20 depicts the excess pore pressures computed at the end of the simulation for Scenario 2. Similar to the results for Scenario 1, build-up of the excess pore pressures is observed underneath the compacted cell.

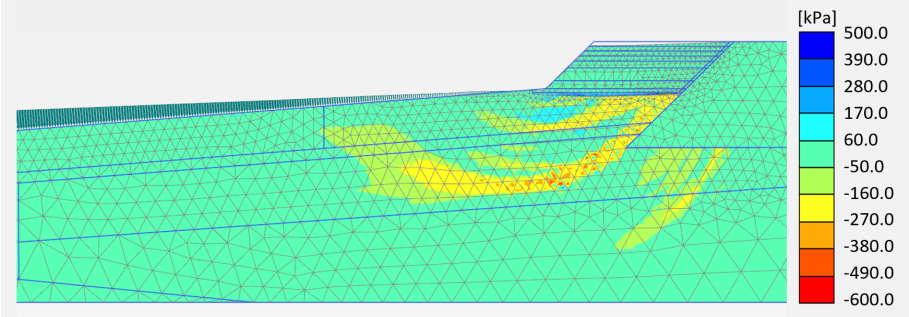

Figure 7.20: Excess pore pressures at the end of the simulation for Scenario 2.

Figure 7.21 shows the state parameter computed for the tailing materials at the start of the undrained loading (Figure 7.21a) and at the end of the simulation (Figure 7.21b). Similar to the results obtained for Scenario 1, it can be noted that during the undrained loading, the state parameters of the tailings below the compacted cell are practically zero, suggesting that these materials reach critical state conditions and denote a failure mechanism.

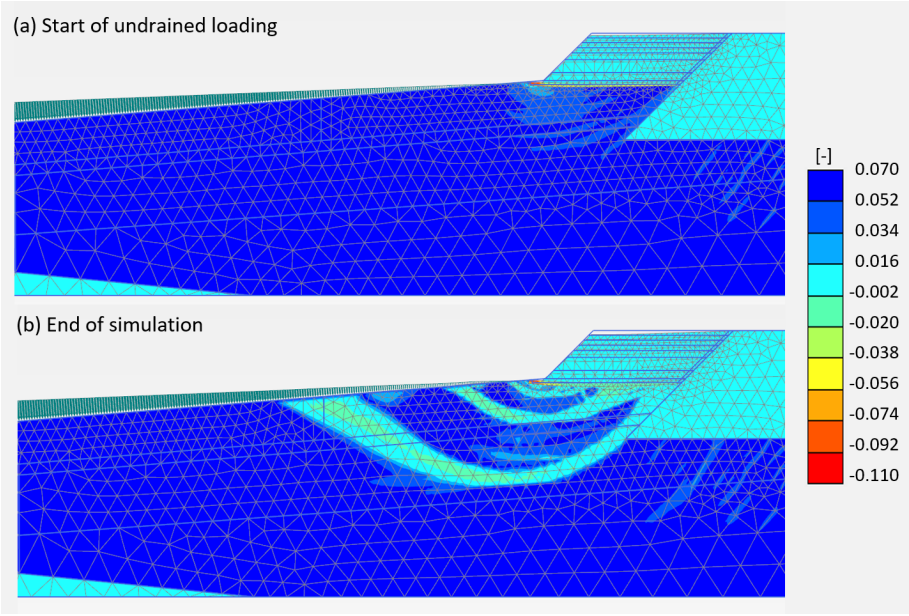

Figure 7.21: State parameter contours for different undrained loading moments for Scenario 2.

Figure 7.22 shows the incremental displacements and total displacements at the end of the simulation (i.e. at failure). Similar to Scenario 1, it can be observed that the whole compacted cell is within the sliding mass. Moreover, in this case, a total displacement equal to 1.25 m is obtained at the end of the simulation, which is slightly greater than that obtained for Scenario 1 (about 1.17 m).

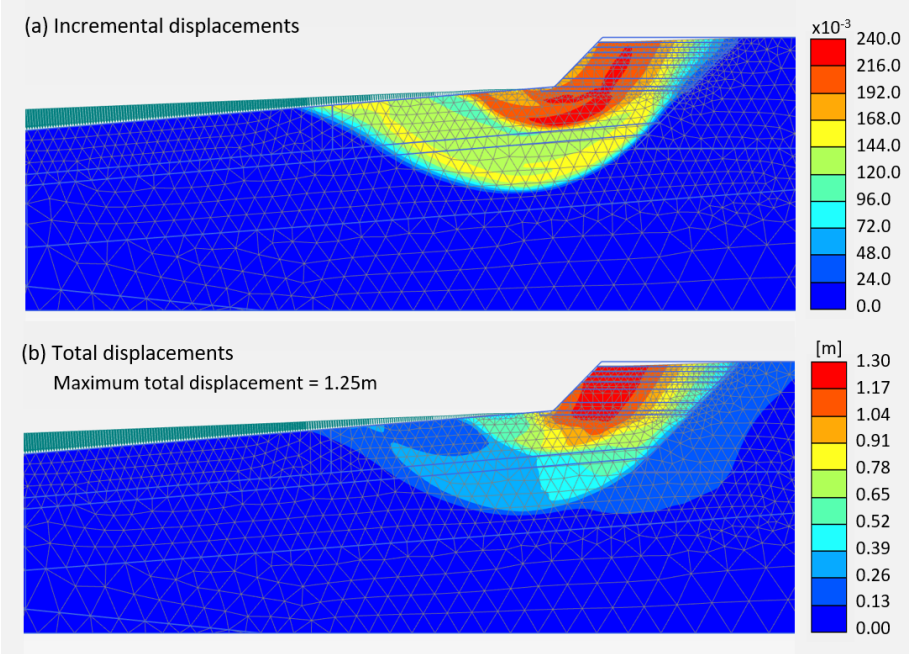

Figure 7.22: Incremental displacements and total displacements at the end of simulation of Scenario 2.

Figure 7.23 shows the obtained results for Scenario 2 in terms of incremental deviatoric strains at different moments of the undrained loading phase, which give an indication of the deformation mechanism developed during that phase. It can be observed that the deformation mechanism has a similar shape to that developed in Scenario 1, with the incremental deviatoric strains developing along the weak layer and under the compacted cell in the loose 'in situ' BBW tailing deposit. It should be noted, however, that the amount of activated undrained loading that triggered the failure for Scenario 2 (ΣMstag = 0.251) is slightly smaller than that obtained for Scenario 1 (ΣMstage = 0.295). Moreover, some differences can be observed in terms of the volume of the sliding mass. In effect, Figure 7.23d shows a deeper and wider failure mechanism extending about 30 m deep and 70 m in length from the toe of the compacted cell was obtained in this scenario, due to the absence of the thin submerged BAW tailing layer, which is denser than the BBW tailing deposit.

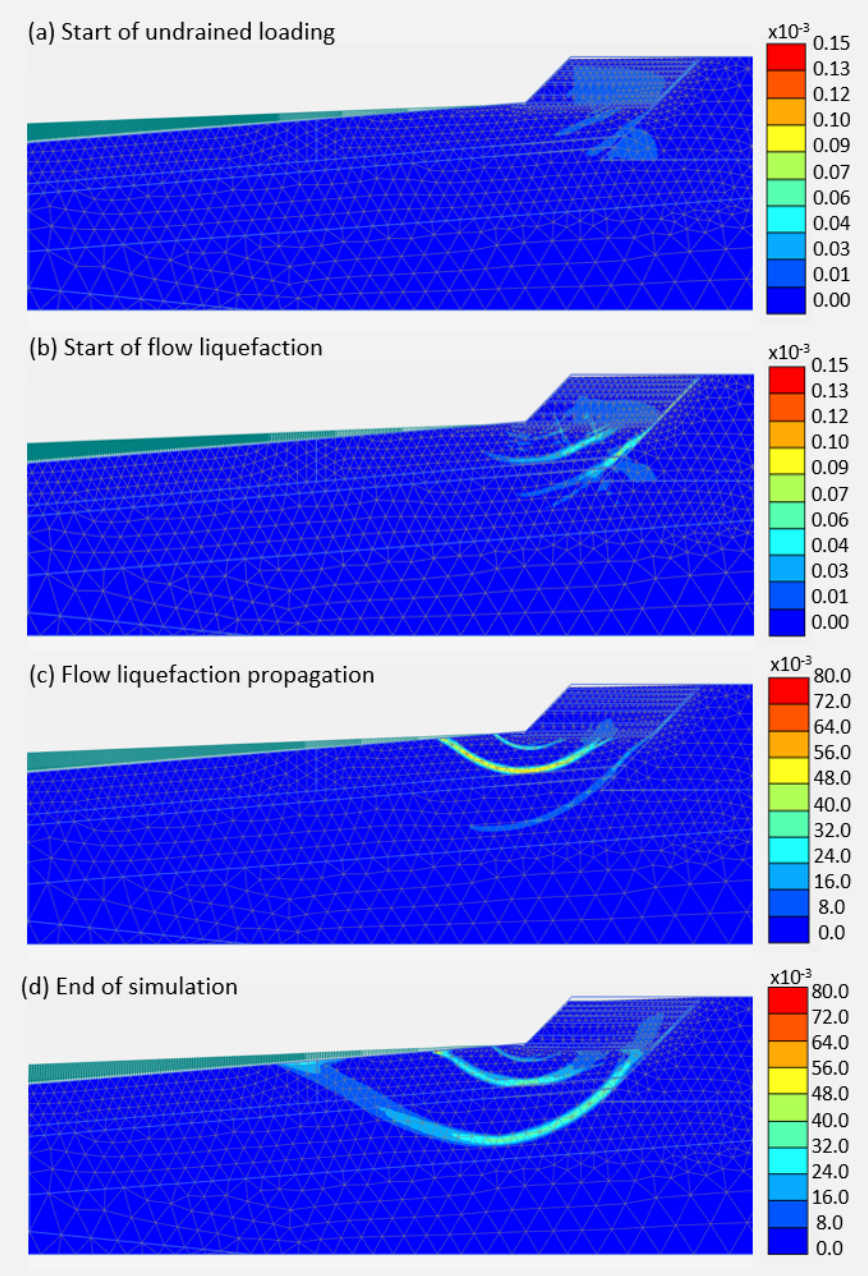

Figure 7.23: Incremental deviatoric strains for different moments of loading for Scenario 2

Comparison of the responses obtained when using CASM and NorSand

Given the results obtained for the Tar Island Dyke slump simulation when using NorSand, Shuttle et al. (2021) argue that the closest match between numerical data and field observations was obtained when the denser zones in the tailings were not considered in the model, which is the case of Scenario 2 in the present study. As such, with the purpose of comparing the responses computed with CASM and NorSand, only the results of Scenario 2 are considered. Moreover, note that the numerical results obtained using NorSand and CASM are compared for the same loading stage (ΣMstage = 0.251), which corresponds to the maximum load reached during the simulation using CASM

The results of the simulations in terms of excess pore pressures are shown in Figure 7.24, where it can be observed that excess pore pressures build-up quicker when using CASM than when using NorSand since higher excess pore pressures are computed with CASM. Moreover, Figure 7.25 shows the incremental deviatoric strains corresponding to the mentioned loading stage. It can be observed that

in the case of CASM (Figure 7.25a), significantly large incremental deviatoric strains develop along the weak layer and underneath the compacted cell. On the contrary, when using NorSand (Figure 7.25b), the incremental deviatoric strains at this loading stage can still be considered small, with no clear signs yet of a failure mechanism being developed underneath the compacted cell and along the weak layer.

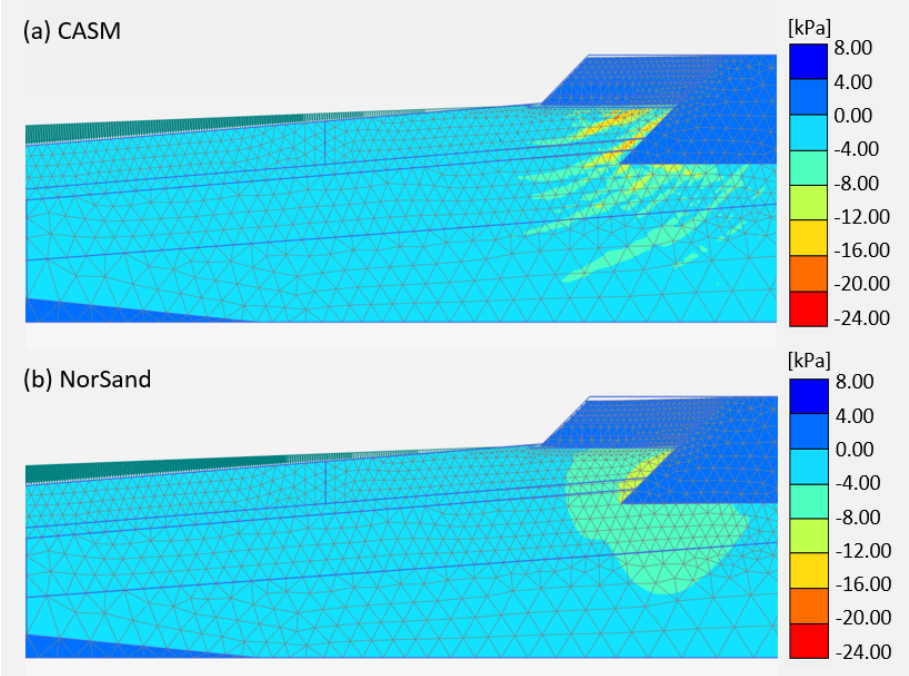

Figure 7.24: Excess pore pressures for the Tar Island Dyke model using CASM and NorSand at the same loading stage.

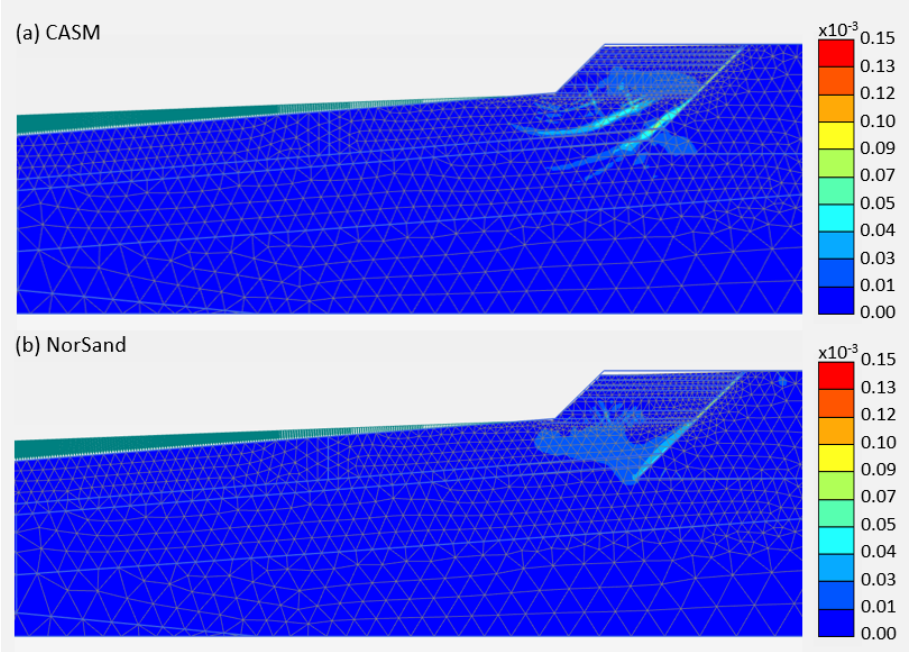

Figure 7.25: Excess pore pressures for the Tar Island Dyke model using CASM and NorSand at the same loading stage.

Even though the failure mechanism develops quicker when using CASM, the total accumulated displacements are smaller than those obtained using NorSand. This can be observed in Figure 7.26, which presents the contours of total displacements at the same loading stage. It is nevertheless important

to note that larger total displacements accumulate not only during the last undrained loading phase but also during the previous drained phases corresponding to the placement of the first four layers of the compacted cell. This is shown in Figure 7.27, where it is apparent that the total maximum displacement of each phase is around 40 to 50 % times larger when using NorSand.

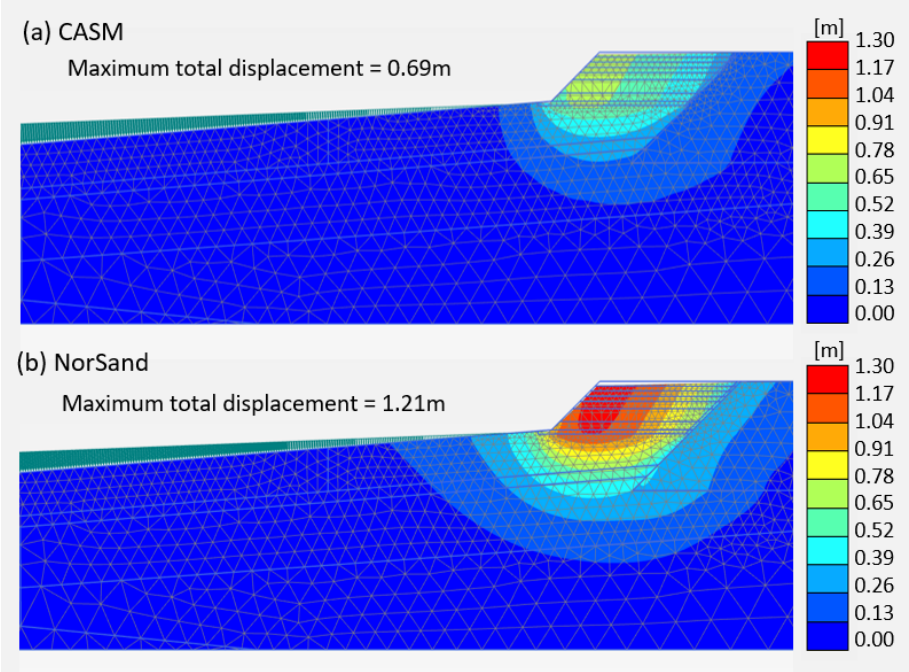

Figure 7.26: Total displacement for the Tar Island Dyke model using CASM and NorSand at the same loading stage.

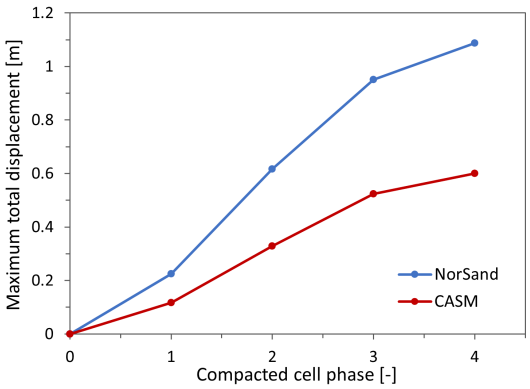

Figure 7.27: Maximum total displacements for the first four drained loading phases of the Tar Island Dyke simulation.

Finally, Figure 7.28 and Figure 7.29 show the contours of the state parameter and deviatoric strain increments at different loading stages during the simulations. In terms of state parameter, it can be observed that for both simulations, at the start of the undrained loading (Figure 7.28a), the tailings underneath the compacted cell are similar to the initial state parameter ($\psi_0 = 0.06$). At the end of the simulations (Figure 7.28c), these tailings reach the critical state ($\psi = 0$). In terms of incremental deviatoric strains, it can be mentioned that the failure mechanisms obtained in the two simulations have a similar shape, with the one obtained with CASM being slightly deeper but about 40 m narrower than that obtained when using NorSand. Note, however, that it was not possible to apply in the simulation with CASM the same number of unloading steps selected for the simulation with NorSand and, therefore, it is unclear whether the deformation mechanism obtained in the former simulation could evolve further and eventually become similar to that obtained in the latter simulation.

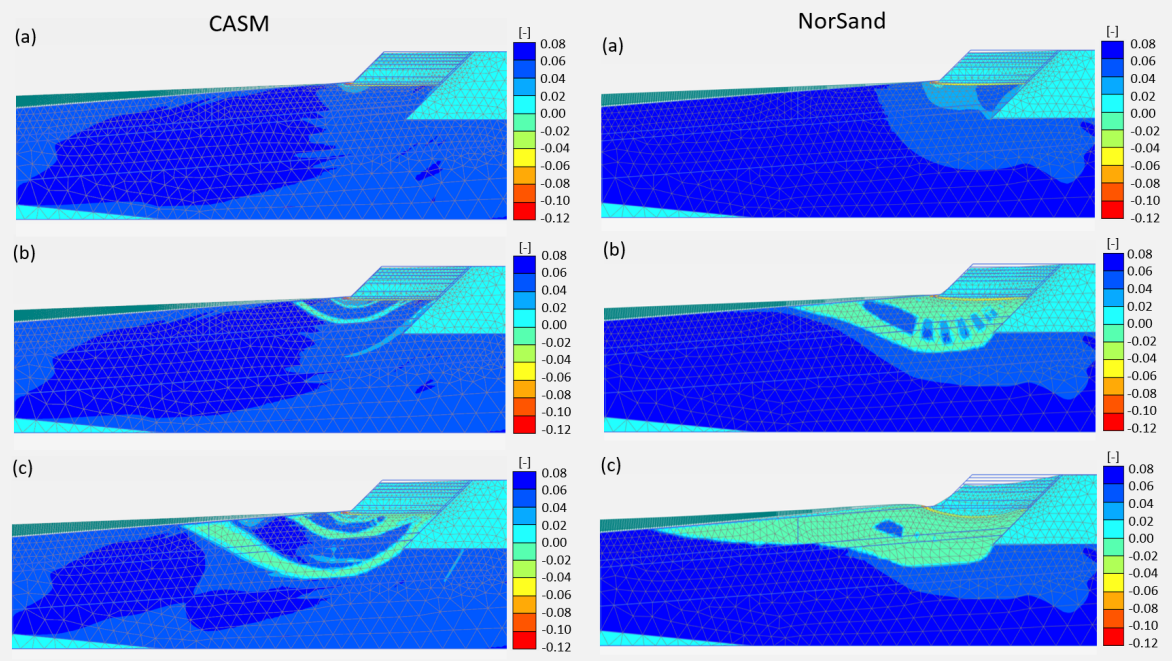

Figure 7.28: State parameter for the Tar Island Dyke model using CASM and NorSand at different loading stages.

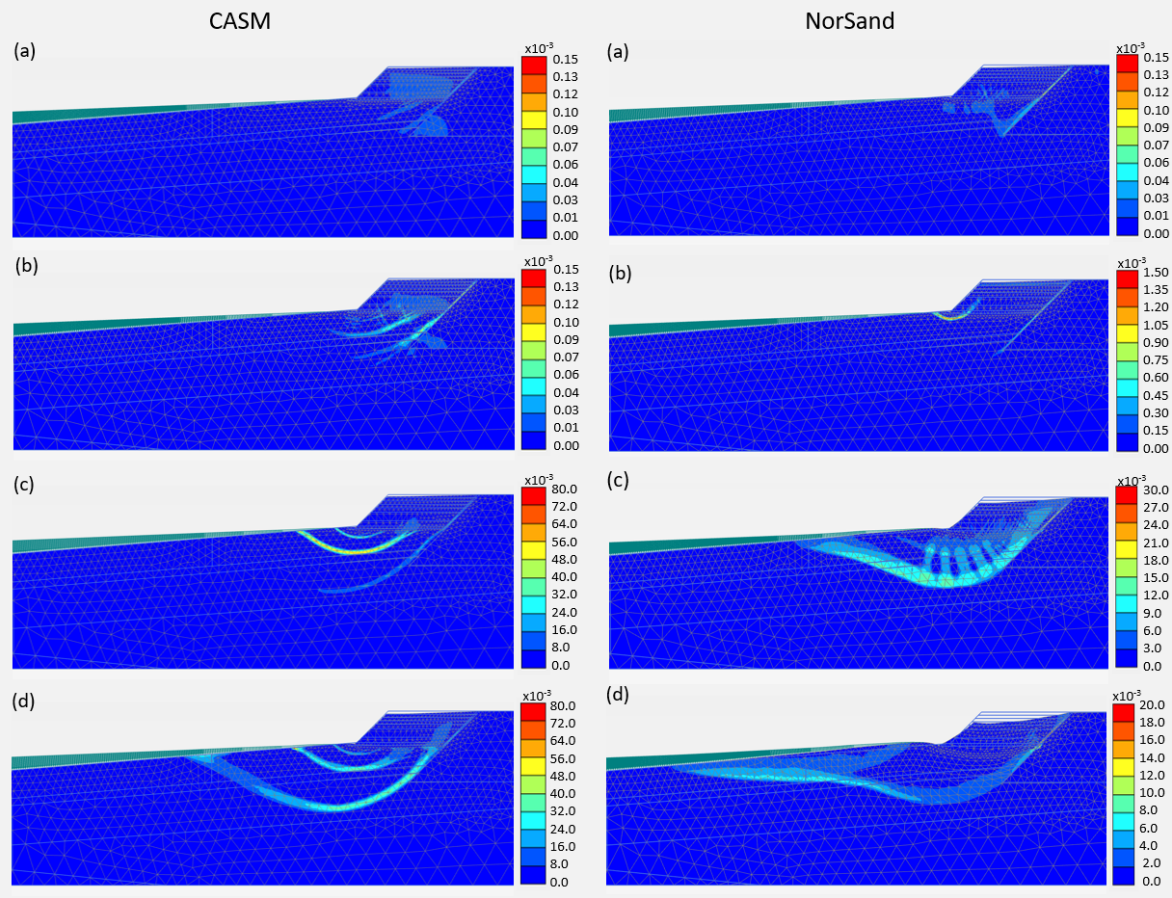

Figure 7.29: Incremental deviatoric strains for the Tar Island Dyke model using CASM and NorSand at different loading stages.

The results obtained using CASM and NorSand show the same responses for both boundary value problems. Under drained conditions, larger total displacements are computed using NorSand, which may be related to the differences between the models in terms of formulations. CASM and NorSand use different plastic potential surfaces and hardening rules resulting in the calculation of different plastic strain components, and therefore, the displacements are different. Under undrained conditions, the results suggest a lower strength of the models simulated with CASM with higher excess pore pressure build-up and reaching failure at earlier loading stages. The results of the Tar Island Dyke simulation using both models show a similar behaviour in terms of excess pore pressures and state parameter with excess pore pressures build-up underneath the compacted cell and tailings with state parameters approaching the critical state during the undrained loading. Moreover, similar failure mechanisms identified by means of the incremental deviatoric strains are developed, starting along the weak layer and below the compacted cell. These results indicate that the simulations performed with both models fail due to flow liquefaction triggered by undrained loading.

8

Conclusions and future research

8.1. Conclusions

The aim of the present research was to assess the capabilities and limitations of NorSand and CASM in the analysis of flow liquefaction using the geotechnical finite element software PLAXIS. The approach used to reach this aim was to perform comparative analyses of the model results at three different study levels: material point level, simple boundary value problem level, and complex boundary value problem level. To carry out these analyses, firstly, the implementation of the models into PLAXIS was successfully verified. Specifically, in the present research, CASM was extensively verified at a stress point level for several stress paths and in simple boundary value problems. Moreover, additional verification exercises were performed for NorSand, which was previously verified and tested by other works (Woudstra, 2021). Complementary, a series of parametric sensitivity analyses were performed to have a better insight into the effect of the parameters on the models' responses. Finally, the sets of parameters used during the simulations were calibrated and validated for the same Tar Island tailings materials.

To reach the research aim, three research questions were formulated, the first being related to the model differences in terms of formulations and application. Significant differences and similarities were identified from the literature review and during the research. Both NorSand and CASM are developed within the critical state soil mechanics framework characterised by a single yield surface that encloses a domain inside which the behaviour is purely elastic. A hypoelastic formulation is used in both cases. However, CASM assumes a linear dependency of the bulk and shear stiffness on the mean pressure, while they can vary non-linearly in the case of NorSand, according to a power law. In the case of NorSand, the yield function has the same unique shape as the one defining the Original Cam-Clay model, with a plastic potential function coinciding with it. This means that an associated flow rule is assumed, with the direction of the plastic strain increment vector being perpendicular to the yield surface. On the contrary, CASM is characterised by a more versatile yield function that can assume different shapes by varying the value of the parameter n. Consequently, the plastic potential function can also be defined such that both an associated and a non-associated flow rule can be adopted. CASM and NorSand assume that a unique critical state line can be identified, both in the $(\ln p' - v)$ plane, by defining the specific volume or void ratio at critical state at a mean pressure of 1 kPa and a slope λ, and in the $(p' - q)$ plane, through the friction angle or the critical stress ratio. However, CASM assumes a unique reference consolidation line, which always lies above (as a function of the spacing ratio r) and parallel to the critical state line in the $(\ln p' - v)$ plane (i.e., it is characterised by the same slope λ). Instead, NorSand considers the possibility that an infinite number of normally consolidation lines may exist in the $(\ln p' - v)$ plane. These NCLs depend on the initial void ratio at deposition and are not parallel to the CSL. Additionally, NorSand gives the possibility to alternatively model a non-linear CSL. Another substantial difference between the two constitutive model formulations is the dependency of the hardening variable on the plastic volumetric strains only, in the case of CASM, and on the plastic deviatoric strains only, in the case of NorSand. Moreover, to define the initial state, it is necessary to specify the values of the state parameter and overconsolidation ratio in the case of NorSand. In addition to this option, CASM offers the possibility to input other combinations of parameters, such as

the initial void ratio and the preconsolidation stress. Finally, the version of CASM used in this research includes a visco-plastic extension based on the overstress theory of Perzyna (1966).

In terms of parameters, CASM requires the definition of at least 10 model parameters, while NorSand involves a total of 14 or 15 parameters depending on the CSL alternative chosen. Most of the parameters can be estimated through conventional laboratory tests or in-situ tests, as shown in the case of the Mildred Lake tailings. Both models require the determination of λ, Γ, ϕ_{cs}, and ν by means of very well-established calibration procedures using laboratory experimental data. In the case of NorSand, the elastic behaviour is primarily defined in terms of the elastic shear stiffness at a reference pressure, G_{ref}, which may depend non-linearly on the pressure through the exponent n_G. The shear stiffness is used to calculate the bulk stiffness K as a function of ν. On the contrary, CASM requires the definition of K through the slope of the swelling line κ in the semi-logarithmic plane. The rest of the parameters necessary to complete NorSand are estimated through strategies where drained triaxial test data are required. For CASM, the remaining parameters, n, r and m, can be directly determined based on conventional laboratory tests that describe the material behaviour according to different stress paths. For example, oedometer test data are valuable for the calibration of the parameters r and m. Triaxial tests performed at different confining pressures may allow identifying the locus of the yield points and, therefore, determine n. When experimental data are lacking, or as a first estimation, empirical equations can be used, assuming normally consolidated conditions. In the present study, due to the limited experimental data, the Tar Island tailings (i.e. Albian and Mildred Lake tailings) were calibrated through empirical equations with satisfactory results when simulating the response of loose samples and with questionable results for dense samples. In principle, the calibration of both models is relatively straightforward if the required experimental data is available. However, when the data is limited, empirical formulations can be used to estimate the parameters of CASM, while the calibration of NorSand seems to be constrained to the procedures described above.

A second research question related to the accuracy of the models in predicting the response of tailings under monotonic loading conditions was formulated. For this, the material point level study shows that both NorSand and CASM are models capable of reproducing flow liquefaction, matching experimental data very well when imposing undrained conditions at loose state. Moreover, the simulation results of direct simple shear tests and monotonic triaxial tests under both drained and undrained conditions show similar responses for loose samples. Nevertheless, some differences were found under other conditions. As reported by Shuttle et al. (2021), NorSand reproduces very well qualitatively and quantitatively monotonic triaxial compression test on dense samples. On the contrary, CASM presents a rather linear response initially stiffer than NorSand and experimental data, which is associated with the large elastic domain computed for dense materials (i.e. $\psi < 0$) and the low inclination of the NCL defined by λ. These observations suggest a limitation of CASM for simulations on dense materials, at least with the parameters used in the present study. Therefore, CASM is not suitable for materials characterised by a negative state parameter (i.e. dense materials). Additionally, considerable differences were observed during oedometer test simulations using NorSand and CASM. NorSand presents a stiffer response and, particularly for the set of parameters used, an unrealistic K_0 approximate to 1 is computed, leading to a stress path similar to that one of an isotropic consolidation where the deviatoric stresses are equal to zero. On the other hand, the results obtained with CASM denote the expected results with the inclination of the consolidation line equal to the parameter λ and the K_0 computed equal to the value desired when calibrating the parameter m. It is important to remark that these tests were performed using a state parameter characterising a loose sample (i.e. $\psi > 0$).

To answer the last question regarding the performance of CASM and NorSand in boundary value problems, two boundary value problems were analysed, corresponding to the simulation of an embankment construction and the flow liquefaction in the Tar Island Dyke. The results of these analyses denote significant differences in terms of stress-strain response. The results obtained with CASM show lower strength and higher stiffness than those obtained with NorSand. During the drained and consolidations analysis, smaller total displacements were obtained in the simulations using CASM at the end of each loading state, while during the undrained analysis, the simulations performed with CASM reached failure at earlier loading stages than NorSand, suggesting a weaker response. Moreover, similar to the observations made in the odometer test simulations using NorSand, very low deviatoric stresses are

identified in the tailings deposits during the initial loading phases, where the loading conditions are relatively similar to one-dimensional consolidation.

The analysis of the Tar Island Dyke slump proved that as NorSand, CASM is able to reproduce flow liquefaction, which in this study is assessed in terms of the generation of large excess pore pressures and the evolution of the state parameters approaching the critical state. Two different scenarios were established for these simulations. The first considers the presence of the dense BAW tailings layer, and the second considers only loose BBW tailings deposit. As expected, the Scenario 2 results show a larger failure mechanism due to the absence of dense BAW tailings. Compared with the results obtained using NorSand, in terms of failure mechanism, the results are qualitatively similar, representing very well the observations reported. However, the displacements were not accurately computed with smaller values computed by the model simulated with CASM. This may be improved using a larger number of unloading steps, representing a numerical limitation for this model since larger maximum unloading steps could not be defined.

Finally, NorSand and CASM are models that can be used to analyse flow liquefaction events. In professional practice, since most of the parameters used by the models are the same and the particular parameters of CASM can be estimated through correlations assuming normally consolidated conditions, the application of the models can be complementary for performing a qualitative assessment of a flow liquefaction event. The selection of a single model may be subject to the available data to calibrate the models parameters and the state conditions of the soil material to be simulated due to the fact that, as implemented, CASM presents limitations to reproduce accurately the response of sand or tailings at dense state, but is suitable for materials at loose state, which are those considered to be susceptible to flow liquefaction.

8.2. Future research

This research was carried out by evaluating some simple ideal cases and one complex case study. However, the tailings mechanical behaviour can widely vary due to its nature, and further research involving also other case studies may be necessary to support the conclusions found in this work. Additionally, given the viscoplasticity extension already characterising CASM, future research can address this aspect as well.

At the material point level, this research highlighted a limitation of CASM in quantitatively reproducing the behaviour of dense materials. Future developments may involve new strategies to improve its ability in this direction. Moreover, regarding the findings using NorSand, the unrealistic stress paths obtained during the oedometer test may be further explored by evaluating the influence of this behaviour on the accuracy of the results of boundary value problems.

Moreover, during the present work, some mesh dependency results were found, as well as slight discrepancies for some verification exercises performed for CASM, which, as reported in Chapter 4 might be related to some inaccuracy in the initial conditions reported in the literature. Due to time constraints, they were not investigated in depth in this work and may be important aspects to be reviewed to improve the implementation and robustness of the models.

Finally, the models have been applied here for the simulation of tailings. However, the capabilities of the models to simulate the behaviour of other classes of materials, such as clays, could be investigated. This would give more insights into the models abilities and could lead to outlining more simple and robust calibration procedures or indication of ranges of values for the model parameters based on the material.

References

Alonso, E. E., Gens, A., & Josa, A. (1990). A constitutive model for partially saturated soils. *Géotechnique*, *40*(3), 405–430.

Arroyo, M., & Gens, A. (2021). Computational analyses of Dam I failure at the Corrego de Feijao mine in Brumadinho – final report.

Been, K., Jefferies, M. G., & Hachey, J. (1991). The critical state of sands. *Geotechnique*, *41*(3), 365–381.

Been, K., & Jefferies, M. (1985). A state parameter for sands. *Géotechnique*, *35*(2), 99–112.

Been, K., & Jefferies, M. (2004). Stress dilatancy in very loose sand. *Canadian Geotechnical Journal*, *41*(5), 972–989.

Bowker, L. N., & Chambers, D. M. (2016). *Root causes of tailings dam overtopping: The economics of risk & consequence* (Doctoral dissertation). Colorado State University. Libraries.

Brinkgreve, R. B. J., Kumarswamy, S., & Swolfs, W. M. (2022). Plaxis 2022 user manual.

Caldwell, J. A., & Smith, A. (1985). Material considerations in the design of downstream embankments for tailings impoundments. *Mining Science and Technology*, *3*(1), 35–49.

Casagrande, A., & Shannon, W. (1949). Strength of soils under dynamic loads. *Transactions of the american society of civil engineers*, *114*(1), 755–772.

Castro, G., Enos, J., France, J. W., & Poulos, S. (1982). Liquefaction induced by cyclic loading. *NASA STI/Recon Technical Report N*, *83*, 13308.

Cheng, Z., & Jefferies, M. (2020). Implementation and verification of norsand model in general 3d framework. *Geo-Congress 2020: Geotechnical Earthquake Engineering and Special Topics*, 10–19.

Coop, M., & Lee, I. (1993). The behaviour of granular soils at elevated stresses. predictive soil mechanics—proc. wroth memorial symposium.

Das, B. (2008). Advanced soil mechanics: Tylor & frances.

Davies, M., & Martin, T. (2000). Upstream constructed tailings dams–a review of the basics. *Tailings and Mine Waste 2000*, 3–15.

Davies, M., McRoberts, E., & Martin, T. (2002). Static liquefaction of tailings–fundamentals and case histories. *Proceedings Tailings Dams ASDSO/USCOLD*, 233–255.

Drucker, D. C., Gibson, R. E., & Henkel, D. J. (1957). Soil mechanics and work-hardening theories of plasticity. *Transactions of the American Society of Civil Engineers*, *122*(1), 338–346.

Fourie, A., Blight, G., & Papageorgiou, G. (2001). Static liquefaction as a possible explanation for the merriespruit tailings dam failure. *Canadian Geotechnical Journal*, *38*(4), 707–719.

Google Earth Pro 7.3.6. (2023). Tar Island Dyke location 56°59'44.53"N, 111°29'25.18"W, aerial view from 2006.

ICOLD. (1989). Tailings dams safety – guidelines (bulletin 74). *Commission Internationale des Grands Barrages, Paris*.

ICOLD. (2001). Tailings dams – risk of dangerous occurrences, lessons learnt from practical experiences (bulletin 121). *Commission Internationale des Grands Barrages, Paris*, *155*.

Ishihara, K. (1993). Liquefaction and flow failure during earthquakes. *Geotechnique*, *43*(3), 351–451.

Islam, K., & Murakami, S. (2021). Global-scale impact analysis of mine tailings dam failures: 1915–2020. *Global Environmental Change*, *70*, 102361.

Jaky, J. (1944). The coefficient of earth pressure at rest. *Journal of the Society of Hungarian Architects and engineers*.

Jefferies, M. (1993). Nor-sand: A simple critical state model for sand. *Geotechnique*, *43*(1), 91–103.

Jefferies, M., & Been, K. (2006). Soil liquefaction: A critical state approach.

Jefferies, M., & Been, K. (2015). *Soil liquefaction: A critical state approach*. CRC press.

Jefferies, M., Shuttle, D., & Been, K. (2015). Principal stress rotation as cause of cyclic mobility. *Geotechnical Research*, *2*(2), 66–96.

Kavvadas, M., & Amorosi, A. (1998). A plasticity approach for the mechanical behaviour of structured soils. *The geotechnics of hard soils-soft rocks*, 603–613.

Kramer, S. L. (1996). *Geotechnical earthquake engineering*. Pearson Education India.

Kramer, S. L., & Elgamal, A.-W. M. (2001). *Modeling soil liquefaction hazards for performance-based earthquake engineering*. Pacific Earthquake Engineering Research Center, College of Engineering …

Kun, W., Peng, Y., Hudson-Edwards, K., Wen-sheng, L., & Lei, B. (2018). Status and development for the prevention and management of tailings dam failure accidents. , *40*(5), 526–539.

Lade, P. V. (1993). Initiation of static instability in the submarine nerlerk berm. *Canadian Geotechnical Journal*, *30*(6), 895–904.

Lazenby, H. (2022). Analysis: No reduction in tailings dam failures over the past two decades. *The Northern Miner: Global mining news*. Retrieved September 6, 2022, from https://www.northernminer.com/news/analysis-no-reduction-in-tailings-dam-failures-over-the-past-two-decades/

Ledesma, O., Sfriso, A., & Manzanal, D. (2022). Procedure for assessing the liquefaction vulnerability of tailings dams. *Computers and Geotechnics*, *144*, 104632.

Lee, K. L., Seed, H. B., & Dunlop, P. (1966). The effect of transient loading on the strength of sand.

Li, X. S., & Dafalias, Y. F. (2000). Dilatancy for cohesionless soils. *Géotechnique*, *50*(4), 449–460.

Lumbroso, D., McElroy, C., Goff, C., Collell, M. R., Petkovsek, G., & Wetton, M. (2019). The potential to reduce the risks posed by tailings dams using satellite-based information. *International journal of disaster risk reduction*, *38*, 101209.

Mánica, M. A., Arroyo, M., Gens, A., & Monforte, L. (2022). Application of a critical state model to the merriespruit tailings dam failure. *Proceedings of the Institution of Civil Engineers-Geotechnical Engineering*, *175*(2), 151–165.

Massarsch, K., Risk, G., & AB, V. S. (2015). Determination of shear modulus of soil from static and seismic penetration testing. *Jubilee volume. Proceedings in honour of Prof. A. Anagnostopoulos, Technical University of Athens*, 335–352.

McDowell, G., & Hau, K. (2003). A simple non-associated three surface kinematic hardening model. *Géotechnique*, *53*(4), 433–437.

Mittal, H. K., & Hardy, R. M. (1977). Geotechnical aspects of a tar sand tailings dyke.

O'Brien, K., O'Brien, T., & Robinson, B. (2021). Using the norsand constitutive model as a tool in assessing the static and dynamic stability of tailings slopes containing contractive material.

Ohmaki, S. (1982). Stress-strain behaviour of anisotropically, normally consolidated cohesive soil.

Olson, S. M., & Stark, T. D. (2003). Yield strength ratio and liquefaction analysis of slopes and embankments. *Journal of Geotechnical and Geoenvironmental Engineering*, *129*(8), 727–737.

Olson, S. M. (2001). *Liquefaction analysis of level and sloping ground using field case histories and penetration resistance*. University of Illinois at Urbana-Champaign.

Perzyna, P. (1966). Fundamental problems in viscoplasticity. *Advances in applied mechanics*, *9*, 243–377.

Piciullo, L., Storrøsten, E. B., Liu, Z., Nadim, F., & Lacasse, S. (2022). A new look at the statistics of tailings dam failures. *Engineering Geology*, *303*, 106657.

Plewes, H., McRoberts, E., & Chun, W. (1988). Downhole nuclear density logging in sand tailings. In *Hydraulic fill structures*.

Plewes, H., O'Neil, G., McRoberts, E., & Chan, W. (1989). Liquefaction considerations for suncor tailings pond. *Proceedings of the Dam Safety Seminar, Edmonton, Alberta, Sept*, *1*, 61–89.

Potts, D. M., & Zdravkovic, L. (1999). *Finite element analysis in geotechnical engineering: Theory* (Vol. 1). Thomas Telford.

Robertson, P. K., De Melo, L., Williams, D., & Wilson, G. W. (2019). Report of the expert panel on the technical causes of the failure of feijão dam i. *Commissioned by Vale*, *81*.

Robertson, P. (1997). Liquefaction of sands and its evaluation. *Proc. IS-TOKYO'95/The 1st Intl. Conf. on Earthquake Geotech. Engrg.*, 1253–1289.

Roche, C., Thygesen, K., & Baker, E. (2017). Mine tailings storage: Safety is no accident (arendal: Un environment, grid-arendal, november 2017).

Roscoe, K., & Burland, J. (1968). On the generalized stress-strain behaviour of wet clay.

Rowe, P. W. (1962). The stress-dilatancy relation for static equilibrium of an assembly of particles in contact. *Proceedings of the Royal Society of London. Series A. Mathematical and Physical Sciences*, *269*(1339), 500–527.

Schofield, A. N., & Wroth, P. (1968). *Critical state soil mechanics* (Vol. 310). McGraw-hill London.

Sheng, D., Sloan, S., & Yu, H. (2000). Aspects of finite element implementation of critical state models. *Computational mechanics*, *26*, 185–196.

Shuttle, D., & Jefferies, M. (2010). Norsand: Description, calibration, validation and applications. *Geofrontiers congress 2005–Soil constitutive models: evaluation, selection, and calibration*, 204–236.

Shuttle, D., Marinelli, F., Brasile, S., & Jefferies, M. (2021). Validation of computational liquefaction for tailings: Tar island slump. *Geotechnical Research*, *9*(1), 32–55.

Shuttle, D., Martens, S., & Jefferies, M. (2023). Geostatic stress in oil-sand tailings. *Proceedings of the Institution of Civil Engineers - Geotechnical Engineering*, *176*(3), 274–283. https://doi.org/10.1680/jgeen.21.00114

Simo, J. (1989). Strain softening and dissipation: A unification of approaches. *Cracking and damage: strain localization and size effect*, 440–461.

Sladen, J., D'hollander, R., & Krahn, J. (1985). The liquefaction of sands, a collapse surface approach. *Canadian geotechnical journal*, *22*(4), 564–578.

Terzaghi, K., & Peck, R. B. (1948). Soil mechanics. *Engineering Practice. John Wiley and Sons, Inc., New York*.

Vick, S. G. (1990). *Planning, design, and analysis of tailings dams*. BiTech Publishers Ltd.

Vick, S. G. (1996). Landslides: Investigation and mitigation. chapter 22-hydraulic tailings. *Transportation Research Board Special Report*, (247).

Woudstra, L.-J. (2021). Verification, validation and application of the norsand constitutive model in plaxis: Single-stress point analyses of experimental lab test data and finite element analyses of a submerged landslide.

Yang. (2002). Non-uniqueness of flow liquefaction line for loose sand. *Géotechnique*, *52*(10), 757–760.

Yang & Yu, H. S. (2006). A non-coaxial critical state soil model and its application to simple shear simulations. *International journal for numerical and analytical methods in geomechanics*, *30*(13), 1369–1390.

Yu, H. S. (1998). Casm: A unified state parameter model for clay and sand. *International journal for numerical and analytical methods in geomechanics*, *22*(8), 621–653.

Yu, H. S. (2006). Plasticity and geotechnics. *Plasticity and Geotechnics*.

Yu, H. S., Khong, C., Wang, J., & Zhang, G. (2005). Experimental evaluation and extension of a simple critical state model for sand. *Granular Matter*, *7*, 213–225.

Zheng, L., Jin, L., & Liu, F. (2022). Norsand modelling for evaluating the triggering of flowslides in loess.

A

Sensitivity analysis results

A.1. CASM - Dense samples

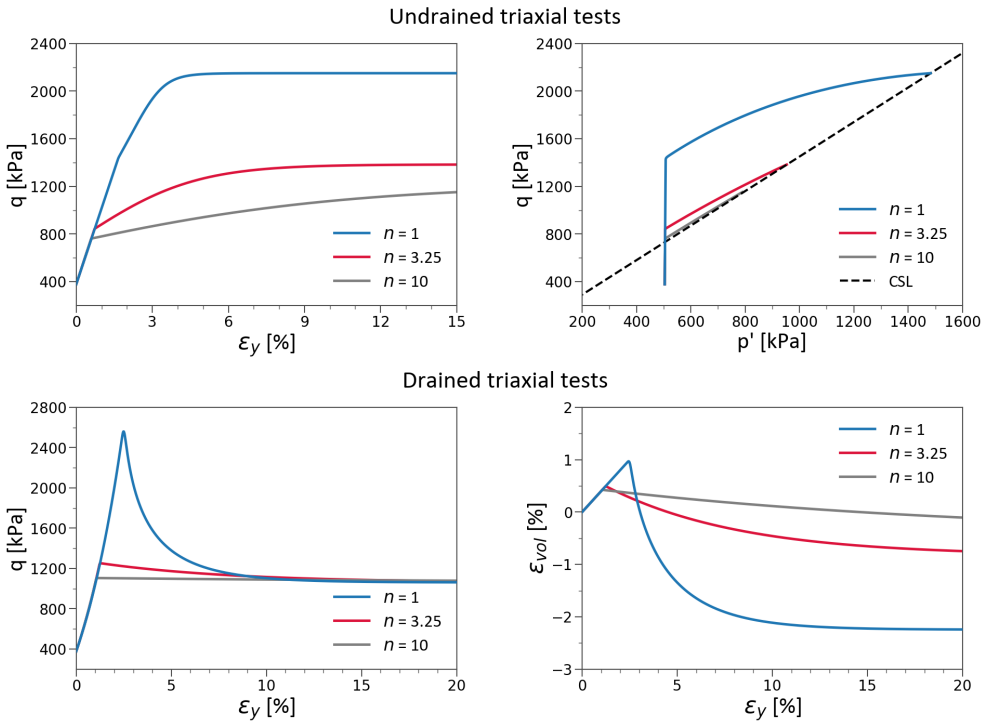

Figure A.1: Sensitivity analysis results for the parameter n on dense material.

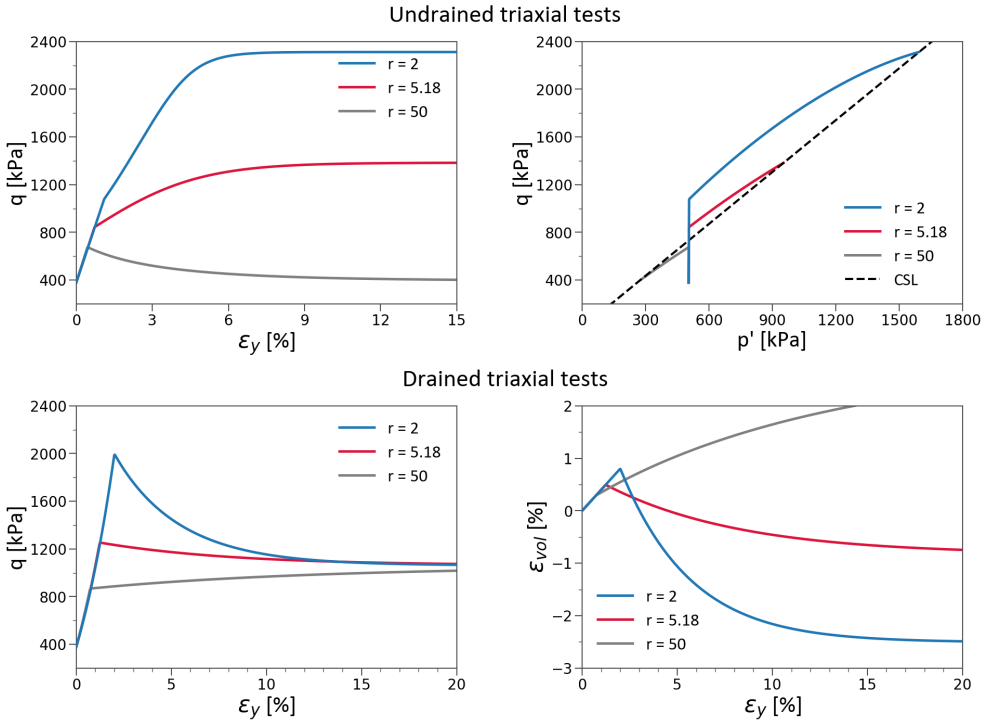

Figure A.2: Sensitivity analysis results for the parameter r on dense material.

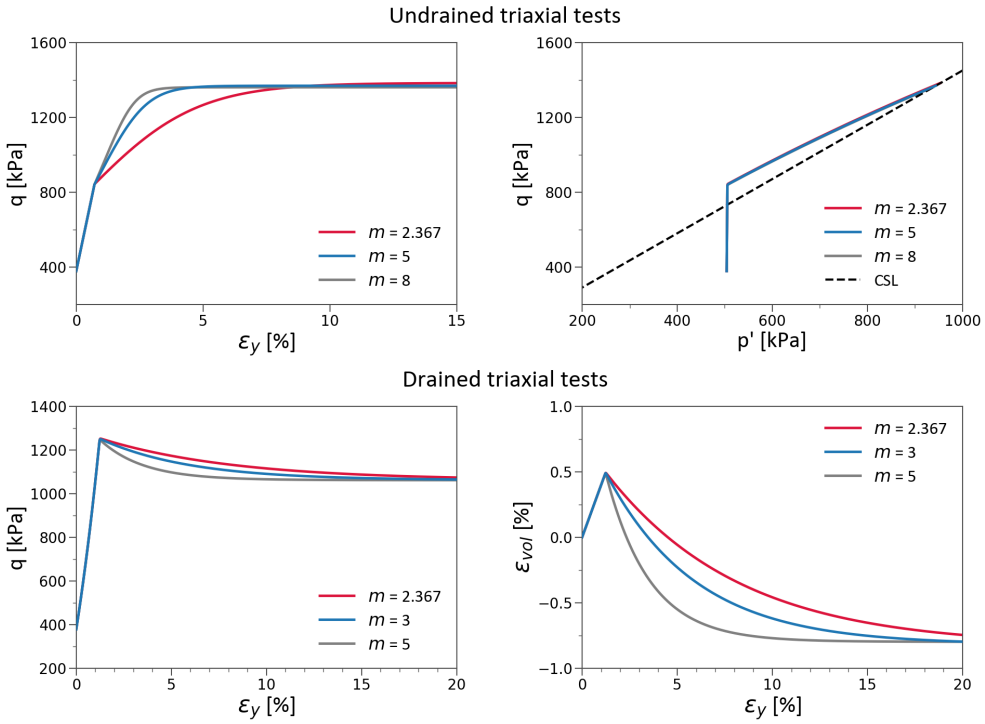

Figure A.3: Sensitivity analysis results for the parameter m on dense material.

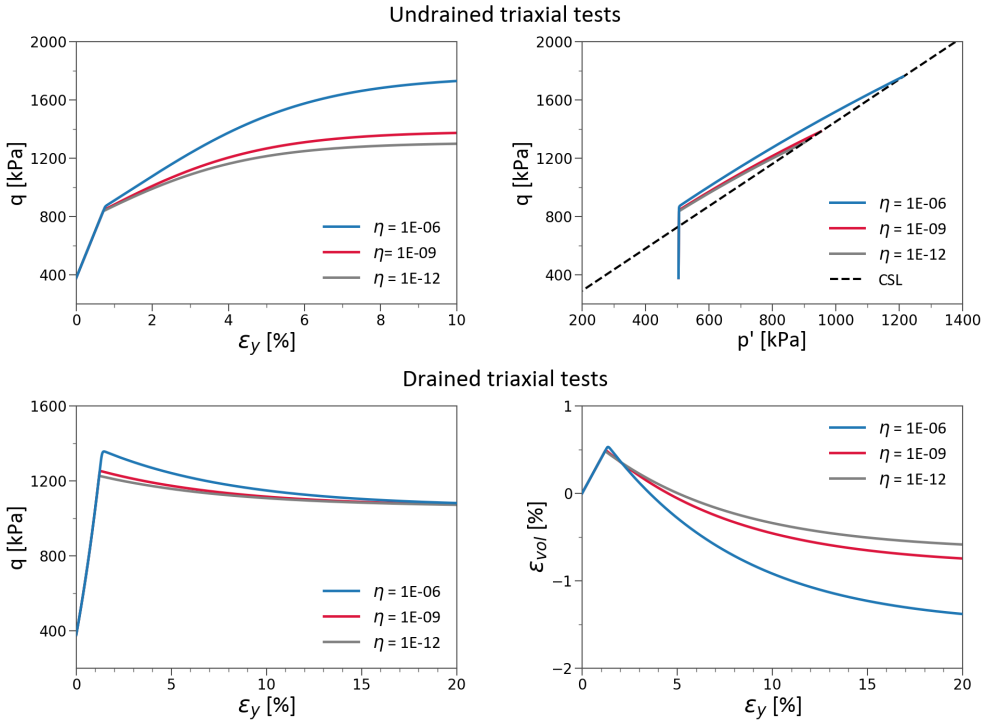

Figure A.4: Sensitivity analysis results for the viscosity parameter η on dense material.

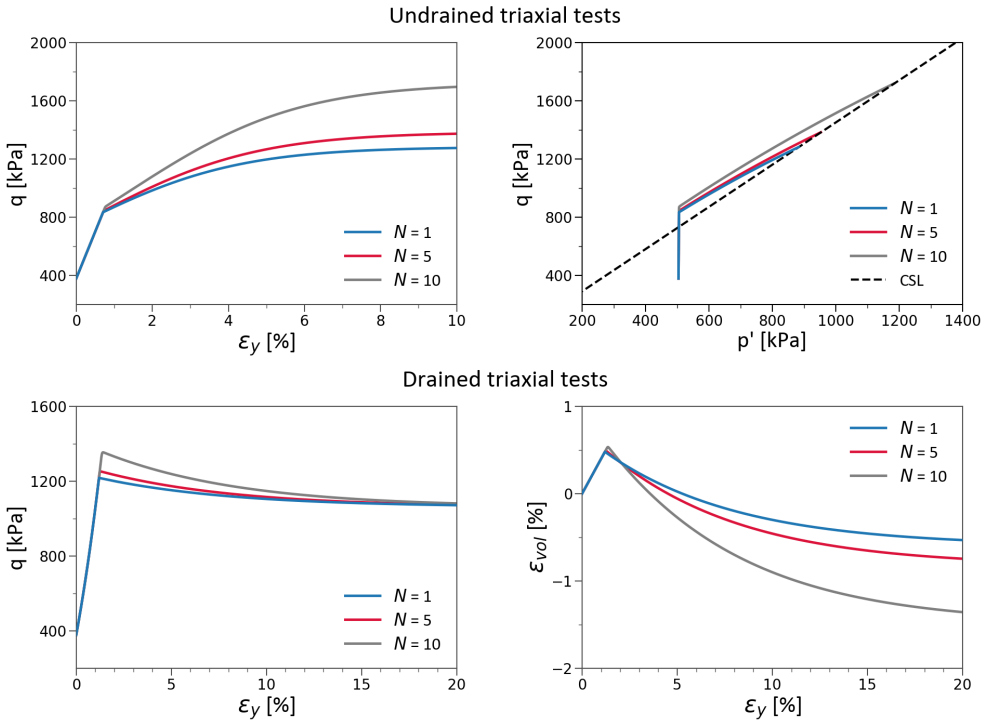

Figure A.5: Sensitivity analysis results for the viscosity parameter N on dense material.

A.2. NorSand - Dense samples

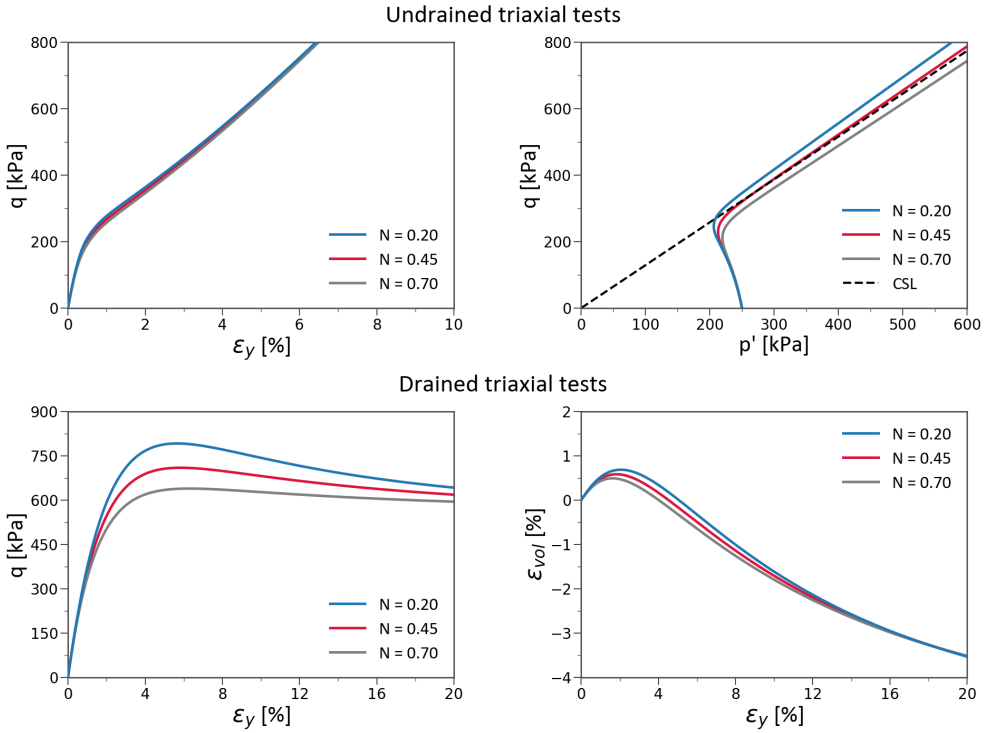

Figure A.6: Sensitivity analysis results of the volumetric coupling parameter, N, on dense material.

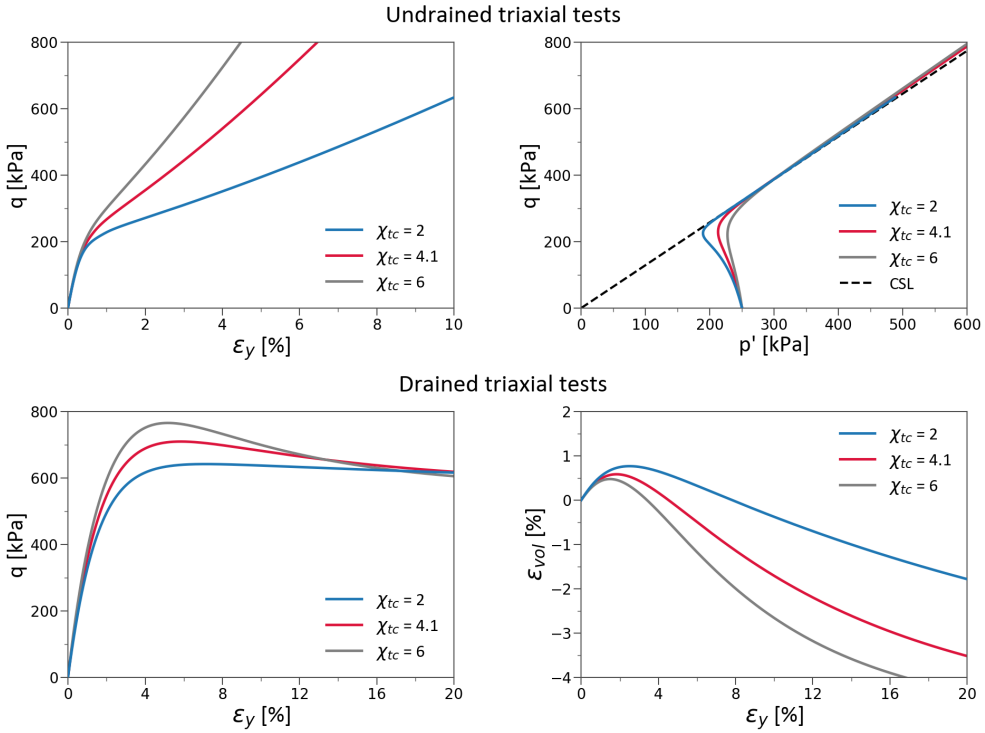

Figure A.7: Sensitivity analysis results of the state-dilatancy parameter, χ_{tc}, on dense material.

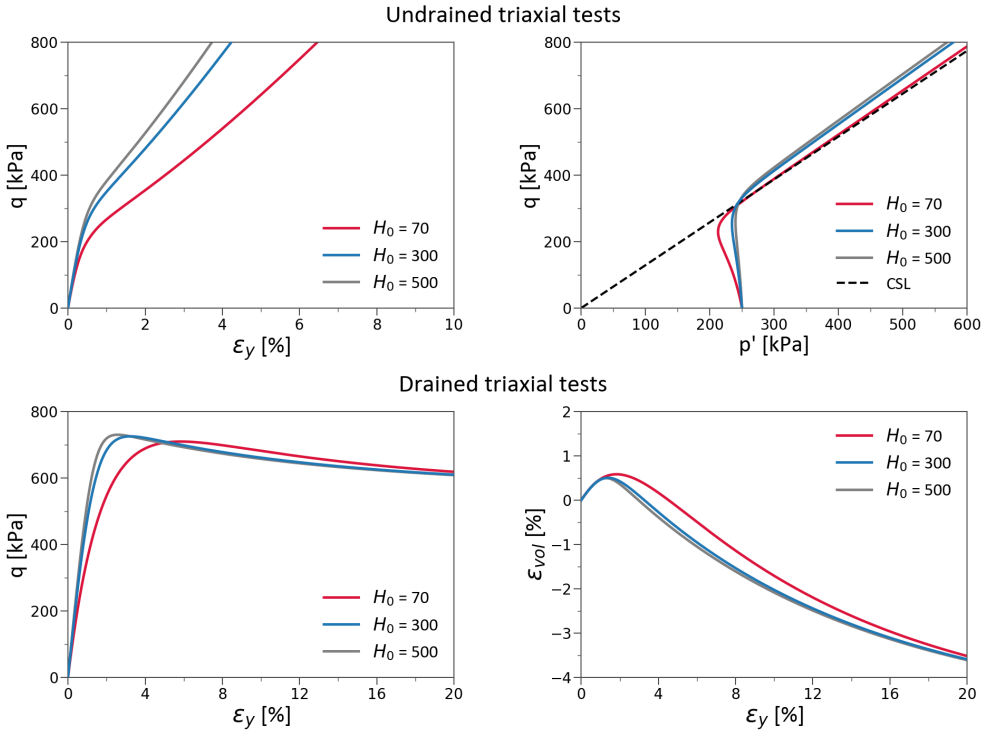

Figure A.8: Sensitivity analysis results of the hardening parameter, H_θ, on dense material.

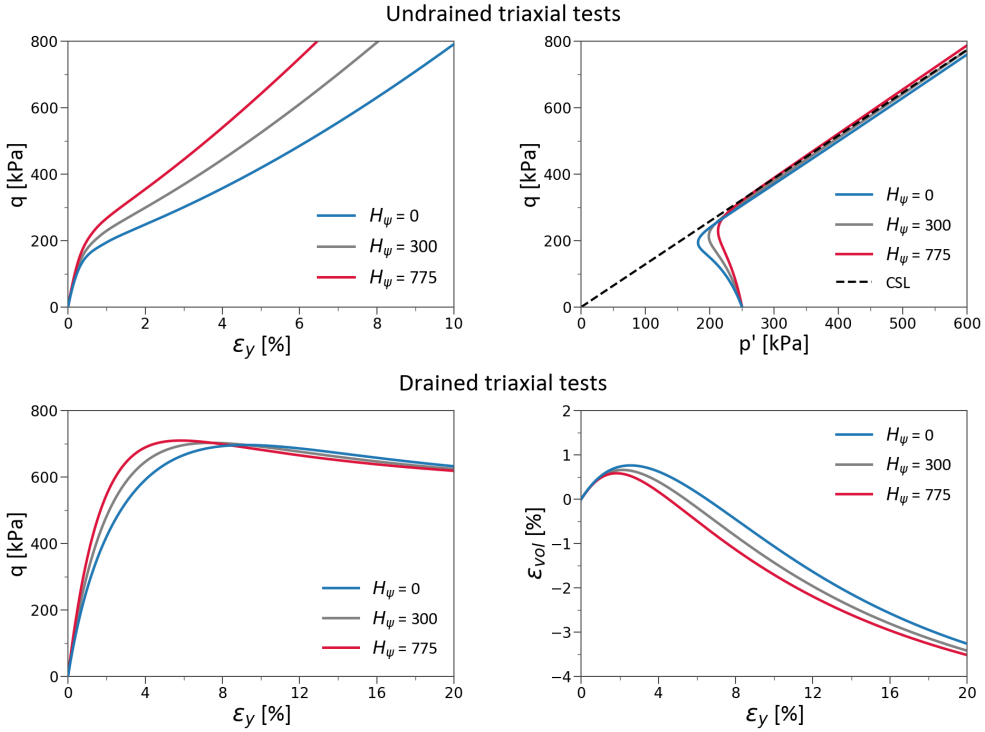

Figure A.9: Sensitivity analysis results of the hardening parameter, H_ψ, on dense material.